

Exoplanetary Atmospheric Characterization Using Polarimetry and Other Radiative Transfer Modeling Problems

Thesis by
Pushkar Kopparla

In Partial Fulfillment of the Requirements for the
degree of
Doctor of Philosophy

The logo for the California Institute of Technology (Caltech), featuring the word "Caltech" in a bold, orange, sans-serif font.

CALIFORNIA INSTITUTE OF TECHNOLOGY
Pasadena, California

2018
Defended 14 March 2018

© 2018

Pushkar Kopparla
ORCID: 0000-0002-8951-3907

All rights reserved

ACKNOWLEDGEMENTS

I'd like to thank my teacher, Prof. Yuk Yung, for a great education. I remember my first group meeting, where nearly a dozen different people brought up progress on their work in one or two sentences, and Yuk always knew exactly what issue they were facing. I did not know then that it was possible to have such a command of so many problems at once. Yuk always showed kindness in his own unique way, while running a tight ship. Beyond work, I enjoyed several conversations with him on various topics from politics, history, capitalism, relationships and life in general. I also learned a lot from him about working with people, and how to deal with conflict gracefully.

I'm also grateful to my committee members, Profs. Heather Knutson, Andy Ingersoll and Dave Stevenson. Apart from giving me great advice during my committee meetings, they also worked with me on research projects at different stages in grad school. Some of these projects did not reach a satisfactory conclusion, and that is certainly something I regret and will reflect on. Nonetheless, I was able to work on nearly anything I pleased and learn from these wonderful teachers. Such freedom is a rare and precious thing, and I will always be grateful to the culture of this Division and Caltech in general that enables freestyle research.

Several JPL scientists were vital to much of the work in this thesis, most prominent among them being Vijay Natraj and David Crisp. I'm deeply grateful to Vijay for leading me through the ins and outs of radiative transfer modeling with great patience. And thanks to Dave, who despite his doubly overbooked schedule always made time to attend the Friday meetings to talk about my work. Thanks to Sloane Wiktorowicz for giving me my first telescope observing experience. Also thanks to Mark Swain and members of his group for their valuable advice. Generous funding support from VPL at the University of Washington, courtesy of Prof. Victoria Meadows, and the President's and Director's Fund at Caltech were vital to working on exoplanet polarimetry, seen by many as unviable or at least premature. Thanks to Run-Lie Shia and also Shawn Ewald, for their kindness and willingness to help at any time. And of course, thanks to Margaret Carlos for managing all my bureaucratic affairs, to Ulrika Terrones for always being kind and to Irma Black for giving me this great new computer.

The planetary science grad student crowd is a tight knit, fun and supportive unit

even though everyone is neck deep in their own research and life problems. Though I cannot do full justice in acknowledging everyone's support, a few special mentions are in order. My thanks to Chris Spalding for coming by to talk in good moods and bad, to Ian Wong, for treating me to many delicious dinners and to Dana Anderson for making sure I could always go to her wonderful birthday parties. Thanks to Mike Wong, for your kindness, good cheer and for the many great experiences we shared together. Also thanks to Peter Gao, for inviting me to his bachelor party that I nearly did not survive, Nancy Thomas and Nathan Stein, for your halloween parties, trivia and other social initiatives. Outside the Division, I'd like to say thanks to Neel Nadkarni, for showing me it was humanly possible to eat that slowly, to Kishore Jaganathan, for not saying out loud his very worst jokes, and to Sumanth Dathathri, for learning to play Dota 2 with me.

Finally, I'd like to thank my family, including grandparents, aunts and uncles. In particular, my parents, K. N. Pavani and K. N. Murthy, made many sacrifices, including changing careers and living alone away from family, to make sure my sister, Mahati, and I got a good education.

ABSTRACT

This thesis deals with a pair of current problems with the remote sensing of planetary atmospheres. First is the modeling of polarization of scattered light from the atmospheres of exoplanets. With the first such observations becoming possible in the last year, there is a need to understand what these measurements actually mean. To that end, we developed families of radiative transfer models that simulate polarized phase curves for different atmospheric scenarios on hot Jupiters. These models were then used in the interpretation of scattered light from HD 189733b and WASP 12b, two hot Jupiter exoplanets, to determine their albedos and gauge what type of scattering particles might be present in their atmospheres. The last part of this half deals with observing oceans on distant Earth-like exoplanets using polarization from glint off the water surface. Though this measurement is not possible with current telescopes, but it may become accessible in the next decade with a slew of high powered ground and space telescopes in the pipeline.

The second half of the thesis is devoted to the development of a fast radiative transfer model. The goal of this model is to be able to process the massive amounts of data coming in from Earth observing satellites such as GOSAT and OCO-2 in a timely and accurate manner. We refined the principal component analysis based fast radiative transfer model to be accurate enough to retrieve carbon dioxide concentrations to the part per million accuracy that is necessary to track spatial and temporal changes in this important greenhouse gas.

PUBLISHED CONTENT AND CONTRIBUTIONS

1. Kopparla, Pushkar, Vijay Natraj, Drew Limpasuvan, Robert Spurr, David Crisp, Run-Lie Shia, Peter Somkuti, and Yuk L Yung (2017). “PCA-based radiative transfer: Improvements to aerosol scheme, vertical layering and spectral binning”. In: *Journal of Quantitative Spectroscopy and Radiative Transfer* 198, pp. 104–111., doi:10.1016/j.jqsrt.2017.05.005

I participated in the conception of the project, set up the model runs, analyzed the results and wrote the manuscript.

2. Kopparla, Pushkar, Vijay Natraj, Robert Spurr, Run-Lie Shia, David Crisp, and Yuk L Yung (2016). “A fast and accurate PCA based radiative transfer model: Extension to the broadband shortwave region”. In: *Journal of Quantitative Spectroscopy and Radiative Transfer* 173, pp. 65–71., doi:10.1016/j.jqsrt.2016.01.014

I participated in the conception of the project, performed the model runs, analyzed the results and wrote the manuscript.

3. Somkuti, Peter, Hartmut Boesch, Vijay Natraj, and Pushkar Kopparla (2017). “Application of a PCA Based Fast Radiative Transfer Model to XCO₂ Retrievals in the Shortwave Infrared”. In: *Journal of Geophysical Research: Atmospheres* 122.19., doi:10.1002/2017JD027013

I provided information on the use of our PCA-RT technique.

4. Kopparla, Pushkar, Vijay Natraj, Xi Zhang, Mark R Swain, Sloane J Wiktorowicz, and Yuk L Yung (2016). “A Multiple Scattering Polarized Radiative Transfer Model: Application to HD 189733b”. In: *The Astrophysical Journal* 817.1, p. 32., doi:10.3847/0004-637X/817/1/32

I participated in the conception of the project, assembled and wrote the code, performed the model runs, analyzed the results and wrote the manuscript.

5. Wiktorowicz, Sloane J, Larissa A Nofi, Daniel Jontof-Hutter, Pushkar Kopparla, Gregory P Laughlin, Ninos Hermis, Yuk L Yung, and Mark R Swain (2015). “A ground-based Albedo Upper Limit for HD 189733b from Polarimetry”. In: *The Astrophysical Journal* 813.1, p. 48., doi:10.1088/0004-637X/813/1/48

I performed the radiative transfer calculations used to interpret the observed data.

TABLE OF CONTENTS

Acknowledgements	iv
Abstract	vi
Table of Contents	viii
List of Illustrations	x
List of Tables	xvii
Chapter I: Introduction	1
Chapter II: Polarization from the HD 189733 System: Model Development and Interpretation of Observations	3
2.1 Abstract	3
2.2 Introduction	3
Polarimetry of HD 189733b	5
Photometric Observations	6
Theoretical Polarization Studies	6
2.3 The Atmospheric Structure of HD 189733b and Radiative Transfer	8
Model Setup	8
Disk Integration	10
Geometric Considerations	14
Atmospheric Structure of HD 189733b	15
2.4 Results and Discussion	17
Semi-infinite Rayleigh Scattering Atmospheres	18
Semi-infinite Hazy Atmospheres	20
Thin Atmospheres Above Cloud Decks	21
Inhomogeneous Atmospheres	23
Dependence on Orbital Parameters	25
2.5 Conclusions	25
2.6 Acknowledgements	27
Chapter III: Polarization of the WASP-12 System: Albedos and Cloud Com- position from Simple Models	34
3.1 Abstract	34
3.2 Introduction	34
3.3 Results and Discussion	35
3.4 Conclusions	39
3.5 Acknowledgments	41
Chapter IV: Observing Oceans in Tightly Packed Planetary Systems: Per- spectives from Polarization Modeling of the TRAPPIST-1 System	43
4.1 Abstract	43
4.2 Introduction	43
4.3 Model	44
4.4 Results	46

Atmospheric Effects	46
Signatures of Different Ocean Configurations	49
Phase Curves for the TRAPPIST-1 System	50
Observing Possibilities	53
4.5 Conclusions	56
4.6 Acknowledgements	56
Chapter V: A Fast and Accurate PCA Based Radiative Transfer Model: Ex- tension to the Broadband Shortwave Region and Improvements to Aerosol Scheme, Vertical Layering and Spectral Binning	60
5.1 Abstract	60
5.2 Introduction	61
5.3 The PCA RT Technique	62
RT Models	62
PCA RT Formalism	63
Model Setup and Preliminary Binning Considerations	65
5.4 Preliminary Results	66
5.5 PCA Efficiencies	69
5.6 Aerosol Scheme	71
5.7 Further Modifications to Binning Schemes	72
Scheme 1	73
Scheme 2	74
Other Issues	74
5.8 Final Results and Discussion	76
5.9 Acknowledgements	79

LIST OF ILLUSTRATIONS

<i>Number</i>	<i>Page</i>
2.1 Top panel shows reflectivities from Zhang et al. (2013) using DIS-ORT (blue dashed line), with this work using VLIDORT (solid green line) and observations from Cassini in the UV1 filter (red points) at $S60^\circ$ latitude and a phase angle of 17.5° . This is the blue curve in the top left panel of Figure 8 in Zhang et al. (2013). Bottom panel shows observed values of polarization in the blue channel from Pioneer 10 (Smith and Tomasko, 1984, red points) and the corresponding modeled values (this work, solid green line) at a phase angle of 98°	10
2.2 Geometric albedo as a function of single scattering albedo in a semi-infinite Rayleigh scattering atmosphere from this model (blue curve) and from Madhusudhan and Burrows, 2012 (red pluses).	14
2.3 Simple schematic indicating the breakup of the illuminated disk into smaller regions, each one of which is represented by a stack of plane parallel atmospheric layers. There are N (N typically being 1 or 2) layers which can have either gas alone (Rayleigh scattering) or a mixture of gas and haze particles. This is underlain by a thick, reflective cloud layer at the bottom. Single and multiple scattering (as indicated by the black arrows) are calculated using the radiative transfer model VLIDORT (Spurr, 2006).	17
2.4 Variation in the degree of polarization for reflected light from HD189733b with changes in geometric albedo for a semi-infinite, purely Rayleigh scattering atmosphere. I and P are normalized to direct starlight. The B11 and W09 lines indicate the amplitude of observations from Berdyugina et al. (2011) and the upper limit for non-detection from Wiktorowicz (2009). Orbital phase 0 is mid-transit and 0.5 is mid-eclipse.	19

- 2.5 Variation in the degree of polarization as a function of single scattering albedo and orbital phase for a semi-infinite Rayleigh scattering atmosphere normalized to reflected light from the planet (top) and direct starlight (bottom). For the former, the highest degree of polarization occurs at low albedo, while for the latter (which is the observable quantity), it occurs at high albedo. 20
- 2.6 Variation in the degree of polarization from reflected light HD189733b system with a semi-infinite pure gas and hazy atmospheres. The particle properties are listed in Table 2.2. The geometric albedo of the planet is forced to remain close to 0.23. B11 and W09 lines indicate the amplitude of observations from Berdyugina et al. (2011) and Wiktorowicz (2009). 22
- 2.7 Variation in reflected intensity and the degree of polarization for different atmospheric structures of HD 189733b. The intensity curves for a semi-infinite Rayleigh atmosphere (deep gas), thin, clear gas atmosphere (thin gas) and a hazy atmosphere with spherical particles (thin haze) on top of a cloud layer. The haze and cloud properties are mentioned in Table 2.2. 23
- 2.8 Variation in reflected intensity and the degree of polarization as a planet with an inhomogeneous atmosphere completes one orbit compared to a homogeneous, Rayleigh scattering planet. The spheres on top show the planet as seen from Earth at the phases indicated on the abscissa. The dark blue regions are pure Rayleigh scattering, and the greyish regions contain haze. The portion covered by the box indicates the night side of the planet. 24
- 2.9 The top panel shows a cartoon of two orbits of inclination close to 90 degrees and longitude of the ascending node 16 degrees (red, solid line) and -16 degrees (blue, dashed line) for the HD189733b system as seen from Earth. (Figure is approximate, not to scale, angles are not accurately depicted). The arrow indicates the sense of motion of the planet in the orbit and upwards is North in the sky plane of the Earth. These orbits are indistinguishable from photometry alone, but can be separated using polarimetry. The sign of Stokes parameter U changes, while intensity is invariant for this pair of orbits. 26

3.1	Scattered light intensity and polarization for Rayleigh scattering atmospheres on WASP-12b with various geometric albedos. Polarization is expressed as a fraction of direct unscattered starlight in units of parts per million (ppm).	36
3.2	Variation of the peak polarization amplitude due to scattering a clear atmosphere on WASP-12b with geometric albedo. A given value of peak polarization translates directly to a single geometric albedo value of the planet and can be compared to measurements from other techniques such as secondary eclipse (Bell et al., 2017).	37
3.3	Polarized light curves for corundum (top) and perovskite (bottom) cloud scattering on WASP-12b. Note that peak polarization is a non-monotonic function of particle size.	38
3.4	Maximum polarization from the scattering of light by a thick atmospheric cloud on WASP-12b for cloud composed of Al_2O_3 particles of various sizes. The numbers next to the points on the plot indicate geometric albedos for WASP-12b.	39
3.5	Same as 3.4, but for a cloud of $CaTiO_3$ particles.	40
4.1	Normalized Stokes parameter I and degree of polarization P for a Cox-Munk glint surface under a very thin 1-D Rayleigh scattering atmosphere (optical depth 0.01) for a variety of values of VZA and AZM. SZA = 60 deg. The wind speed is 1 m/s for the plots in the top row, and 10 m/s for those in the bottom row.	46
4.2	A typical total column optical depth spectrum of the Earth's atmosphere between the wavelengths 0.3 and 3 μm with Rayleigh scattering, gas and aerosol extinction but no clouds. Note that an atmosphere can be optically thin in a given wavelength range ("atmospheric window" regions) even with a large column air mass. This profile was generated by the WRF-Chem chemistry and transport model for a location over the continental US (Grell et al., 2005; Fast et al., 2006; Peckham et al., 2011)	47

- 4.3 Reflected starlight intensity and degree of polarization phase curves for TRAPPIST-1e in the thin (left column) and thick atmospheric (right column) limits over an ocean like glinting surface. Legend indicates the optical depth of the atmosphere. The phase angle used here is an atypical convention chosen for consistency with exoplanetary polarization literature (for e.g., Wiktorowicz et al., 2015). Under this convention, phase angles of 0 and 1 correspond to mid-transit (only nightside is visible) and a phase of 0.5 corresponds to opposition (full dayside is visible). Intensity and polarization are expressed as fractions of direct, unscattered starlight in units of parts per million [ppm] and parts per billion [ppb]. 48
- 4.4 Same as Fig 4.3, but with scattering by cloud particles of size $2 \mu\text{m}$. Note the appearance of rainbows around phase 0.4 and 0.6 in the thick cloud limit. 49
- 4.5 Phase curves for fully ocean covered (aqua), completely dry planet and two intermediate cases. The equatorial ocean and global ocean cases have near identical polarization curves since the glint signal comes primarily from near the equator. The intensity curves for the non-dry cases are nearly identical, and different from the dry case, since the dry surfaces are brighter than the ocean at non-glint angles and contribute significantly to disc brightness. 51
- 4.6 Reflected light intensity and polarization expressed as a fraction of direct starlight for the TRAPPIST-1 system for one period of the outermost planet (~ 19 days). Planet e is modeled as an aquaplanet, while the other planets are completely dry. The wet planet signal contributes a much higher fraction of the sum total in polarization ($\sim 17\%$) than in intensity ($\sim 1\%$). 53
- 4.7 Fourier transforms of the combined phase curves (dark black line in Fig 4.6) for observing periods totaling 5, 10 and 20 periods of the outermost planet ($\sim 94, 188$ and 375 days) for cases 1-4 described in the text. Vertical lines indicate the periods of the known planets, TRAPPIST-1e is in green. 54

4.8	Modeled glint star-planet contrast signals (dot-dash grey lines) plotted against detection limits of various upcoming large telescopes (WFIRST, LUVOIR and ELT) for systems at a distance of 10 pc. The blue and red lines indicate the distance from the star at which a planet receives an Earthlike (surface water ocean) and Titanlike (surface hydrocarbon lakes) solar flux. Present or near future observable Earth like planets (size smaller than $2R_{Earth}$) from Kepler detections and candidate objects (downloaded from exoplanets.org (Han et al., 2014) on 6 Oct 2017) and simulated detections from TESS (Sullivan et al., 2015) are overplotted for a sense of the number of detections by surveys that may have an ocean, which can be followed up for glint studies. Planetary periods listed in the TESS simulated dataset are converted to orbital distances by converting the listed stellar radii to stellar masses using the method of Demircan and Kahraman, 1991.	55
5.1	Top of the Atmosphere (TOA) reflectances from Exact-RT LIDORT for a single profile showing major absorptions. There are 33 spectral fields in all, with 8 in the ultraviolet/visible and the rest in the shortwave infrared (Table 5.1).	66
5.2	Residuals (%) of the Exact-RT LIDORT radiances for 2, 4, 8, and 16 streams compared with the 32-streams LIDORT calculations. Optical properties as for Figure 5.1	67
5.3	Residuals (%) for the PCA (black) and 2S (red) models as compared to 32 stream LIDORT over the entire shortwave range. The residuals have been Gaussian smoothed to 0.2 cm^{-1}	68
5.4	Residuals of the PCA (black) and 2 Stream (red) models as compared to 32 stream LIDORT with (top) and without (bottom) smoothing for spectral field 9, where the dominant gas absorbers are oxygen and water.	69
5.5	The sum total of the runtime of LIDORT and PCA model over all spectral fields for one profile with changing number of computational streams. Note from Figure 3 that increasing the number of streams improves the PCA RT accuracy, with very little time penalty as shown in this figure. Refer to text for further discussion.	70

5.6	Total column optical depth reconstruction accuracy using 5 EOFs for various settings: (upper left) "standard" PCA on log optical properties on an arbitrarily spaced vertical grid, (upper right) same as standard PCA but with linear optical properties, (lower left) PCA on log optical properties on an equal pressure thickness grid, (lower right) PCA on linear optical properties on an equal pressure thickness grid. Optical depths are reconstructed layer by layer and then summed, and compared to the total column optical depth in the original data set.	71
5.7	Comparison of PCA RT performance: (top) arbitrarily spaced vertical grid, (bottom) equal pressure thickness grid. Both grids have 114 layers. RMSE denotes the root mean square error.	72
5.8	Differences in PCA RT residuals (bottom) using bin averaging for aerosol optical properties, and (top) with explicit inclusion of aerosols in the PCA process. Note the almost complete elimination of the slope in the latter scenario.	73
5.9	(upper left) TOA radiances, (upper right) residuals using Scheme 1 with 11 bins, (lower left) residuals using Scheme 1 with 21 bins, and (lower right) Scheme 2 with 11 bins, for spectral window 11. The band of absorption lines centered at $0.76\mu\text{m}$ is the O ₂ A-band, and that around $0.79\mu\text{m}$ is due to water vapor absorption.	75
5.10	Top of the atmosphere radiances (top left) and residuals using Scheme 2 with 5 bins (top right), 21 bins (bot left) for spectral range 4. Since adding more bins was found to be ineffective with both Schemes 1 (not shown here) and 2, the spectral range was split into two around $0.535\mu\text{m}$. Each piece was then treated as a separate spectral range and solved using Scheme 1 binning with 5 bins (bot right).	75
5.11	Residuals in spectral window 11 for two different profiles, with different viewing geometries, aerosol densities and surface types, using Scheme 2 with 11 bins. For a given binning scheme, errors remain fairly constant for different atmospheric profiles taken from the GEOS-CHEM model (Bey et al., 2001).	76
5.12	TOA radiances over the entire shortwave range of interest, (top) with and (middle) without aerosols, and the difference between the aerosol and no aerosol cases (bottom) for a representative atmospheric profile.	77

5.13	Residuals over the entire shortwave range of interest using (top) purely Scheme 2 and (bottom) a combination of Schemes 1 and 2, for a representative atmospheric profile.	78
5.14	Mean distribution of residuals over 70 diverse atmospheric profiles using binning Scheme 2.	78

LIST OF TABLES

<i>Number</i>	<i>Page</i>
2.1 Comparisons with Rayleigh Scattering Results of Buenzli and Schmid (2009)	13
2.2 Summary of Parameters Used	17
3.1 Summary of Parameters Used	35
4.1 Scaling factors for brightness to convert above curves to other planets in the system based on relative size and orbital distance. Values taken from Wang et al. (2017).	52
5.1 Spectral Fields as Defined by Major Gas Absorptions.	80

Chapter 1

INTRODUCTION

Clouds and hazes are principal constituents of any planetary atmosphere, and their study is vital to understanding of atmospheric radiative properties, dynamics, climates, compositions and chemistry. Clouds and hazes are very well studied on Earth, still somewhat of an enigma on other Solar System planets and pretty much uncharted territory on exoplanets, though this is rapidly changing with the constant influx of observations and the development of increasingly sophisticated atmospheric chemistry and dynamical models.

Constraining the composition of hazes observationally on these exoplanets is a hard problem. Since the best observed exoplanets have thus far been hot Jupiters, hazes that can exist in the atmospheres of these very hot planets are typically metal oxides or silicates. There is a lack of easily identifiable spectral features for these species, and uniquely identifying one will require high quality spectra across a broader wavelength range than is currently possible. As a result, we can only infer the presence of clouds or haze due to increased opacity in the atmosphere affecting absorptions by species such as sodium, potassium or water. It is usually possible to narrow the haze candidates based on condensation curves at the expected temperatures, however, a unique determination of haze composition has remained out of reach thus far.

It is here that polarimetry offers a vital piece of information. Different haze candidates often have distinct refractive indices and polarization by scattering is very sensitive to this property. Polarimetry aided in the identification of the composition of clouds on Venus (Hansen and Hovenier, 1974) and hazes in the atmosphere of Titan (West and Smith, 1991). The challenge, as always with exoplanets, is to obtain data of a high enough quality to make the distinction between species. In this thesis, we are able to see exoplanet polarimetric data making this transition, primarily due to the efforts of Sloane Wiktorowicz who built and continually refined the polarimeter and continues to make these observations. The chapter on HD 189733 shows the first set of data that are completely dominated by telescope effects, resulting in a non-detection of polarization from the system of interest. In the next chapter on WASP-12b, the observations are still dominated by telescope effects. However,

these effects are regular and the planetary polarization can be retrieved after isolating them. The data is now of sufficient quality to make distinctions between scattering by corundum or perovskite hazes.

The fourth chapter is more of a view towards the future of exoplanet polarimetry. We attempt to answer the question: what will it take to get a direct observation of an ocean on an Earth like exoplanet? Polarimetry is useful here since specular reflection off a water surface is almost 100% linearly polarized. The answer, it seems, depends on a lot of variables: how big the ocean is, how thick the atmosphere and what it's made of. Though the prospects of such an observation appear bleak at the moment, high powered telescopes that are expected to come online within the next decade might plausibly make it happen.

The last chapter returns to another problem of atmospheric scattering, this time in the Earth's atmosphere. With the advent of several carbon monitoring satellites, such as GOSAT, OCO-2 and TANSAT, there are now several hundred thousand atmospheric spectra being captured globally everyday. Quickly and accurately retrieving carbon dioxide concentrations from this data requires complex radiative transfer calculations that account for the scattering properties of hazes and different land surface types. To this end, we refined an existing principal component analysis based fast radiative transfer model to satisfy the speed and accuracy requirements for this task. Retrievals using simulated GOSAT data showed that the model was a hundredfold faster than a standard line by line radiative transfer model, while maintaining an accuracy of 0.06 ppm for carbon dioxide retrievals (Somkuti et al., 2017).

Chapter 2

POLARIZATION FROM THE HD 189733 SYSTEM: MODEL DEVELOPMENT AND INTERPRETATION OF OBSERVATIONS

This chapter is adapted from work previously published as

Kopparla, Pushkar, Vijay Natraj, Xi Zhang, Mark R Swain, Sloane J Wiktorowicz, and Yuk L Yung (2016). “A Multiple Scattering Polarized Radiative Transfer Model: Application to HD 189733b”. In: *The Astrophysical Journal* 817.1, p. 32.

2.1 Abstract

We develop a multiple scattering vector radiative transfer model which produces disk integrated, full phase polarized light curves for reflected light from an exoplanetary atmosphere. We validate our model against results from published analytical and computational models and discuss a small number of cases relevant to the existing and possible near-future observations of the exoplanet HD 189733b. HD 189733b is arguably the most well observed exoplanet to date and the only exoplanet to be observed in polarized light, yet it is debated if the planet’s atmosphere is cloudy or clear. We model reflected light from clear atmospheres with Rayleigh scattering, and cloudy or hazy atmospheres with Mie and fractal aggregate particles. We show that clear and cloudy atmospheres have large differences in polarized light as compared to simple flux measurements, though existing observations are insufficient to make this distinction. Furthermore, we show that atmospheres which are spatially inhomogeneous, such as being partially covered by clouds or hazes, exhibit larger contrasts in polarized light when compared to clear atmospheres. This effect can potentially be used to identify patchy clouds in exoplanets. Given a set of full phase polarimetric measurements, this model can constrain the geometric albedo, properties of scattering particles in the atmosphere and the longitude of the ascending node of the orbit. The model is used to interpret new polarimetric observations of HD 189733b in a companion paper.

2.2 Introduction

Polarimetry has been used to probe the atmospheres of planets in the solar system; the first observation of linear polarization from Venus’ atmosphere is credited to Lyot (1929). More recently, the properties of clouds and hazes in Venus’s atmosphere

were deduced through polarimetric data from both ground-based observations and from Pioneer data (Hansen and Hovenier, 1974; Kawabata et al., 1980). Similar successful studies exist for Titan (Tomasko and Smith, 1982), Jupiter (Smith and Tomasko, 1984) and the other outer planets (Joos and Schmid, 2007). The idea of using polarimetry to probe exoplanetary atmospheres is thus a natural extension, and was first examined in a theoretical study by Seager, Whitney, and Sasselov (2000). The great advantage of using polarimetry in the study of exoplanets is the increase in contrast between direct starlight and the reflected light from the planetary atmosphere. Integrated over the whole disk, direct starlight from inactive, nearby stars can be assumed to be unpolarized to a high degree¹. For instance, the linear polarization integrated over the sun's disk is $\sim 1ppm$ (parts per million) in visible wavelengths (Kemp et al., 1987), light scattered from a planetary atmosphere may have polarizations of a few tens of percent. Thus, depending on the reflectivity of a planetary atmosphere, the degree of polarization in the star-planet system can be dominated by the reflected light from the planetary atmosphere. In such a case, the combined star planet system should show a periodic modulation in the degree of polarization as the planet moves through different phases of illumination in its orbit.

A prime exoplanet candidate for polarimetric studies is HD 189733b, a hot Jupiter orbiting a K star, with a semimajor axis of 0.031 AU. The system is relatively close by (19.3 parsecs) and thus bright. Berdyugina et al. (2008) reported a detection of polarized light of amplitude $200ppm$. Surprisingly, the strength of observed polarization was about one order of magnitude higher than predicted assuming a semi-infinite Rayleigh scattering atmosphere (which produces the highest degree of polarization for a given planetary radius), leading to some skepticism over the observations (Lucas et al., 2009). Follow up studies since have not reached a consensus on the observed degree of polarization (Wiktorowicz, 2009; Berdyugina et al., 2011). Furthermore, Lucas et al. (2009) observed the polarization of two other exoplanet systems, 55 Cnc and τ Boo. In both cases, they found polarization of the order of $1ppm$ but there was no significant variability associated with the orbital periods of the known exoplanets in these systems. In parallel however, there have been few efforts to model the observable polarization signal using what is known about the atmosphere of HD189733b from photometric measurements, since the early work of Lucas et al., 2009 and Sengupta, 2008. We will briefly examine the

¹Polarization is introduced in starlight through interactions with interstellar dust clouds and magnetic fields therein (Davis and Greenstein, 1949). However these values are unlikely to vary on planetary orbital timescales.

observations, and some of the issues involved in their interpretation, in order to understand what information can be retrieved using a multiple scattering radiative transfer model.

The chapter is structured as follows. The remainder of the introduction is devoted to a review of exoplanetary polarization studies, both theoretical and observational. In Section 2, we outline our model setup and validate our model using observations of Jupiter. In Section 3, we discuss the observable polarization signal for different atmospheric compositions, orbital orientations and spatial inhomogeneities in the atmosphere, followed by a summary in Section 4.

Polarimetry of HD 189733b

Berdyugina et al. (2008)'s study consisted of 93 individual nightly observations taken in the B band (370-550nm) through the KVA 0.6-m telescope and find variable polarization of amplitude $200ppm$. The degree of polarization is always measured as a fraction of the direct starlight, and not just the reflected light from the planet. They interpret their observations using a single scattering Rayleigh-Lambertian model, and are able to retrieve values of eccentricity and orbital inclination that agree quite well with other studies. To explain the large degree of polarization, they are forced to use a large planetary radius, $1.5 \pm 0.2 R_J$ where the standard value is $1.154 \pm 0.017 R_J$ (Pont et al., 2007). They comment that this large radius might be indicative of an extended, evaporating halo around the planet. It is uncertain if such a halo would be reflective enough to be responsible for a significant fraction of the reflected intensity.

Wiktorowicz (2009) observed the same planet in the wavelength range 400-675 nm from the Palomar 5-m telescope. He found polarization of the order of $10ppm$, but there was no significant relationship with the period of the exoplanet. However, this study has only one observation near elongation (phase angle 90°) where polarization is expected to peak and most observations are at phases where polarization is expected to be small, as has been pointed out by later papers (Berdyugina et al., 2011). This study also derives an upper limit to the polarimetric modulation of the exoplanet as $79ppm$ and the polarimetric variability of starspots to $21ppm$.

Berdyugina et al. (2011) observed polarization modulations in the U, B, and V bands centered at 360, 440 and 530 nm respectively with the NOT 2.5-m telescope. They find that the degree of polarization varies with the wavelength in proportion to the Rayleigh scattering law across the different bands. However, they revise their earlier

value of the amplitude of polarization from $200ppm$ down to $\sim 100ppm$. Because of the visual similarities to Neptune in the geometric albedo profile, they suggest that the atmosphere might have a similar structure, with a high altitude haze layer above a semi-infinite cloud deck. Another proposed structure is the presence of a dust condensate layer beneath a thin gas layer.

Photometric Observations

Temperatures in the atmosphere of HD 189733b are thought to vary between 1000-1500 K depending on altitude and longitude (Knutson et al., 2009; Knutson et al., 2012; Huitson et al., 2012). Its atmosphere is fairly well studied and is known to contain water (Tinetti et al., 2007), carbon monoxide (Kok et al., 2013), carbon dioxide and methane (Swain, Vasisht, and Tinetti, 2008; Swain et al., 2009) in trace amounts. The bulk composition is usually modeled to be mostly hydrogen and helium (Huitson et al., 2012; Danielski et al., 2014). From theoretical models, it is also expected that such an atmosphere would contain traces of metals like sodium, potassium and magnesium (Fortney et al., 2010). Weak detections of these metals from visible (Redfield et al., 2008) and infrared transmission spectra as well as strong slope from the UV to the near infrared, lead to the inference that a high level, Rayleigh haze that spans several scale heights over an opaque cloud deck may be present (Sing et al., 2009; Désert et al., 2011; Sing et al., 2011; Pont et al., 2013).

However, a recent pair of studies (Crouzet et al., 2014; McCullough et al., 2014) have put forth an alternative interpretation of the transit and secondary eclipse data. They argue that the slope previously attributed to a Rayleigh scattering haze could instead be caused by unocculted star spots in the field of view. This interpretation favors a clear, cloudless atmosphere for HD 189733b, though it does not rule out a hazy atmosphere.

The geometric albedo of HD 189733b was measured by Evans et al. (2013) using the HST to measure the brightness of the disk at secondary eclipse, and they find values of 0.40 ± 0.12 in the range 290-450 nm and an upper limit of 0.12 between 450-570 nm. This data provides an independent check for the albedos retrieved by Berdyugina et al. (2011). The values of Berdyugina et al. (2011) are systematically higher than those obtained by Evans et al. (2013).

Theoretical Polarization Studies

Seager, Whitney, and Sasselov (2000) in a pioneering study produced theoretical polarization curves for reflected planetary light using a forward Monte Carlo ra-

diative transfer (RT) model for a Rayleigh scattering atmosphere. They concluded that the maximum degree of polarization ($1 - 5 \times 10^{-5}$) was in most cases below detection limits at the time. They also examined the effects of scattering particles and cloud layers, in all cases deviation from a purely scattering gaseous atmosphere reduced the degree of polarization. Following this, there were a series of papers e.g., Stam, Hovenier, and Waters (2004) and Stam et al. (2006) using an adding doubling RT model. Their results were similar to that of the previous work, but the great advantage of their model is the generation of a "planetary scattering matrix". With this matrix, a single calculation can replicate multiple scattering radiative transfer through a planetary atmosphere of arbitrary thickness and composition (only for top of the atmosphere fluxes). Buenzli and Schmid (2009) explored the dependence of observable polarization signals on single scattering albedo, optical depth of the scattering layer, and albedo of an underlying Lambert surface for purely Rayleigh scattering atmospheres using a Monte Carlo model. Madhusudhan and Burrows (2012) used an analytic model on a Rayleigh scattering atmosphere to map out polarization signals for various scenarios.

While extensive parameter searches have been performed theoretically, the observational data have only been interpreted using very simple single scattering Rayleigh-Lambert models (Berdyugina et al., 2008; Berdyugina et al., 2011). Newer theoretical studies have moved onto modeling increasingly specialized features such as rainbows from water clouds (Bailey, 2007; Karalidi, Stam, and Guirado, 2013), surface vegetation (Stam, 2008), oceans (Williams and Gaidos, 2008) and relatively fine cloud structure (Karalidi and Stam, 2012). Current observations exist only for hot Jupiters, and it is unlikely that most of these features will either exist or be observable on such planets in the near future. In this way, there is a divergence between the modeling and observational community within the field. The goal of this work is the creation of an atmospheric polarization model with sufficient physics (multiple scattering, use of non-Rayleigh scattering functions, multiple atmospheric layers, inhomogeneous atmospheres) but simple enough (sufficiently few parameters) to be useful in the interpretation of current and near-future observations (so that data can constrain model parameters). The purpose of this model is to be a tool that augments our understanding of observations; it is not intended to function as a standalone parameter search engine.

2.3 The Atmospheric Structure of HD 189733b and Radiative Transfer

Model Setup

Our approach to building an exoplanetary atmospheric polarization model is to start with a well understood planetary atmospheric model, continually modify into an atmospheric structure relevant to HD 189733b and validate it at each step. We begin with a model of Jupiter’s stratosphere based on retrievals of Cassini data (Zhang et al., 2013), henceforth Z13. This model is attractive as a baseline since the atmosphere has realistic clouds and two different types of haze particles: spherical and fractal aggregates. While current polarimetric observations may not have sufficient data to distinguish between these two types of haze particles, we are optimistic about the future. Z13 model the atmosphere of Jupiter using a 12-layer plane parallel atmosphere with scattering and absorption at each layer, underlain by a reflective semi-infinite cloud layer. This model currently works only with the photometric intensity, I , while we require at least three of the Stokes parameters, I , the intensity, and Q and U , the linear polarization parameters. The degree of polarization, P is defined as

$$P = \frac{\sqrt{Q^2 + U^2}}{I_{star} + I_{planet}} \sim \frac{\sqrt{Q^2 + U^2}}{I_{star}} \quad (2.1)$$

We talk about degree of polarization in the total star-planet flux since this is the observable quantity. Direct starlight is assumed to be unpolarized integrated over the disk of the star. Symmetry breaking due to starspots or the transiting planet itself can induce non-zero polarization in direct starlight. However, these effects have been calculated to be about one order of magnitude smaller than the expected polarization from the planet (Kostogryz, Yakobchuk, and Berdyugina, 2015). If the detected polarization of the planet is much smaller than expected, these effects will become important and must be accounted for. The first change we make is to swap out the scalar RT model DISORT (Stamnes et al., 2000) which works only on intensities, with a vector RT model VLIDORT (Spurr, 2006) that can handle polarized radiances. This is a plane-parallel scattering code that uses the discrete ordinate method to approximate multiple scatter integral source terms in the RT equation. The model will make a precise single scatter calculation for both incoming solar and outgoing line-of-sight beams in a plane-parallel or spherical-shell atmosphere. Stokes vector output may be generated at any level in the atmosphere and for any angular distribution, using the source function integration technique. The model can handle coupled thermal/surface emission and multiple scattering scenarios, and there is a provision for dealing with bidirectional reflecting surfaces as well as the

usual Lambertian surface assumption. The VLIDORT model is also fully linearized: simultaneously with the polarized radiance field, it will deliver analytic Jacobians with respect to any atmospheric and/or surface properties.

VLIDORT has been validated against Rayleigh (Coulson, Dave, and Sckera, 1960) and aerosol benchmark results (Garcia and Siewert, 1989; Siewert, 2000). Details of the validation can be obtained from Spurr (2006). VLIDORT has also been validated in the thermal infrared (with no solar sources) and mid infrared (with both solar and thermal emission sources) spectral regions by comparisons with the National Center for Atmospheric Research GENLN Spectral Mapper model, which in turn is based on the GENLN line-by-line RT algorithm (Edwards, 1992). VLIDORT has been previously used in remote sensing applications for Earth (Cuesta et al., 2013; Xi et al., 2015).

We validate this modified Jupiter atmosphere vector model by reproducing known photometric and polarimetric results for the atmosphere of Jupiter. The basic calculation here is one-dimensional, monochromatic radiative transfer in a plane parallel atmosphere for a given set of observing angles using an 8-stream RT model, following Z13. We are able to reproduce, up to four decimal places, the best fits of Z13 to Cassini data at different wavelength filters and latitudes. A representative plot is shown in the top panel of Figure 1 for an atmosphere containing fractal aggregate hazes over a reflective cloud layer. Haze particles are either modeled as Mie spheres (De Rooij and Van der Stap, 1984) or fractal aggregates, using the approximate method of Tomasko et al. (2008) designed for Titan hazes. Well resolved polarimetric data of Jupiter has existed since the Pioneer missions (Smith and Tomasko, 1984). We attempt to reproduce these values using the atmospheric model of Z13 with VLIDORT for the relevant latitudes. The bottom panel of Figure 2.1 shows the degree of polarization produced by our model and the corresponding Pioneer observations, taken from Table IVC of Smith and Tomasko (1984). These observations correspond to the blue filter, whose central wavelength is $0.44\mu\text{m}$ (Pellicori, Russell, and Watts, 1973). The fit is certainly not as good as that for photometry. Inaccuracies may partially be due to the fact that the retrieved parameters are optimized to match the photometric data from Cassini alone, whose wavelengths are different. The optical properties at $0.44\mu\text{m}$ are thus interpolated values from the Cassini retrievals. Also, aerosol properties at 98° phase angle are not constrained well by the Cassini ISS data in Z13, most of the images of which are at small ($< 30^\circ$) and large ($> 130^\circ$) phase angles. Two more validation cases

are discussed in the following section on disk integration.

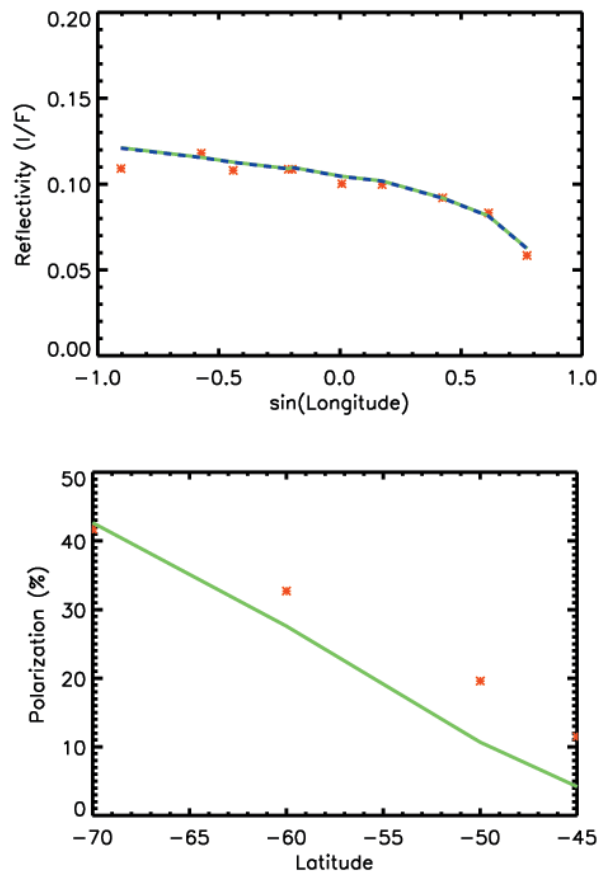


Figure 2.1: Top panel shows reflectivities from Zhang et al. (2013) using DIS-ORT (blue dashed line), with this work using VLIDORT (solid green line) and observations from Cassini in the UV1 filter (red points) at $S60^\circ$ latitude and a phase angle of 17.5° . This is the blue curve in the top left panel of Figure 8 in Zhang et al. (2013). Bottom panel shows observed values of polarization in the blue channel from Pioneer 10 (Smith and Tomasko, 1984, red points) and the corresponding modeled values (this work, solid green line) at a phase angle of 98° .

Disk Integration

Unlike Jupiter, where the disk of the planet is well resolved, polarimetric observations of exoplanets will only yield disk integrated values. Thus, the equation of radiative transfer must be solved for a finite number of points on the planet and the emergent radiance summed to yield disk integrated values. We use the quadrature method of Horak (1950) for fast disk integration. The polarized light can be represented by the Stokes vector, \mathbf{I} , which comprises of the four Stokes parameters, I , Q ,

U and V .

$$\mathbf{I} = \begin{bmatrix} I \\ Q \\ U \\ V \end{bmatrix} \quad (2.2)$$

The integral of interest, which gives the integrated Stokes parameters of the planet over the illuminated fraction of the disk at a phase angle α , is

$$j(\alpha) = \int_0^\pi \sin^2 \eta \, d\eta \int_{\alpha-\pi/2}^\pi \mathbf{I}(\eta, \zeta) \cos \zeta \, d\zeta \quad (2.3)$$

where $\mathbf{I}(\eta, \zeta)$ is the outgoing Stokes vector from the point defined by the colatitude η and longitude ζ in the direction of the observer. The intensity within the integral is not analytical and must be obtained from multiple scattering calculations from VLIDORT. It is therefore preferable to have the integral expressed as a summation over some finite number of points. Using the transformation

$$\xi = \left(\frac{2}{\cos \alpha + 1} \right) \nu + \left(\frac{\cos \alpha - 1}{\cos \alpha + 1} \right), \psi = \cos \eta \quad (2.4)$$

where $\nu = \sin \eta$, the limits of the integrals are changed to -1 to +1. Note that these equations are valid for positive phase angles, α . For negative phase angles, the extent of the illuminated disk is expressed as

$$j(\alpha) = \int_0^\pi \sin^2 \eta \, d\eta \int_{-\pi/2}^{\pi-\alpha} \mathbf{I}(\eta, \zeta) \cos \zeta \, d\zeta \quad (2.5)$$

The corresponding variable substitution is now

$$\xi = \left(\frac{2}{\cos \alpha + 1} \right) \nu - \left(\frac{\cos \alpha - 1}{\cos \alpha + 1} \right), \psi = \cos \eta \quad (2.6)$$

These integrals can now be expressed as the summations

$$j(\alpha) = \frac{(\cos \alpha + 1)}{2} \sum_{i=1}^n \sum_{j=1}^n w_i u_j \mathbf{I}(\psi_i, \xi_j) \quad (2.7)$$

where each w_i and u_j represents the quadrature weights for the quadrature divisions ψ_i and ξ_j . For a given number of summation terms, n , the quadrature weights and divisions are well defined (Chandrasekhar, 1960). VLIDORT only needs to be run at the positions on the disk indicated by these divisions and summed up to give

the outgoing intensity. The inputs to VLIDORT are the solar zenith angle (θ_o), indicating the direction of the incoming flux from the star measured with respect to the local normal to the surface, viewing zenith angle (θ), which is the direction of outgoing radiance to the observer, and the relative azimuthal angle ($\Delta\phi$) between these two directions. These angles are given by

$$\cos \theta_o = \sin \eta \cos(\eta - \alpha) \quad (2.8)$$

$$\cos \theta = \sin \eta \cos(\eta) \quad (2.9)$$

$$\tan \Delta\phi = \frac{\sin \alpha \cos \eta}{\cos \theta \cos \theta_o - \cos \alpha} \quad (2.10)$$

We verify that our numerical implementation is correct by reproducing Table 3 of Horak (1950) for surface reflection from a Lambertian surface. The effects using different numbers of quadrature points, computational streams in the RT model and the resolution of the orbit are discussed in the appendix. In brief, pure Rayleigh scattering atmospheres are insensitive to resolution effects and use 8-stream, 64-point quadrature. Mie scattering atmospheres require at least 16-stream RT to produce rainbows and use 32-stream and 256-point quadrature for the cases discussed. For inhomogeneous hazy atmospheres with sharp discontinuities in the scattering properties across the disk, 32-stream, 1024-point quadrature was used to produce smooth curves in reflected intensity. Model runtime scales linearly with number of phases modeled per orbit, as the square of the linear spatial resolution of the disk and the cube of the number of RT streams.

To further validate our disk integration scheme implementation, we reproduce the disk integrated reflectivity and degree of polarization calculations from Buenzli and Schmid (2009) for Rayleigh scattering atmosphere of optical depth 30 and single scattering albedo 0.999999 over a Lambertian surface of albedo 1. Our results agree well with published values, as shown in Table 2.1. The error in the degree of polarization is given as 0.1% in Buenzli and Schmid, 2009. The columns are the scattering phase angle (α), reflectivity (I , this work, I_{BS} from (Buenzli and Schmid, 2009)) and the degree of polarization expressed as a percentage of reflected light (q and q_{BS} respectively). In this work, we use the definitions of the Stokes parameters as given by Hovenier, Mee, and Domke, 2014, which are the same as those used in Chandrasekhar, 1960. Buenzli and Schmid, 2009 use the definition from Coulson, Dave, and Sckera, 1960, which only differs in the sign of Q .

Furthermore, since we are particularly interested in measurements of the geometric albedo, we also validate our calculations for the dependence of geometric albedo

Table 2.1: Comparisons with Rayleigh Scattering Results of Buenzli and Schmid (2009)

α [°]	$I(\alpha)$	$I_{BS}(\alpha)$	$q(\alpha)$ [%]	$q_{BS}(\alpha)$ [%]
2.5	0.796	0.795	-0.0	0.0
7.5	0.786	0.785	-0.4	0.4
12.5	0.767	0.766	-1.1	1.1
17.5	0.741	0.740	-2.1	2.1
22.5	0.709	0.708	-3.4	3.4
27.5	0.672	0.671	-5.0	5.1
32.5	0.631	0.630	-6.9	6.9
37.5	0.588	0.587	-9.1	9.1
42.5	0.543	0.542	-11.4	11.4
47.5	0.498	0.497	-14.0	13.9
52.5	0.453	0.453	-16.6	16.6
57.5	0.410	0.410	-19.3	19.3
62.5	0.368	0.368	-22.0	22.0
67.5	0.329	0.329	-24.6	24.6
72.5	0.293	0.292	-27.0	27.0
77.5	0.259	0.259	-29.1	29.1
82.5	0.228	0.228	-30.8	30.7
87.5	0.199	0.199	-32.0	31.9
92.5	0.174	0.174	-32.6	32.5
97.5	0.151	0.150	-32.5	32.5
102.5	0.130	0.130	-31.9	31.8
107.5	0.111	0.111	-30.5	30.5
112.5	0.094	0.094	-28.6	28.6
117.5	0.079	0.079	-26.2	26.2
122.5	0.066	0.066	-23.4	23.4
127.5	0.054	0.054	-20.2	20.3
132.5	0.043	0.043	-16.9	17.0
137.5	0.033	0.033	-13.6	13.7
142.5	0.025	0.025	-10.3	10.4
147.5	0.018	0.018	-7.1	7.3
152.5	0.012	0.013	-4.3	4.4
157.5	0.008	0.008	-1.9	2.0
162.5	0.004	0.005	0.1	0.0
167.5	0.002	0.002	1.5	-1.4
172.5	0.001	0.001	2.0	-1.9
177.5	0.000	0.000	-	-

(Signs are opposite due to the use of different conventions. See text for details)

on the single scattering albedo. For comparison, we use the fitted analytic expres-

sion from Madhusudhan and Burrows (2012), shown in Figure 2.2. We get good agreement except close to single scattering albedo ~ 1 , where the analytic fitting expression is not good as reported by Madhusudhan and Burrows, 2012. However, our model value of 0.7976 is close to the published numerically computed values of 0.7977 (Madhusudhan and Burrows, 2012) and 0.7975 (Prather, 1974). VLIDORT cannot handle a single scattering albedo of exactly 1, and therefore we use the value 0.999999.

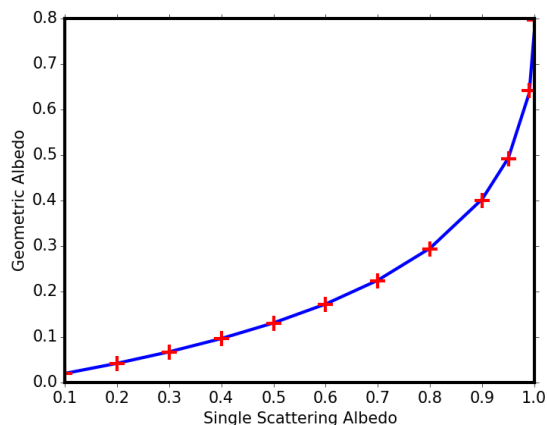


Figure 2.2: Geometric albedo as a function of single scattering albedo in a semi-infinite Rayleigh scattering atmosphere from this model (blue curve) and from Madhusudhan and Burrows, 2012 (red pluses).

Geometric Considerations

For a circular orbit, we have the scattering angle for a given orbital position (Madhusudhan and Burrows, 2012)

$$\cos \alpha = \sin \phi \sin i \quad (2.11)$$

where ϕ is the true anomaly and i is the inclination. As the orbit is circular, we take the true anomaly to be the same as our orbital position angle. $\phi = 0$ corresponds to superior conjunction as seen from Earth and $\phi = \pi$ corresponds to mid-transit. The definition of the Stokes parameters Q and U is generally with respect to the plane of the sky as seen from Earth. However, each VLIDORT calculation yields these parameters in the local scattering plane. Therefore, one rotation is necessary to change the reference plane to the equatorial plane of the exoplanet before being summed up by the quadrature formula above. A second rotation is necessary to express the polarizations in the sky plane of the Earth. In both cases, the Stokes

parameters I and V remain unchanged since they deal with the total intensity and the handedness and magnitude of circular polarization. Thus the first rotation is of the form (Madhusudhan and Burrows, 2012)

$$\begin{bmatrix} I' \\ Q' \\ U' \\ V' \end{bmatrix} = \begin{bmatrix} 1 & 0 & 0 & 0 \\ 0 & \cos 2\gamma_1 & \sin 2\gamma_1 & 0 \\ 0 & -\sin 2\gamma_1 & \cos 2\gamma_1 & 0 \\ 0 & 0 & 0 & 1 \end{bmatrix} \begin{bmatrix} I \\ Q \\ U \\ V \end{bmatrix} \quad (2.12)$$

$$\cos \gamma_1 = \frac{\sin \eta \sin \zeta}{\sin \theta} \quad (2.13)$$

θ is the angle with the vertical at the point of scattering made by the outgoing beam of radiation to Earth. The angle of the second rotation is a function of the planet's position in the orbit and is given by (Schmid, 1992)

$$\gamma_2 = \tan^{-1} \left(\frac{\tan \phi}{\cos i} \right) + 90^\circ + \omega_p \quad (2.14)$$

where i is the inclination of the orbit and ω_p is the longitude of the ascending node. Note that the orbit is assumed to be nearly circular, which is valid for HD 189733b. The rotation itself is of the form

$$Q'' = Q' \cos 2\gamma_2 \quad (2.15)$$

$$U'' = Q' \sin 2\gamma_2 \quad (2.16)$$

I and V are unaffected as before. Note that U' plays no role in the second rotation since its value drops to zero during the first rotation and summation over the illuminated disk for a planet that is symmetric about its equator. This set of transformations yield the full orbit polarized phase curve $[I(\phi), Q''(\phi), U''(\phi), V(\phi)]$ for the planet. Our simple model does not account for transit, secondary eclipse or limb effects in the star and the planet, non-spherical planets, thermal emission from the planet and other higher order effects. Those will be considered in future efforts.

Atmospheric Structure of HD 189733b

Starting with the relatively complex Jupiter atmosphere of Z13, we construct simple atmospheric structures that may be plausible for HD 189733b. The legacy atmospheric model from Z13 consists of 11 layers of gas and haze particles; gas is present in each layer while haze particles may or may not be present. The 12th (deepest) layer being an optically thick reflective cloud layer with single scattering albedo

0.99. Gas is also present in this layer; however, the large optical depth of the cloud makes scattering by gas inconsequential within this layer. A simple schematic of this plane parallel atmosphere is provided in Figure 2.3. Since we do not require this level of vertical resolution with current observations, we will reduce the number of gas layers, N to 1 or 2 depending on the case of interest. Should observations of sufficient quality become available, it is easy to add on more layers. The cloud layer is underlain by a Lambertian surface of albedo zero to provide a boundary condition. However, the cloud layer is thick enough ($\tau_{cloud} = 50$) that changes to the albedo of this surface has no observable effect. The atmospheric composition of HD 189733b consists primarily of hydrogen and helium, with traces of methane, carbon dioxide and water. Since none of these gases have absorption lines or bands at $0.44\mu m$, their contribution is primarily Rayleigh scattering. We take the typical depolarization ratio of 0.02 for hydrogen as representative of the atmosphere following Stam, Hovenier, and Waters (2004). The scattering properties of the underlying cloud layer is described by a double Henyey-Greenstein (DHG) function, Equation 2 of Z13. The DHG function is fully depolarizing. For the sake of simplicity and due to the lack of better alternatives, we use the following values from Table 4 of Z13 for the parameters for the double Henyey-Greenstein scattering function, $f_1 = 0.8303$, $g_1 = 0.8311$ and $g_2 = -0.3657$. A summary of relevant atmospheric parameters is provided in Table 2.2. The total column optical depth of the gaseous atmosphere (excluding the bottom cloud layer) is treated as a free parameter. However, we find that with total column optical depths of order one, a doubling or halving of the optical depth only results in changes of order 5-10% in the intensity and degree of polarization for a pure Rayleigh scattering atmosphere.

Haze particles are either modeled as Mie spheres (De Rooij and Van der Stap, 1984) or fractal aggregates, using the approximate method of Tomasko et al. (2008) designed for Titan hazes. The refractive index of the particles is fixed at $1.68 + 10^{-4}i$ (Jäger et al., 2003), representing a composition of silicate grains as hypothesized by Pont et al. (2013). Since the slope seen in transmission spectra is attributed to a scattering haze over several scale heights, we assume a well mixed atmosphere. Thus, the mixing fraction of haze particles will have no vertical variations in our models, unless the variation is the difference between the existence or absence of haze. For the following sections, we fix the wavelength of radiative transfer calculations at $0.44\mu m$, which is the central wavelength of the B band in the visible range. It is relatively straightforward to change the wavelength to the UV or IR ranges, as long as the relevant scattering and extinction cross-sections are available

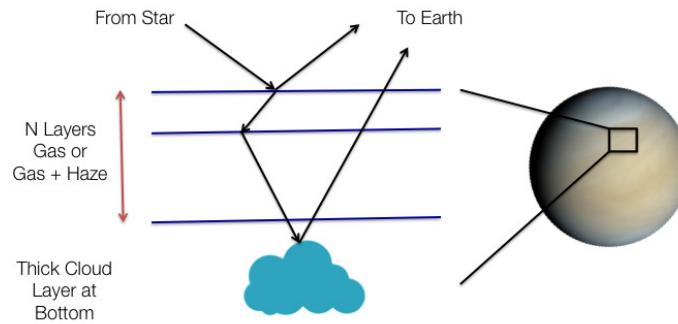


Figure 2.3: Simple schematic indicating the breakup of the illuminated disk into smaller regions, each one of which is represented by a stack of plane parallel atmospheric layers. There are N (N typically being 1 or 2) layers which can have either gas alone (Rayleigh scattering) or a mixture of gas and haze particles. This is underlain by a thick, reflective cloud layer at the bottom. Single and multiple scattering (as indicated by the black arrows) are calculated using the radiative transfer model VLIDORT (Spurr, 2006).

Table 2.2: Summary of Parameters Used

Function	Parameter	Value
Wavelength		$0.44 \mu\text{m}$
Cloud Ph. Fn. (DHG)	f1	0.8303
	g1	0.8311
	g2	-0.3657
Haze Particles	Refractive Index	$1.68 + 10^{-4}i$
	Radius (spherical)	$1 \mu\text{m}$
	Monomer radius (fractal)	10nm
	Monomers/particle	1000

for all gases, haze and cloud particles. The planetary and orbital parameters for HD 189733b are taken as follows. The radius of the planet is $1.138R_j$, semi-major axis is 0.03 AU and the eccentricity of the orbit is taken to be nearly zero (actual value is 0.0041) (Torres, Winn, and Holman, 2008). The inclination of the orbit can be either 86° (Triaud et al., 2010; Berdyugina et al., 2008) or 94° (Berdyugina et al., 2011) (we use 94°) and the longitude of the ascending node is 16° (Berdyugina et al., 2008).

2.4 Results and Discussion

Polarimetric observations typically yield the two linear polarization parameters, Stokes Q and U , in addition to the intensity. In reflected starlight, circular po-

larization over the northern and southern hemispheres will likely have comparable absolute values but opposite signs. The result is that integrated over the disk, the circular polarization values are very small. The degree of circular polarization is at least 4-5 orders of magnitude smaller than the linear polarization, and cannot be measured with current technology for exoplanets. Thus, the reflected light from the atmosphere of an exoplanet is described fully by I , Q and U . The total degree of polarization of reflected light is wholly determined by the nature of scattering in the planetary atmosphere, while the viewing geometries determine the distribution of polarization between the parameters Q and U . The broad atmospheric structure of HD 189733b is still a matter of active debate. Depending on the interpretation of transit spectra, cloudy or clear atmospheric scenarios cannot be ruled out (Crouzet et al., 2014). Thus, we will examine a few simple structures and their associated polarization signatures here.

Semi-infinite Rayleigh Scattering Atmospheres

The recent ideas of Crouzet et al. (2014) and McCullough et al. (2014) support a clear atmosphere for HD 189733b. Thus, we start with a very simple case: a thick, purely Rayleigh semi-infinite scattering atmosphere. The atmosphere has one single Rayleigh scattering layer with an optical depth of 1000, above a Lambertian surface of albedo 1.0. We will refer to such atmospheres as a semi-infinite Rayleigh scattering atmospheres in the following discussions. We vary the single scattering albedo to simulate the effect of changes in geometric albedo of the planet. The results are shown in Figure 2.4, with reflected intensity and polarization normalized to total direct starlight. Disk integrations are carried out at every 5° in orbital position angle. Following the notation of (Berdyugina et al., 2011), orbital phase angle of 0° (secondary-eclipse) corresponds to an orbital phase of 0.5, and an orbital phase angle of 180° (transit) corresponds to orbital phase of 0.0. We also overplot the detected magnitude of polarization from Berdyugina et al. (2011) and the upper limit from the non-detection from Wiktorowicz (2009), while noting that the central wavelength of the filters used in these observations do not exactly coincide with our model wavelength of $0.44\mu m$. We cannot explain the large value of Berdyugina et al. (2011) using this atmospheric structure, under the assumption that the polarization is due to reflection from the planetary atmosphere. However, we note that the large value of observed polarization still points towards a highly reflective Rayleigh-like atmosphere, since any other type of scattering particle will reduce the degree of polarization.

For a purely Rayleigh scattering atmosphere, the degree of polarization depends only on the single scattering albedo. The single scattering albedo accounts for the presence of absorbing gases in that layer. Since each photon is scattered around till it is either absorbed or leaves the atmosphere, layers with high albedo have multiple scattering that randomizes the plane of polarization and reduces the observed degree of polarization at the top of the atmosphere. One might be tempted to infer, therefore, that low albedos are preferable to reduce multiple scattering and have larger polarization signals. However, as the albedo of the atmosphere is lowered, the planet becomes dimmer with respect to the star. Consequently, the maximum degree of polarization in the star-planet flux becomes lesser. These two competing albedo effects give rise to different behaviors depending on whether the polarization is normalized to the intensity of the star or the reflected intensity of the planet as seen in Figure 2.5.

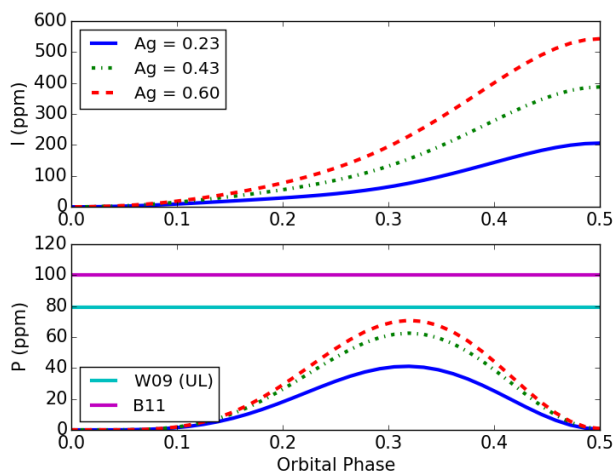


Figure 2.4: Variation in the degree of polarization for reflected light from HD189733b with changes in geometric albedo for a semi-infinite, purely Rayleigh scattering atmosphere. I and P are normalized to direct starlight. The B11 and W09 lines indicate the amplitude of observations from Berdyugina et al. (2011) and the upper limit for non-detection from Wiktorowicz (2009). Orbital phase 0 is mid-transit and 0.5 is mid-eclipse.

For the following cases, we will hold the geometric albedo constant, unless otherwise stated, and vary other atmospheric parameters. We use a value of 0.23, which is the geometric mean of the observed albedos spanning the B-band ($\sim 390 - 480$ nm) as reported in Table 1 of Evans et al. (2013).

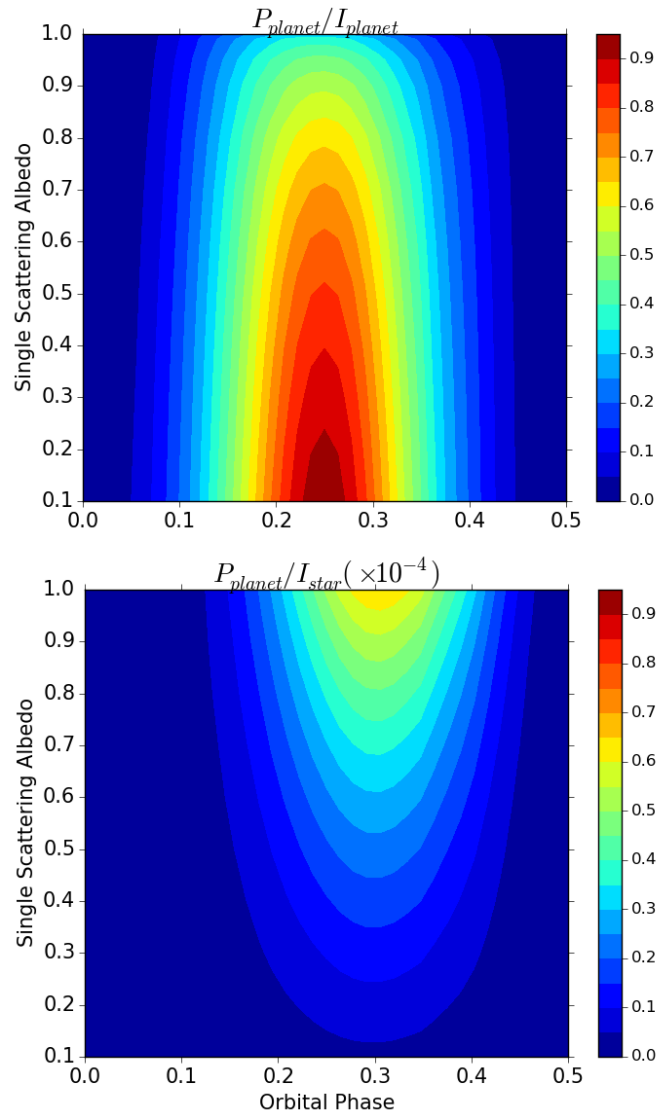


Figure 2.5: Variation in the degree of polarization as a function of single scattering albedo and orbital phase for a semi-infinite Rayleigh scattering atmosphere normalized to reflected light from the planet (top) and direct starlight (bottom). For the former, the highest degree of polarization occurs at low albedo, while for the latter (which is the observable quantity), it occurs at high albedo.

Semi-infinite Hazy Atmospheres

Based on the interpretation of Pont et al. (2013) and others, the atmosphere of HD 189733b consists of a well-mixed Rayleigh scattering haze over several scale heights. To model this, we introduce two types of scattering particles into the atmosphere: spherical particles of size $1\mu m$ and fractal particles of effective size $\sim 0.1\mu m$, composed of 1000 spherical monomers of size $\sim 10nm$. These are similar

in shape to fractal particles used in Z13, but their refractive index is that of silicates, $1.68 + 10^{-4}i$. As in Section 3.2, a single gas+haze layer with an optical depth of 1000 makes up the atmosphere, with an underlying cloud layer. These particles are added such that they contribute to 50% of the optical depth at each atmospheric layer, while the geometric albedo is held constant close to 0.23. This is achieved by setting the single scattering albedo to 0.71 in the Rayleigh case, 0.54 in the Mie case and 0.84 in the fractal case. The resulting curves are shown in Figure 2.6.² The highest polarization is always produced by a non-absorbing, purely Rayleigh scattering atmosphere. The introduction of any particle that deviates from this regime reduces the polarization. Polarization is non-zero at orbital phase 0.5 since the planet is in an orbit whose inclination is not 90° . Therefore, at this orbital phase the phase angle is $\sim 4^\circ$, while polarization is zero for a phase angle of 0° .

A simple reason to explain this effect is that moving from the Rayleigh to Mie regime reduces reflection at quadrature angles and increases preferential forward scattering. Since the polarization peak occurs near quadrature, and there is lower reflection at this point, the total degree of polarization invariably decreases. The fractal particles are characterized by their Mie particle-like intensity curve, which comes from their large effective radius and Rayleigh-like polarization curve, which is due to the small size of individual monomers that make up the aggregate. The Mie-particle haze can be distinguished by a rainbow close to secondary eclipse. Thus, for a given albedo, using a combination of intensity and polarization measurements, it should be possible to determine whether a haze is present, and what type of particles might be present in it. Recent work has begun to place constraints on scattering particle properties (Muñoz and Isaak, 2015). Increasing effective haze particle size decreases the degree of polarization observed. However, it will be tricky to characterize the size of haze particles from the degree of polarization alone without extremely high resolution polarimetric observations ($\Delta P \sim \text{few ppm}$).

Thin Atmospheres Above Cloud Decks

Berdyugina et al., 2011 proposed an atmospheric structure with a thin gas or haze layer on top of a semi-infinite cloud or condensate deck. Since the nature of the cloud or haze layer remains fairly unconstrained in this picture, we create a structure with two layers. In the first case, the top layer is pure gas with an optical depth of 1.0,

² The jagged appearance of the Mie curve is due to disk integrations being carried out at every 5° in orbital phase angle. Smooth curves can be obtained by carrying out integrations at every 1° (Appendix, Figure 14), but the increased computational time does not yield any fundamentally new features.

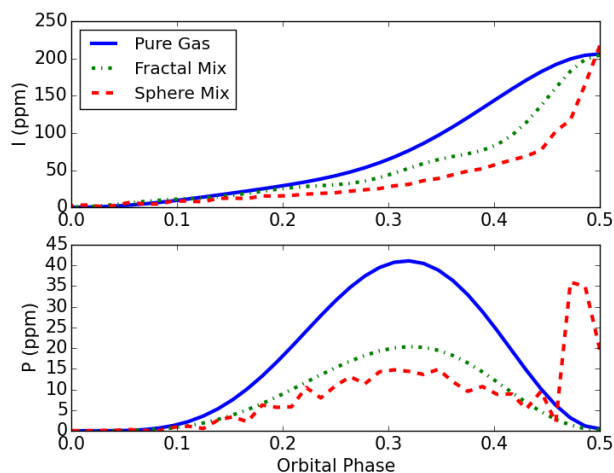


Figure 2.6: Variation in the degree of polarization from reflected light HD189733b system with a semi-infinite pure gas and hazy atmospheres. The particle properties are listed in Table 2.2. The geometric albedo of the planet is forced to remain close to 0.23. B11 and W09 lines indicate the amplitude of observations from Berdyugina et al. (2011) and Wiktorowicz (2009).

and single scattering albedo of 0.7. In the second case the top layer has spherical haze particles and gas, each component contributing to 50% of the optical depth with a total optical depth of 1.0 and single scattering albedo of 0.5. The bottom layer is a cloud with optical depth of 1000 and albedo of 0.7, while the cloud scattering properties are represented by the DHG function mentioned in Table 2.2. Scattering by the cloud produces no net polarization. This is to simulate the effects of scattering by very large cloud particles, of millimeter size. In all cases, the geometric albedo of the planet is maintained close to 0.23. The results are shown in Figure 2.7, we compare these cases to a semi-infinite Rayleigh scattering atmosphere since that is the basic structure that we must distinguish from. Since the geometric albedo is constrained to be the same in all cases, changes in observed intensity are very minor. Thin polarizing layers produce a lower degree of polarization, but the shapes of the curves are the same as those of thick atmospheres of similar composition in the previous section. There is no particular advantage to using polarimetry in this case. This information can also be acquired from a different observational technique, such as transit photometry.

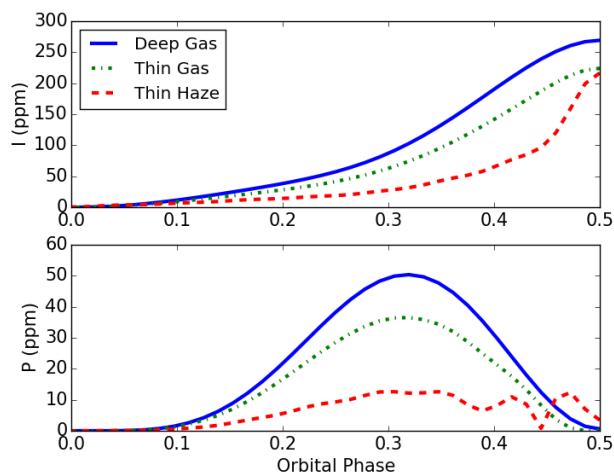


Figure 2.7: Variation in reflected intensity and the degree of polarization for different atmospheric structures of HD 189733b. The intensity curves for a semi-infinite Rayleigh atmosphere (deep gas), thin, clear gas atmosphere (thin gas) and a hazy atmosphere with spherical particles (thin haze) on top of a cloud layer. The haze and cloud properties are mentioned in Table 2.2.

Inhomogeneous Atmospheres

Thus far we have considered homogeneous atmospheres, in both the vertical and horizontal directions, which are idealized cases. We treat one case of horizontal inhomogeneity, where one hemisphere is covered by a haze and the other hemisphere is clear. Such scenarios are of particular interest, since haze and cloud formation process often produce patchy, inhomogeneous regions as seen in the Solar System planets and brown dwarfs. A recent study of the exoplanet Kepler 7b indicates the presence of spatial inhomogeneity where one hemisphere of the planet is more reflective than the other (Demory et al., 2013; Hu et al., 2015), possibly indicating that one hemisphere is covered by patchy clouds while the other is clear.

Here we assume that one hemisphere has a semi-infinite Rayleigh atmosphere (as in Section 3.1) and the other has a semi-infinite hazy atmosphere with spherical particles (as in Section 3.2). The hazy hemisphere has an effective geometric albedo of 0.19, to simulate the effect of greater scattering and absorption, while the geometric albedo of the Rayleigh hemisphere is maintained at 0.23. The hazy hemisphere covers the western part of the planet, lying half over the dayside and half over the nightside, as seen from Earth at secondary eclipse (Figure 2.8). The peak of the reflected intensity is now just before eclipse. Note that the contrast between the homogeneous and inhomogeneous cases is exaggerated in the degree of polarization

at quadrature as compared to the reflected intensity.

Numerically, we create two different atmospheric structures. All longitudes west of the substellar point (which lies at the longitude equal to the scattering angle, α) correspond to the clear structure, eastward are hazy. Thus far, we have used α as defined by Equation 4, which only yields non-negative values. We can get away with only positive α for a homogeneous planet because of longitudinal symmetry. For an inhomogeneous planet, we must have negative α values between $\phi = [\pi, 2\pi]$ to ensure that the correct scattering angles are used. Inhomogeneous atmospheres have been modeled by Karalidi and Stam, 2012; Karalidi, Stam, and Guirado, 2013, by calculating the brightness of homogeneous planets and creating an inhomogeneous planet from their area-weighted averages. One advantage of this method is that we do not need to repeat calculations for different homogeneous planets before arriving at the inhomogeneous case.

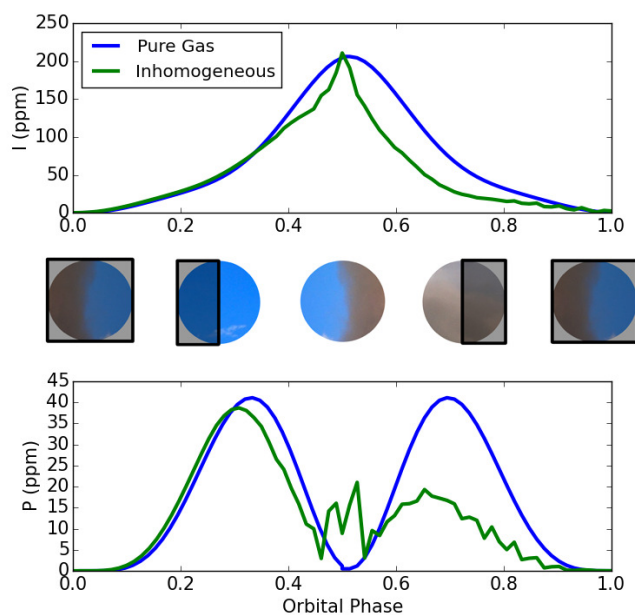


Figure 2.8: Variation in reflected intensity and the degree of polarization as a planet with an inhomogeneous atmosphere completes one orbit compared to a homogeneous, Rayleigh scattering planet. The spheres on top show the planet as seen from Earth at the phases indicated on the abscissa. The dark blue regions are pure Rayleigh scattering, and the greyish regions contain haze. The portion covered by the box indicates the night side of the planet.

Dependence on Orbital Parameters

The range of observed phase angles for one orbit of the exoplanet around the star is set entirely by its inclination. For instance, an inclination of 0° , allows only a constant phase angle of 90° , while an inclination of 90° allows the full range from $0 - 180^\circ$. Intermediate values of inclination allow smaller ranges of phase angles to be observed. Since the inclination can usually be inferred from the transit light curve, we do not consider it a free parameter. However, the longitude of the ascending node cannot always be pin pointed from photometric light curves alone. Figure 2.9 shows an example of two possible transiting orbit candidates for an exoplanet which have the same inclination, but longitudes of the ascending node are of opposite sign albeit same magnitude. The first panel shows the photometric light curve, which is identical for both orbits and cannot be used to distinguish them, while the polarimetric curve, U , clearly shows a change in sign.

2.5 Conclusions

In this paper, we describe a multiple scattering radiative transfer model capable of generating polarized phase curves for reflected light from a range of atmospheric structures. In general, we find that our multiple scattering model cannot produce polarization high enough to match the observations of Berdyugina et al., 2011, agreeing with the findings of Lucas et al., 2009. We also find that clear and hazy atmospheres have observable differences in polarized light. In combination with full orbit reflected intensity phase curves, it might be possible to even distinguish if the haze particles are spheres or aggregates. Furthermore, we also find that spherical haze particles with the refractive of silicate have a rainbow, and corresponding peak in polarization, close to secondary eclipse. In addition, we examine cases where a thin atmosphere is underlain by a semi-infinite cloud layer, and find that they are distinguishable from semi-infinite clear gas atmospheres. The semi-infinite Rayleigh scattering cases were used to put an upper limit on the albedo of HD 189733b in the visible in a companion paper (Wiktorowicz et al., 2015)

In light of growing interest in the exoplanetary community on classifying exoplanetary atmospheres as cloudy (Kreidberg et al., 2014; Knutson et al., 2014) or clear (Fraine et al., 2014), polarimetry has great potential as an observational tool. The inferences of clouds through the transit observations use the absence of features in the spectra to postulate the presence of clouds. The inherent assumption here is that a thick cloud layer must cover a dominant fraction of the planet's atmosphere so as to mask absorption features. Note that clouds, at least those seen within the solar

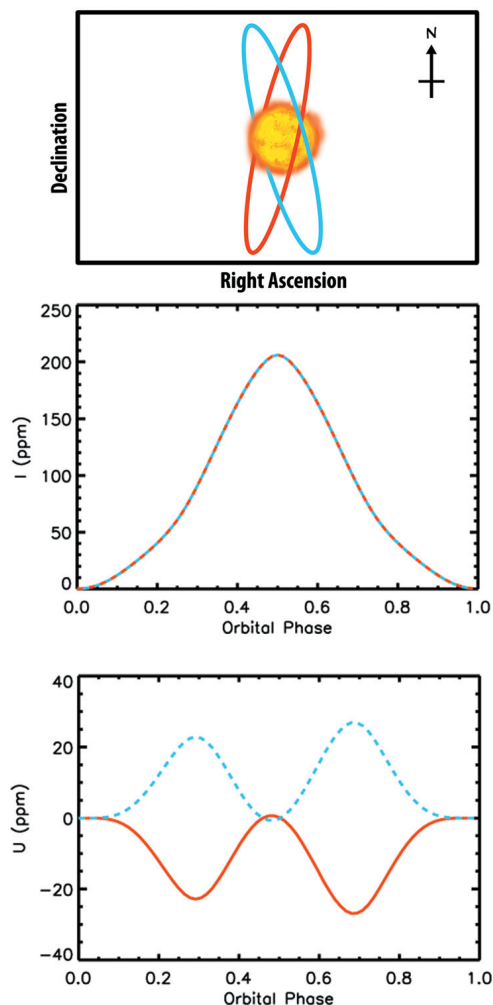


Figure 2.9: The top panel shows a cartoon of two orbits of inclination close to 90 degrees and longitude of the ascending node 16 degrees (red, solid line) and -16 degrees (blue, dashed line) for the HD189733b system as seen from Earth. (Figure is approximate, not to scale, angles are not accurately depicted). The arrow indicates the sense of motion of the planet in the orbit and upwards is North in the sky plane of the Earth. These orbits are indistinguishable from photometry alone, but can be separated using polarimetry. The sign of Stokes parameter U changes, while intensity is invariant for this pair of orbits.

system are never uniformly thick or homogeneous (with the possible exception of Venus). There is no reason to expect that exoplanetary clouds will be any different. Thus, even exoplanets which show absorption features in their transit spectra might still admit patchy clouds in their atmospheres. The detection of patchy clouds is at the limit of current observational capabilities using photometric intensity alone, and must be indirectly inferred (Demory et al., 2013).

We show in this paper that contrasts between clear skies and fully or patchy clouds are significant in polarized light even when the reflected light intensities cannot be differentiated. The locations of hazes and clouds, combined with temperature profiles, can be used to infer the composition of the condensates based on their condensation temperatures. While intensity phase curves may yield information about the size of the scattering particle, polarized curves also give information about the refractive index depending on the position of the rainbow, allowing for additional constraints on chemical composition. The size of cloud particles is indicative of the strength of the updrafts necessary to buoy them, among other factors (see Reutter et al., 2009 for example,) and can provide constraints on the dynamics of exoplanetary atmospheres. The closeness of hot Jupiters to their stars, and the resulting interactions with stellar magnetospheres, can influence the chemistry of the atmosphere. In the solar system, it is thought that the magnetosphere of Jupiter plays a key role in the creation of fractal aggregate hazes near the polar regions (Wong, Yung, and Friedson, 2003).

Better constraints on the scattering properties of atmospheric particles and condensates will allow for the understanding of their formation mechanisms, which are linked to the circulation of the atmosphere itself. Though our model uses overly simplified atmospheric structures in its present form, future work will include spatial variations in atmospheric composition and structure in a more rigorous fashion. One possible extension might be to generate clouds and hazes through a 3D general circulation model and perform vector radiative transfer on the resulting atmospheric structures. As polarimetric observations converge on acceptable values for HD189733b, and new observations become available for other exoplanets, our model can be used in a retrieval framework to constrain atmospheric scattering properties and orbital elements.

2.6 Acknowledgements

We thank David Crisp and Renyu Hu for several insightful comments. This research was supported in part by the President and Director’s Fund at Caltech and by the NAI Virtual Planetary Laboratory grant from the University of Washington to the Jet Propulsion Laboratory and California Institute of Technology. Part of the research described here was carried out at the Jet Propulsion Laboratory, California Institute of Technology, under a contract with the National Aeronautics and Space Administration. X.Z. was supported by the Bisgrove Scholar Program at the University of Arizona.

References

- Bailey, Jeremy (2007). “Rainbows, polarization, and the search for habitable planets”. In: *Astrobiology* 7.2, pp. 320–332.
- Berdyugina, SV, AV Berdyugin, DM Fluri, and V Piirola (2011). “Polarized reflected light from the exoplanet HD189733b: first multicolor observations and confirmation of detection”. In: *The Astrophysical Journal Letters* 728.1, p. L6.
- Berdyugina, Svetlana V, Andrei V Berdyugin, Dominique M Fluri, and Vilppu Piirola (2008). “First detection of polarized scattered light from an exoplanetary atmosphere”. In: *The Astrophysical Journal Letters* 673.1, p. L83.
- Buenzli, Esther and Hans Martin Schmid (2009). “A grid of polarization models for Rayleigh scattering planetary atmospheres”. In: *Astronomy & Astrophysics* 504.1, pp. 259–276.
- Chandrasekhar, Subrahmanyan (1960). *Radiative transfer*. Courier Dover Publications.
- Coulson, Kinsell L, Jitendra V Dave, and Z Sckera (1960). “Tables related to radiation emerging from a planetary atmosphere with Rayleigh scattering”. In:
- Crouzet, Nicolas, Peter R McCullough, Drake Deming, and Nikku Madhusudhan (2014). “Water Vapor in the Spectrum of the Extrasolar Planet HD 189733b. II. The Eclipse”. In: *The Astrophysical Journal* 795.2, p. 166.
- Cuesta, Juan et al. (2013). “Satellite observation of lowermost tropospheric ozone by multispectral synergism of IASI thermal infrared and GOME-2 ultraviolet measurements over Europe”. In: *Atmospheric Chemistry and Physics* 13.19, pp. 9675–9693.
- Danielski, C, P Deroo, IP Waldmann, MDJ Hollis, G Tinetti, and MR Swain (2014). “0.94–2.42 μm Ground-based Transmission Spectra of the Hot Jupiter HD-189733b”. In: *The Astrophysical Journal* 785.1, p. 35.
- Davis, Leverett and Jesse L. Greenstein (May 1949). “The Polarization of Starlight by Interstellar Dust Particles in a Galactic Magnetic Field”. In: *Phys. Rev.* 75 (10), pp. 1605–1605. DOI: 10.1103/PhysRev.75.1605. URL: <http://link.aps.org/doi/10.1103/PhysRev.75.1605>.
- De Rooij, WA and CCAH Van der Stap (1984). “Expansion of Mie scattering matrices in generalized spherical functions”. In: *Astronomy and Astrophysics* 131, pp. 237–248.
- Demory, Brice-Olivier et al. (2013). “Inference of inhomogeneous clouds in an exoplanet atmosphere”. In: *The Astrophysical Journal Letters* 776.2, p. L25.
- Désert, J-M, D Sing, A Vidal-Madjar, G Hébrard, D Ehrenreich, A Lecavelier Des Etangs, V Parmentier, R Ferlet, and GW Henry (2011). “Transit spectrophotometry of the exoplanet HD 189733b-II. New Spitzer observations at 3.6 μm ”. In: *Astronomy & Astrophysics* 526, A12.

- Edwards, DP (1992). “GENLN2: A general line-by-line atmospheric transmittance and radiance model. Version 3.0: Description and users guide”. In: *Rep. NCAR/TN-367-STR. National Center for Atmospheric Research, Boulder, Colorado* 1.
- Evans, Thomas M et al. (2013). “The Deep Blue Color of HD 189733b: Albedo Measurements with Hubble Space Telescope/Space Telescope Imaging Spectrograph at Visible Wavelengths”. In: *The Astrophysical Journal Letters* 772.2, p. L16.
- Fortney, JJ, M Shabram, AP Showman, Y Lian, RS Freedman, MS Marley, and NK Lewis (2010). “Transmission spectra of three-dimensional hot Jupiter model atmospheres”. In: *The Astrophysical Journal* 709.2, p. 1396.
- Fraine, Jonathan, Drake Deming, Bjorn Benneke, Heather Knutson, Andrés Jordán, Néstor Espinoza, Nikku Madhusudhan, Ashlee Wilkins, and Kamen Todorov (2014). “Water vapour absorption in the clear atmosphere of a Neptune-sized exoplanet”. In: *Nature* 513.7519, pp. 526–529.
- Garcia, RDM and CE Siewert (1989). “The FN method for radiative transfer models that include polarization effects”. In: *Journal of Quantitative Spectroscopy and Radiative Transfer* 41.2, pp. 117–145.
- Hansen, James E and JW Hovenier (1974). “Interpretation of the polarization of Venus”. In: *Journal of the Atmospheric Sciences* 31.4, pp. 1137–1160.
- Horak, Henry G (1950). “Diffuse Reflection by Planetary Atmospheres.” In: *The Astrophysical Journal* 112, p. 445.
- Hovenier, Joop W, Cornelis VM van der Mee, and Helmut Domke (2014). *Transfer of polarized light in planetary atmospheres: basic concepts and practical methods*. Vol. 318. Springer Science & Business Media.
- Hu, Renyu, Brice-Olivier Demory, Sara Seager, Nikole Lewis, and Adam P. Showman (2015). “A Semi-analytical Model of Visible-wavelength Phase Curves of Exoplanets and Applications to Kepler- 7 b and Kepler- 10 b”. In: *The Astrophysical Journal* 802.1, p. 51. URL: <http://stacks.iop.org/0004-637X/802/i=1/a=51>.
- Huitson, Catherine M, David K Sing, Alfred Vidal-Madjar, Gilda E Ballester, A Lecavelier Des Etangs, J-M Désert, and Frédéric Pont (2012). “Temperature–pressure profile of the hot Jupiter HD 189733b from HST sodium observations: detection of upper atmospheric heating”. In: *Monthly Notices of the Royal Astronomical Society* 422.3, pp. 2477–2488.
- Jäger, C, J Dorschner, H Mutschke, Th Posch, and Th Henning (2003). “Steps toward interstellar silicate mineralogy-VII. Spectral properties and crystallization behaviour of magnesium silicates produced by the sol-gel method”. In: *Astronomy & Astrophysics* 408.1, pp. 193–204.
- Joos, Franco and Hans Martin Schmid (2007). “Polarimetry of solar system gaseous planets”. In: *Messenger* 130, pp. 27–31.

- Karalidi, T., D. M. Stam, and D. Guirado (2013). “Flux and polarization signals of spatially inhomogeneous gaseous exoplanets”. In: *A&A* 555, A127. DOI: 10.1051/0004-6361/201321492. URL: <http://dx.doi.org/10.1051/0004-6361/201321492>.
- Karalidi, T and DM Stam (2012). “Modeled flux and polarization signals of horizontally inhomogeneous exoplanets applied to Earth-like planets”. In: *Astronomy & Astrophysics* 546, A56.
- Kawabata, K, DL Coffeen, JE Hansen, WA Lane, Makoto Sato, and LD Travis (1980). “Cloud and haze properties from Pioneer Venus polarimetry”. In: *Journal of Geophysical Research: Space Physics (1978–2012)* 85.A13, pp. 8129–8140.
- Kemp, JC, GD Henson, CT Steiner, and ER Powell (1987). “The optical polarization of the Sun measured at a sensitivity of parts in ten million”. In: *Nature* 326.6110, pp. 270–273.
- Knutson, Heather A et al. (2012). “3.6 and 4.5 μm phase curves and evidence for non-equilibrium chemistry in the atmosphere of extrasolar planet HD 189733b”. In: *The Astrophysical Journal* 754.1, p. 22.
- Knutson, Heather A, Björn Benneke, Drake Deming, and Derek Homeier (2014). “A featureless transmission spectrum for the Neptune-mass exoplanet GJ [thinsp] 436b”. In: *Nature* 505.7481, pp. 66–68.
- Knutson, Heather A, David Charbonneau, Nicolas B Cowan, Jonathan J Fortney, Adam P Showman, Eric Agol, Gregory W Henry, Mark E Everett, and Lori E Allen (2009). “Multiwavelength constraints on the day-night circulation patterns of HD 189733b”. In: *The Astrophysical Journal* 690.1, p. 822.
- Kok, Remco J de, Matteo Brogi, Ignas AG Snellen, Jayne Birkby, Simon Albrecht, and Ernst JW de Mooij (2013). “Detection of carbon monoxide in the high-resolution day-side spectrum of the exoplanet HD 189733b”. In: *Astronomy & Astrophysics* 554, A82.
- Kostogryz, N. M., T. M. Yakobchuk, and S. V. Berdyugina (2015). “Polarization in Exoplanetary Systems Caused by Transits, Grazing Transits, and Starspots”. In: *The Astrophysical Journal* 806.1, p. 97. URL: <http://stacks.iop.org/0004-637X/806/i=1/a=97>.
- Kreidberg, Laura et al. (2014). “Clouds in the atmosphere of the super-Earth exoplanet GJ [thinsp] 1214b”. In: *Nature* 505.7481, pp. 69–72.
- Lucas, PW, JH Hough, JA Bailey, M Tamura, E Hirst, and D Harrison (2009). “Planetpol polarimetry of the exoplanet systems 55 Cnc and τ Boo”. In: *Monthly Notices of the Royal Astronomical Society* 393.1, pp. 229–244.
- Lyot, Bernard (1929). “Recherches sur la polarisat de la lumière des planetes et de quelques substances terrestres”. In: *Annales de l’Observatoire de Paris, Section de Meudon* 8. English translation available as NASA TT F-187, p. 1.

- Madhusudhan, Nikku and Adam Burrows (2012). “Analytic models for albedos, phase curves, and polarization of reflected light from exoplanets”. In: *The Astrophysical Journal* 747.1, p. 25.
- McCullough, PR, N Crouzet, D Deming, and N Madhusudhan (2014). “Water vapor in the spectrum of the extrasolar planet HD 189733b. I. The transit”. In: *The Astrophysical Journal* 791.1, p. 55.
- Muñoz, Antonio Garcia and Kate G Isaak (2015). “Probing exoplanet clouds with optical phase curves”. In: *Proceedings of the National Academy of Sciences* 112.44, pp. 13461–13466.
- Pellicori, SF, EE Russell, and LA Watts (1973). “Pioneer imaging photopolarimeter optical system”. In: *Applied optics* 12.6, pp. 1246–1258.
- Pont, F, DK Sing, NP Gibson, S Aigrain, G Henry, and N Husnoo (2013). “The prevalence of dust on the exoplanet HD 189733b from Hubble and Spitzer observations”. In: *Monthly Notices of the Royal Astronomical Society*, stt651.
- Pont, Frédéric et al. (2007). “Hubble Space Telescope time-series photometry of the planetary transit of HD 189733: no moon, no rings, starspots”. In: *Astronomy & Astrophysics* 476.3, pp. 1347–1355.
- Prather, MJ (1974). “Solution of the inhomogeneous Rayleigh scattering atmosphere”. In: *The Astrophysical Journal* 192, pp. 787–792.
- Redfield, Seth, Michael Endl, William D Cochran, and Lars Koesterke (2008). “Sodium absorption from the exoplanetary atmosphere of HD 189733b detected in the optical transmission spectrum”. In: *The Astrophysical Journal Letters* 673.1, p. L87.
- Reutter, Philipp, H Su, J Trentmann, Martin Simmel, Diana Rose, SS Gunthe, H Wernli, MO Andreae, and U Pöschl (2009). “Aerosol-and updraft-limited regimes of cloud droplet formation: influence of particle number, size and hygroscopicity on the activation of cloud condensation nuclei (CCN)”. In: *Atmospheric Chemistry and Physics* 9.18, pp. 7067–7080.
- Schmid, HM (1992). “Montecarlo Simulations of Raman Scattered OVI Emission Lines in Symbiotic Stars”. In: *Astronomy and Astrophysics* 254, p. 224.
- Seager, S, BA Whitney, and DD Sasselov (2000). “Photometric light curves and polarization of close-in extrasolar giant planets”. In: *The Astrophysical Journal* 540.1, p. 504.
- Sengupta, Sujan (2008). “Cloudy Atmosphere of the Extrasolar Planet HD 189733b: A Possible Explanation of the Detected B-Band Polarization”. In: *The Astrophysical Journal Letters* 683.2, p. L195.
- Siewert, CE (2000). “A discrete-ordinates solution for radiative-transfer models that include polarization effects”. In: *Journal of Quantitative Spectroscopy and Radiative Transfer* 64.3, pp. 227–254.

- Sing, D. K. et al. (2011). “Hubble Space Telescope transmission spectroscopy of the exoplanet HD 189733b: high-altitude atmospheric haze in the optical and near-ultraviolet with STIS”. In: *Monthly Notices of the Royal Astronomical Society* 416.2, pp. 1443–1455. DOI: 10.1111/j.1365-2966.2011.19142.x. eprint: <http://mnras.oxfordjournals.org/content/416/2/1443.full.pdf+html>. URL: <http://mnras.oxfordjournals.org/content/416/2/1443.abstract>.
- Sing, David K, J-M Désert, A Lecavelier Des Etangs, GE Ballester, A Vidal-Madjar, V Parmentier, G Hebrard, and GW Henry (2009). “Transit spectrophotometry of the exoplanet HD 189733b-I. Searching for water but finding haze with HST NICMOS”. In: *Astronomy & Astrophysics* 505.2, pp. 891–899.
- Smith, Peter H and Martin G Tomasko (1984). “Photometry and polarimetry of Jupiter at large phase angles: II. Polarimetry of the South Tropical Zone, South Equatorial Belt, and the polar regions from the Pioneer 10 and 11 missions”. In: *Icarus* 58.1, pp. 35–73.
- Spurr, Robert JD (2006). “VLIDORT: A linearized pseudo-spherical vector discrete ordinate radiative transfer code for forward model and retrieval studies in multilayer multiple scattering media”. In: *Journal of Quantitative Spectroscopy and Radiative Transfer* 102.2, pp. 316–342.
- Stam, DM (2008). “Spectropolarimetric signatures of Earth-like extrasolar planets”. In: *Astronomy & Astrophysics* 482.3, pp. 989–1007.
- Stam, DM, WA De Rooij, G Cornet, and JW Hovenier (2006). “Integrating polarized light over a planetary disk applied to starlight reflected by extrasolar planets”. In: *Astronomy & Astrophysics* 452.2, pp. 669–683.
- Stam, DM, JW Hovenier, and LBFM Waters (2004). “Using polarimetry to detect and characterize Jupiter-like extrasolar planets”. In: *Astronomy & Astrophysics* 428, pp. 663–672.
- Stamnes, Knut, Si-Chee Tsay, Warren Wiscombe, and Istvan Laszlo (2000). “DISORT, a general-purpose Fortran program for discrete-ordinate-method radiative transfer in scattering and emitting layered media: documentation of methodology”. In: *Goddard Space flight center, NASA*.
- Swain, Mark R, Gautam Vasisht, and Giovanna Tinetti (2008). “The presence of methane in the atmosphere of an extrasolar planet”. In: *Nature* 452.7185, pp. 329–331.
- Swain, MR et al. (2009). “Water, methane, and carbon dioxide present in the dayside spectrum of the exoplanet HD 209458b”. In: *The Astrophysical Journal* 704.2, p. 1616.
- Tinetti, Giovanna et al. (2007). “Water vapour in the atmosphere of a transiting extrasolar planet”. In: *Nature* 448.7150, pp. 169–171.

- Tomasko, Martin G and Peter H Smith (1982). “Photometry and polarimetry of Titan: Pioneer 11 observations and their implications for aerosol properties”. In: *Icarus* 51.1, pp. 65–95.
- Tomasko, MG, L Doose, S Engel, LE Dafoe, R West, M Lemmon, E Karkoschka, and C See (2008). “A model of Titan’s aerosols based on measurements made inside the atmosphere”. In: *Planetary and Space Science* 56.5, pp. 669–707.
- Torres, Guillermo, Joshua N Winn, and Matthew J Holman (2008). “Improved parameters for extrasolar transiting planets”. In: *The Astrophysical Journal* 677.2, p. 1324.
- Triaud, Amaury HMJ et al. (2010). “Spin-orbit angle measurements for six southern transiting planets-New insights into the dynamical origins of hot Jupiters”. In: *Astronomy & Astrophysics* 524, A25.
- Wiktorowicz, Sloane J (2009). “Nondetection of Polarized, Scattered Light from the HD 189733b Hot Jupiter”. In: *The Astrophysical Journal* 696.2, p. 1116.
- Wiktorowicz, Sloane J, Larissa A Nofi, Daniel Jontof-Hutter, Pushkar Kopparla, Gregory P Laughlin, Ninos Hermis, Yuk L Yung, and Mark R Swain (2015). “A ground-based Albedo Upper Limit for HD 189733b from Polarimetry”. In: *The Astrophysical Journal* 813.1, p. 48.
- Williams, Darren M and Eric Gaidos (2008). “Detecting the glint of starlight on the oceans of distant planets”. In: *Icarus* 195.2, pp. 927–937.
- Wong, Ah-San, Yuk L Yung, and A James Friedson (2003). “Benzene and haze formation in the polar atmosphere of Jupiter”. In: *Geophysical research letters* 30.8.
- Xi, X., V. Natraj, R. L. Shia, M. Luo, Q. Zhang, S. Newman, S. P. Sander, and Y. L. Yung (2015). “Simulated retrievals for the remote sensing of CO₂, CH₄, CO, and H₂O from geostationary orbit”. In: *Atmospheric Measurement Techniques Discussions* 8.6, pp. 5809–5846. DOI: 10.5194/amtd-8-5809-2015. URL: <http://www.atmos-meas-tech-discuss.net/8/5809/2015/>.
- Zhang, X, RA West, D Banfield, and YL Yung (2013). “Stratospheric aerosols on Jupiter from Cassini observations”. In: *Icarus* 226.1, pp. 159–171.

POLARIZATION OF THE WASP-12 SYSTEM: ALBEDOS AND CLOUD COMPOSITION FROM SIMPLE MODELS

3.1 Abstract

WASP-12b is one of the hottest known exoplanets, with an equilibrium temperature around 2500 K and a period of 1.1 days. Due to its extreme temperature, it was initially expected that no condensate clouds could form in the atmosphere. However, a slope in the visible region of the transmission spectrum of this planet, as well as muted water absorption features, have hinted at the presence of a thick cloud spanning several scale heights in its atmosphere around the day-night boundary of this planet. Here we explore the polarimetric signals observable under both clear and cloudy sky conditions. Under the clear sky model, the polarization amplitude allows us to constrain the geometric albedo of the planet. However, interpreting this measurement as the result of scattering by cloud particles allows us to derive particle size constraints for different scattering cloud constituents, in addition to constraining the geometric albedo.

3.2 Introduction

There is an increasing consensus on the presence of hazes in the atmosphere of WASP-12b (Sing et al., 2013; Mandell et al., 2013; Kreidberg et al., 2015; Iyer et al., 2016). However, the extent of the observable atmosphere dominated by such hazes is variable and a function of several variables such as the equilibrium temperature, atmospheric chemistry and strength of uplifts and zonal flows (see for e.g., Parmentier et al., 2016). Detailed cloud formation modeling of WASP-12b indicates that Al_2O_3 and $CaTiO_3$ are the most likely candidates to condense as hazes in the upper atmosphere (Wakeford et al., 2016).

We adapt the model described in the previous section to produce polarized light phase curves for WASP-12b, a summary of the important parameters is provided in Table 3.1. Particle refractive indices were taken from Kitzmann and Heng, 2017, and the planetary and orbital properties from "<http://exoplanets.org>" (Han et al., 2014) and "<http://exoplanet.eu>" (Schneider et al., 2011). For all simulations, the upper atmosphere is assumed to be horizontally and vertically homogeneous, in the region relevant to observing scattered light. Thus, clouds or gas are included as

optically thick (optical depth of ~ 1000) horizontal layers over a fully absorbing surface. The actual atmosphere of the planet is likely to have patchy clouds with a spatially variable vertical extent, we do not expect initial polarization data to resolve such fine details. Therefore, we focus on very simple end member models with the aim of making a binary distinction between scattering from a predominantly cloudy or clear atmosphere. The next section describes various simulations using our polarized radiative transfer model. The section following that discusses the implications of an observed signal, and how it may be used to place constraints on geometric albedo and particle composition and size.

Table 3.1: Summary of Parameters Used

Function	Parameter	Value
Wavelength		$0.44 \mu\text{m}$
Refractive Index	Perovskite (CaTiO_3)	$2.43 + 0.005i$
	Corundum (Al_2O_3)	$1.58 + 0.04i$
Planetary Radius		$1.736R_j$
Orbital Radius		0.0229 AU
Inclination		82.5°

3.3 Results and Discussion

Since the expected region of haze condensation is only around the limbs, much of the dayside surface could be dominated by Rayleigh scattering. Various metal oxides and silicates present in the gas phase on the dayside can contribute to absorption, reducing the albedo of an otherwise pure hydrogen atmosphere. The shape of the curve for Rayleigh scattering is well known, with intensity scaling linearly with albedo and polarization approximately quadratically (Fig 3.1, also see next figure). Given that the shape of the curve is similar for all albedos, with peaks around quadrature, peak polarization signal amplitude therefore has a one-to-one correspondence with geometric albedo (Fig 3.2). Thus, for a clear sky planet, a polarization measurement around quadrature will yield a direct constraint on its geometric albedo. Cloud condensation modeling indicates that the dayside of WASP-12b should be mostly cloudless (Wakeford et al., 2016). However, we do not have observations to constrain all model parameters, and model uncertainties could be substantial. Therefore, we also consider cases where the dayside atmospheric scattering is dominated by cloud particles. Fig 3.3 shows curves for corundum (top) and perovskite (bottom) cloud particles of various sizes. The Mie scattering

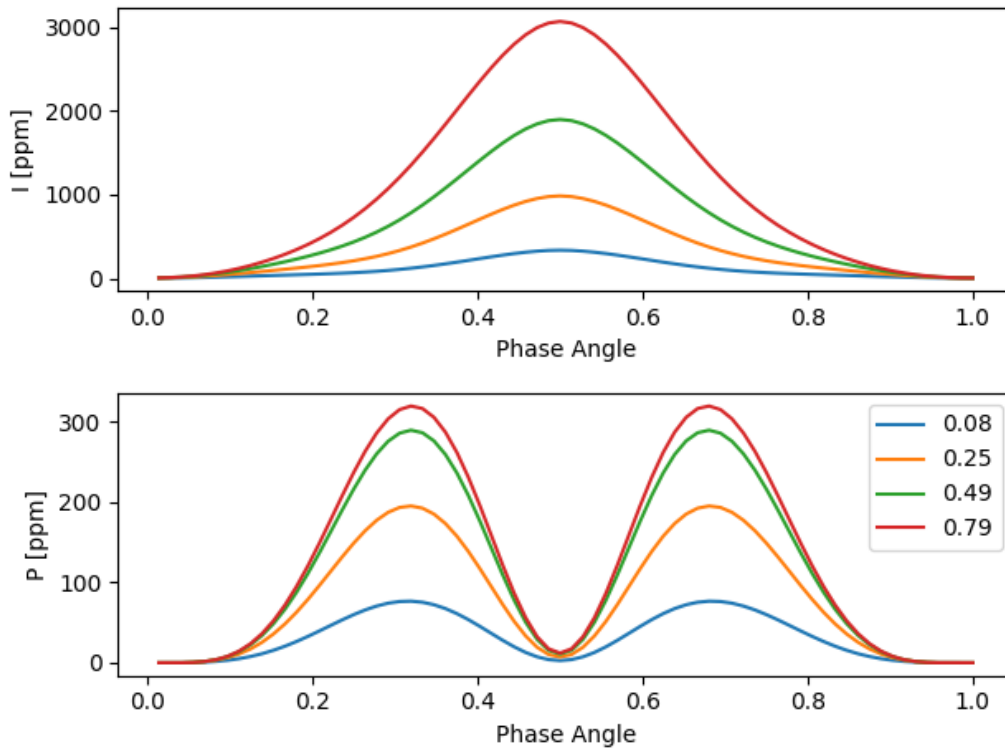


Figure 3.1: Scattered light intensity and polarization for Rayleigh scattering atmospheres on WASP-12b with various geometric albedos. Polarization is expressed as a fraction of direct unscattered starlight in units of parts per million (ppm).

phase functions are calculated using Mie theory, with the Meerhoff Mie program version 3.1 (De Rooij and Van der Stap, 1984). The particle size distribution is log normal (index size distribution 2 in the Meerhoff code), with the variance always set to $\frac{1}{10}$ of the effective particle size. The shape of the phase curve, along with the location and magnitude of peak polarization are functions of both particle size and refractive index. Since polarization is a non-trivial function of particle size, we systematically plot the geometric albedo and peak polarization for corundum and perovskite particles as a function of particle size (Figs 3.4 and 3.5). As expected, the quantities of interest are most variable around $0.07\mu m$ where the particle size parameter ($\frac{2\pi r}{\lambda}$, r is the radius and λ is the wavelength) approaches unity for a wavelength of $0.44\mu m$. There is secondary peak in polarization between $0.1 - 1\mu m$, possibly the result of a Mie scattering resonance. We note from these figures that even with a given geometric albedo and maximum polarization amplitude, the particle size can still be degenerate.

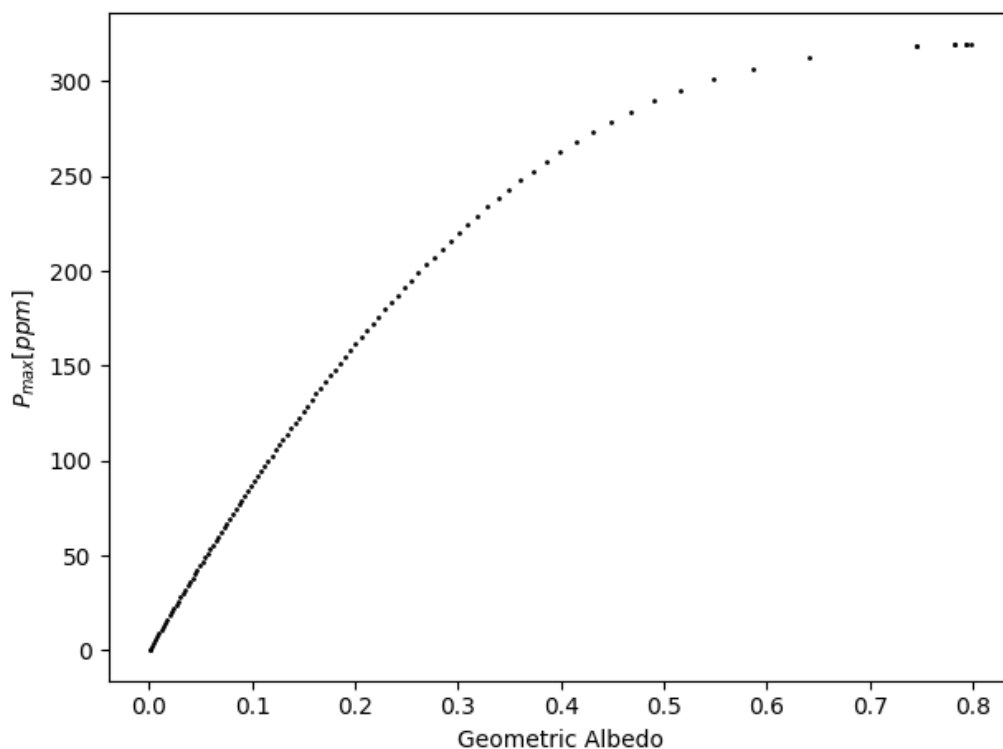


Figure 3.2: Variation of the peak polarization amplitude due to scattering a clear atmosphere on WASP-12b with geometric albedo. A given value of peak polarization translates directly to a single geometric albedo value of the planet and can be compared to measurements from other techniques such as secondary eclipse (Bell et al., 2017).

3.4 Conclusions

We explore the two end member cases (clear and cloudy) for the atmospheric structure of the very hot exoplanet, WASP-12b. A clear atmosphere allows us to unambiguously determine geometric albedo of the planet from the maximum polarization amplitude. Modeling scattering from a cloudy atmosphere allows us to derive cloud particle composition given a particle size constraint (from transits) and polarization amplitude. However, particle size is still somewhat degenerate, and will likely require multiwavelength observations in both photometry (transits, secondary eclipses and maybe even phase curves) and polarimetry to be tightly constrained. We also note that the models used here are highly simplified to match the state of observations at the current time. As better data becomes available in the future, the use of more nuanced atmospheric structures will likely become necessary.

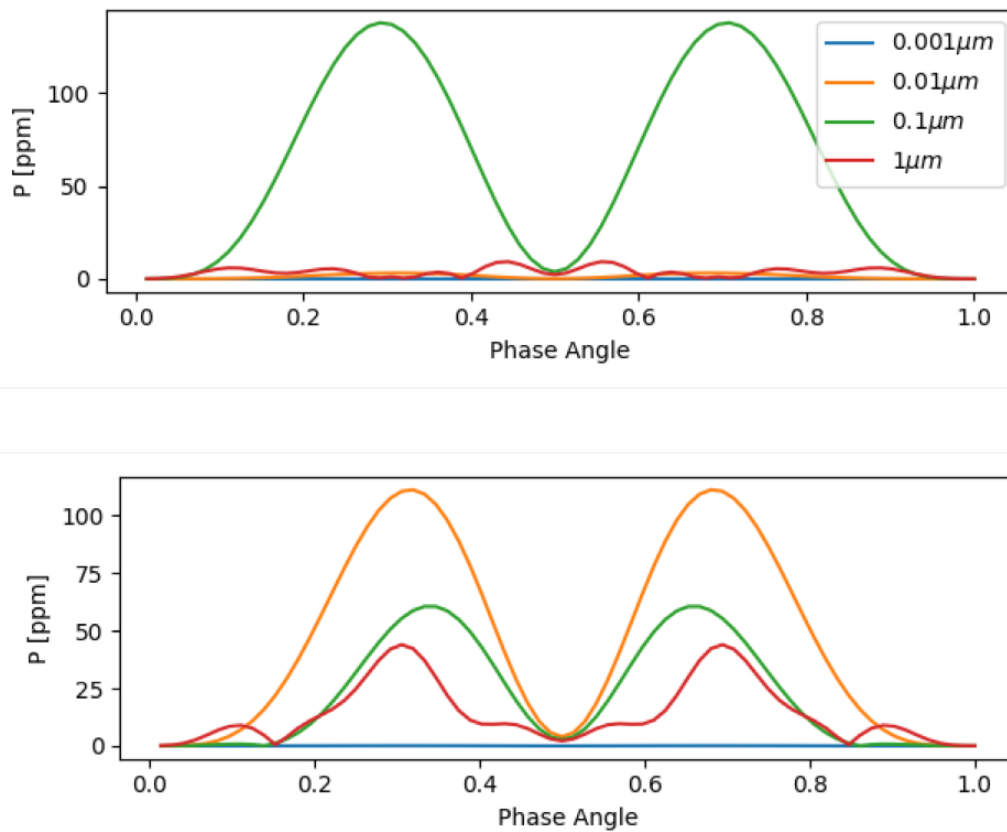


Figure 3.3: Polarized light curves for corundum (top) and perovskite (bottom) cloud scattering on WASP-12b. Note that peak polarization is a non-monotonic function of particle size.

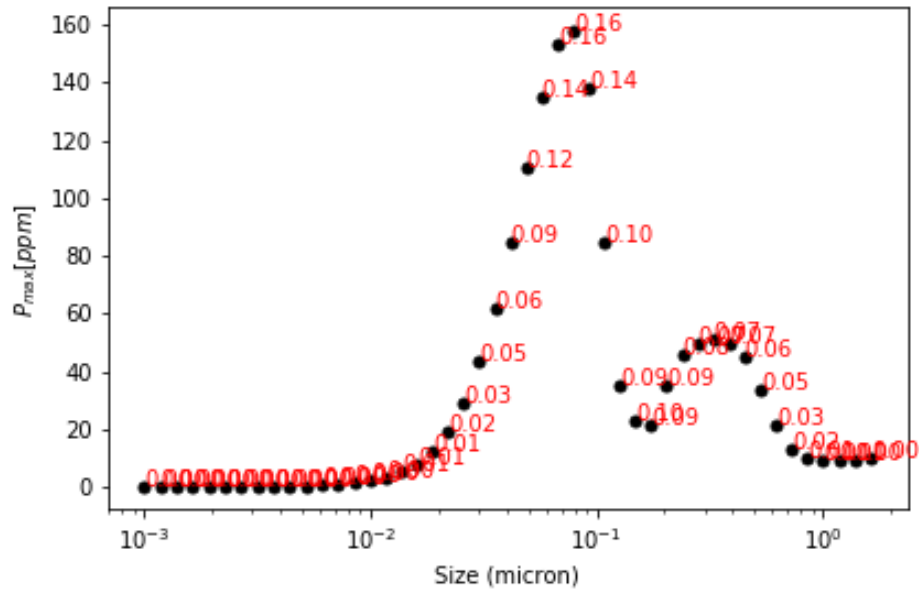


Figure 3.4: Maximum polarization from the scattering of light by a thick atmospheric cloud on WASP-12b for cloud composed of Al_2O_3 particles of various sizes. The numbers next to the points on the plot indicate geometric albedos for WASP-12b.

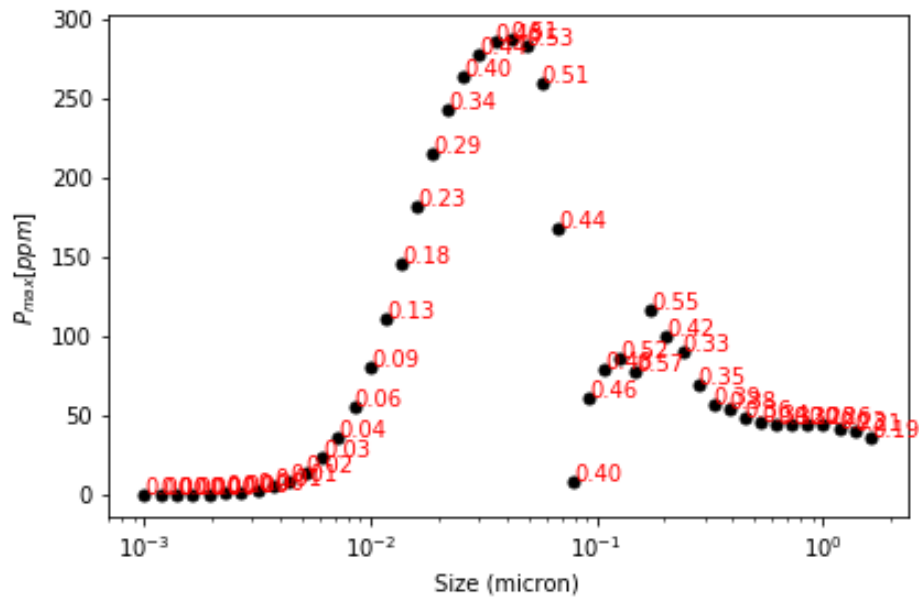


Figure 3.5: Same as 3.4, but for a cloud of $CaTiO_3$ particles.

3.5 Acknowledgments

We would like to acknowledge useful discussions with Vijay Natraj, Dave Crisp, Tiffany Kataria, Suniti Sanghavi and others. Funding support from VPL, JPL and PDF at Caltech.

References

- Bell, Taylor J et al. (2017). “The Very Low Albedo of WASP-12b from Spectral Eclipse Observations with Hubble”. In: *The Astrophysical Journal Letters* 847.1, p. L2.
- De Rooij, WA and CCAH Van der Stap (1984). “Expansion of Mie scattering matrices in generalized spherical functions”. In: *Astronomy and Astrophysics* 131, pp. 237–248.
- Han, Eunhyu, Sharon X Wang, Jason T Wright, Y Katherina Feng, Ming Zhao, Onsi Fakhouri, Jacob I Brown, and Colin Hancock (2014). “Exoplanet orbit database. II. Updates to exoplanets. org”. In: *Publications of the Astronomical Society of the Pacific* 126.943, p. 827.
- Iyer, Aishwarya R, Mark R Swain, Robert T Zellem, Michael R Line, Gael Roudier, Graça Rocha, and John H Livingston (2016). “A characteristic transmission spectrum dominated by H₂O applies to the majority of HST/WFC3 exoplanet observations”. In: *The Astrophysical Journal* 823.2, p. 109.
- Kitzmann, Daniel and Kevin Heng (2017). “Optical properties of potential condensates in exoplanetary atmospheres”. In: *Monthly Notices of the Royal Astronomical Society* 475.1, pp. 94–107.
- Kreidberg, Laura et al. (2015). “A detection of water in the transmission spectrum of the hot Jupiter WASP-12b and implications for its atmospheric composition”. In: *The Astrophysical Journal* 814.1, p. 66.
- Mandell, Avi M, Korey Haynes, Evan Sinukoff, Nikku Madhusudhan, Adam Burrows, and Drake Deming (2013). “Exoplanet transit spectroscopy using WFC3: WASP-12 b, WASP-17 b, and WASP-19 b”. In: *The Astrophysical Journal* 779.2, p. 128.
- Parmentier, Vivien, Jonathan J Fortney, Adam P Showman, Caroline Morley, and Mark S Marley (2016). “Transitions in the cloud composition of hot Jupiters”. In: *The Astrophysical Journal* 828.1, p. 22.
- Schneider, Jean, Cyrill Dedieu, Pierre Le Sidaner, Renaud Savalle, and Ivan Zolotukhin (2011). “Defining and cataloging exoplanets: the exoplanet. eu database”. In: *Astronomy & Astrophysics* 532, A79.
- Sing, David K et al. (2013). “HST hot-Jupiter transmission spectral survey: evidence for aerosols and lack of TiO in the atmosphere of WASP-12b”. In: *Monthly Notices of the Royal Astronomical Society* 436.4, pp. 2956–2973.

Wakeford, H R, Channon Visscher, Nikole K Lewis, Tiffany Kataria, Mark S Marley, Jonathan J Fortney, and Avi M Mandell (2016). “High temperature condensate clouds in super-hot Jupiter atmospheres”. In: *Monthly Notices of the Royal Astronomical Society*, stw2639.

*Chapter 4***OBSERVING OCEANS IN TIGHTLY PACKED PLANETARY SYSTEMS: PERSPECTIVES FROM POLARIZATION MODELING OF THE TRAPPIST-1 SYSTEM****4.1 Abstract**

The recently discovered TRAPPIST-1 system is exciting due to the possibility of several rocky, Earth-sized planets harboring liquid water on their surface. To assess the detectability of oceans on these planets, we model the disk integrated phase curves and polarization signals for planets in this system for reflected starlight. We examine four cases: (1) dry planet, (2) cloud-covered planet, (3) planet with regional-scale oceans, and (4) planet with global oceans. Polarization signals are strongest for optically thin atmospheres over widespread oceans, with the degree of polarization being up to 90% for a single planet. In cases where reflected light from different planets in a tightly packed system cannot be separated, observing in polarized light allows for up to a tenfold increase in star-planet contrast compared to photometric observations alone. Planned telescopes like ELT and LUVOIR may be capable of observing glint (specularly reflected starlight) from Earth-like planets around Sun-like stars, and if equipped with a polarimeter can significantly improve our ability to detect and study oceans on rocky exoplanets.

4.2 Introduction

The discovery of the TRAPPIST-1 system, with several rocky planets tightly packed in a resonant chain of orbits around an ultracool dwarf star (effective temperature of about 2550 K), is the first of its kind (Gillon et al., 2017; Luger et al., 2017). The close-in orbits of these planets combined with the cool temperature of the star allow several of these planets to receive stellar insolation levels comparable to the solar flux at Earth. This circumstance has inspired several studies on different aspects of habitability for these planets such as atmospheric greenhouse effects (Wolf, 2017; Meadows et al., 2017), surface UV fluxes (O'Malley-James and Kaltenegger, 2017) and even some studies on the effects of vegetation (Alberti et al., 2017) and possible exchange of biological matter between planets in the system (Lingam and Loeb, 2017).

In this work, we focus on finding directly detectable signals for liquid water (such as

specularly reflected starlight from the surface, commonly known as glint) for planets in this system. Looking for glint in reflected starlight was first proposed by Cowan et al. (2009) and Robinson, Meadows, and Crisp (2010). However, it is possible to have false positives mimicking glint from a liquid ocean surface occurring due to reflection off ice or snow at high latitudes (Cowan, Abbot, and Voigt, 2012). In such cases, an additional piece of information from polarization can help resolve the degeneracy. Stam (2008) was the first to propose a search for glint in polarized light. Later work explored the parameter space of various atmospheric and surface conditions in the context of detectability, and concluded that the near IR atmospheric windows from 1.55–1.75 μm and 2.1–2.3 μm were the most favorable to detect glint reflection from the surface for an Earth like atmosphere with clouds and aerosols (Zugger et al., 2010; Zugger et al., 2011).

Recent work on modeling the climates of the TRAPPIST-1 planets found that planet d was most likely to have liquid water, with the outer planets being more likely to be frozen over (Alberti et al., 2017). However, other work on estimating the water loss rates on the planets of this system indicate that planets e to h can hold onto some of their water, while the inner planets have loss rates that are too high to expect oceans to exist (Bourrier et al., 2017). We therefore focus much of our modeling on TRAPPIST-1e, as a likely candidate for possessing some liquid water on the basis of these studies.

In the following section, we describe our vector radiative transfer model. Then we present polarized phase curves for a few cases of an ocean on the surface, and the magnitude of an observable signal for various atmospheric conditions. Following that, we explore the issues associated with isolating the glint signal from a single planet in a tightly packed multiplanet system. We discuss our findings and implications for future observations in the final section.

4.3 Model

A detailed description of the polarized radiative transfer model and its validation can be found in an earlier paper (Kopparla et al., 2016), but we summarize it here for convenience. The core of the model is the one-dimensional, multiple scattering, vector radiative transfer model, VLIDORT (Spurr, 2006). The planet’s surface is divided up into a grid of boxes (typically 64 boxes) based on a quadrature scheme (Horak, 1950), and the radiation field is derived at each box using a plane parallel one dimensional atmosphere. The radiation fields from each box are then summed over

the entire surface to give the disc integrated intensity and polarization values. To simulate ocean-covered surfaces, we have used the Cox-Munk ocean reflection glint surface model (Cox and Munk, 1954) capability in VLIDORT. The model outputs the Stokes parameters I (intensity), Q and U (linear polarization parameters) and V (circular polarization parameter). For most of our results, we will mostly deal with Stokes parameter I and the degree of polarization, P is defined as

$$P = \frac{\sqrt{Q^2 + U^2}}{I} \quad (4.1)$$

The Cox-Munk model uses the liquid's refractive index and the surface wind speed (as a measure of the surface roughness) as inputs to calculate the reflectance function. In the example of a glint spot as simulated by the model, (shown in Fig 4.1), the glint spot is strongest when the viewing zenith angle (VZA) is equal to the solar zenith angle (SZA) at an azimuthal angle (AZM) of 0. Increasing the wind speed parameter in the Cox-Munk model causes the water surface to become rougher, and smears out the glint spot to a wider range of angles. For any realistic planet, the ocean surface roughness and winds vary significantly and using a single wind speed is a simplification. Given that we are only able to observe disc-integrated brightnesses from super Earths at best, a single surface roughness parameter is a tolerable approximation. This can also be thought of as the wind speed in the vicinity of the specular point on the sphere that glint reflectance will be most sensitive to.

For simulating the dry land surfaces in our models, we use a Lambertian surface. Land surfaces on Earth have a wide variety of bidirectional reflectance functions (BRDFs) depending on composition, mineralogy, surface roughness, vegetation and so forth (Bicheron and Leroy, 2000; Bacour and Bréon, 2005, see eg.,). Even for surfaces made of one component, such as snow, there is still significant variability based on viewing and lighting angles, wavelength, size and shape of snow grains (Dumont et al., 2010). While we expect some of the surface to be covered in snow based on the expected equilibrium temperatures for some of the TRAPPIST-1 planets, we are still very far from being able to observationally constrain such details as the coverage and properties of snow on the surface. Therefore, in line with our lack of information, we use a very simple surface model: an isotropic (Lambertian) surface with an albedo of 0.2 (typical land surfaces on the Earth have albedos between 0.05-0.4, we simply chose a middling value). Lambertian surfaces are commonly used as first order approximations for modern high resolutions retrievals

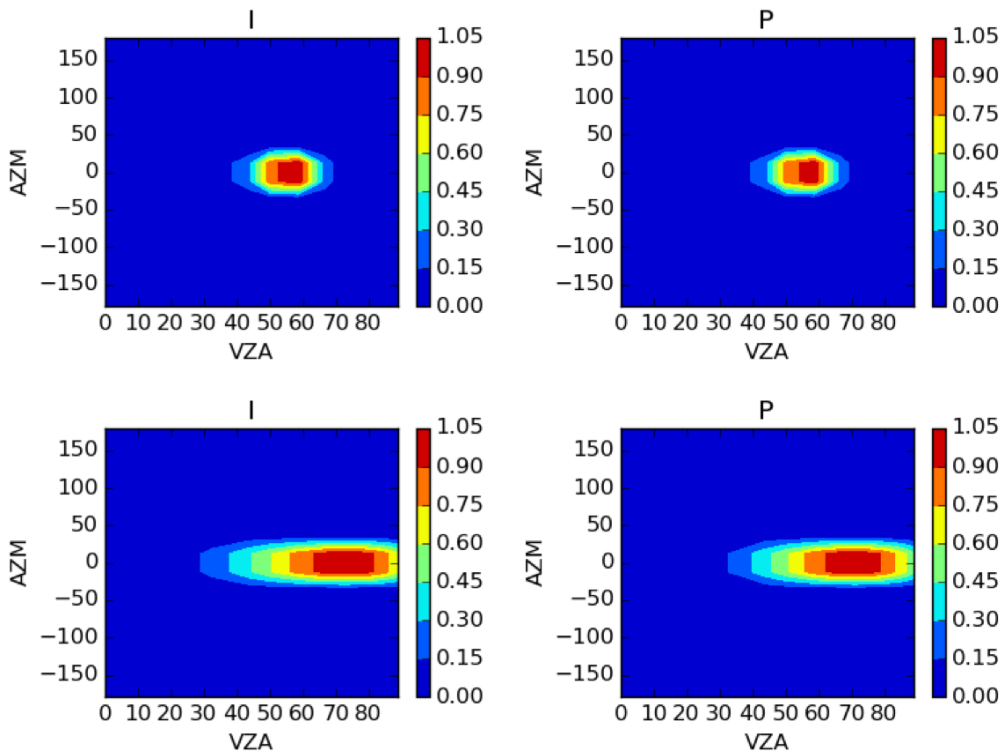


Figure 4.1: Normalized Stokes parameter I and degree of polarization P for a Cox-Munk glint surface under a very thin 1-D Rayleigh scattering atmosphere (optical depth 0.01) for a variety of values of VZA and AZM. SZA = 60 deg. The wind speed is 1 m/s for the plots in the top row, and 10 m/s for those in the bottom row.

of Earth surface albedos from remote sensing instruments such as MODIS (Wang et al., 2010).

4.4 Results

Atmospheric Effects

Atmospheric absorption and scattering are complex effects, with strong dependencies on wavelength, observing geometry and atmospheric composition. Since we are interested in glint signals from the surface, it makes sense to choose wavelengths which the atmosphere is most transparent to. On Earth, for instance, there are several such atmospheric windows in the near infrared regions, where the optical depth is of order 10^{-2} (Fig 4.2). The window locations may be different for TRAPPIST-1 planets, depending on the makeup of their atmospheres. Ascertaining the chemical compositions of atmospheres on these planets is outside the scope of this paper.

Since we do not know where the window regions are, it is likely that glint obser-

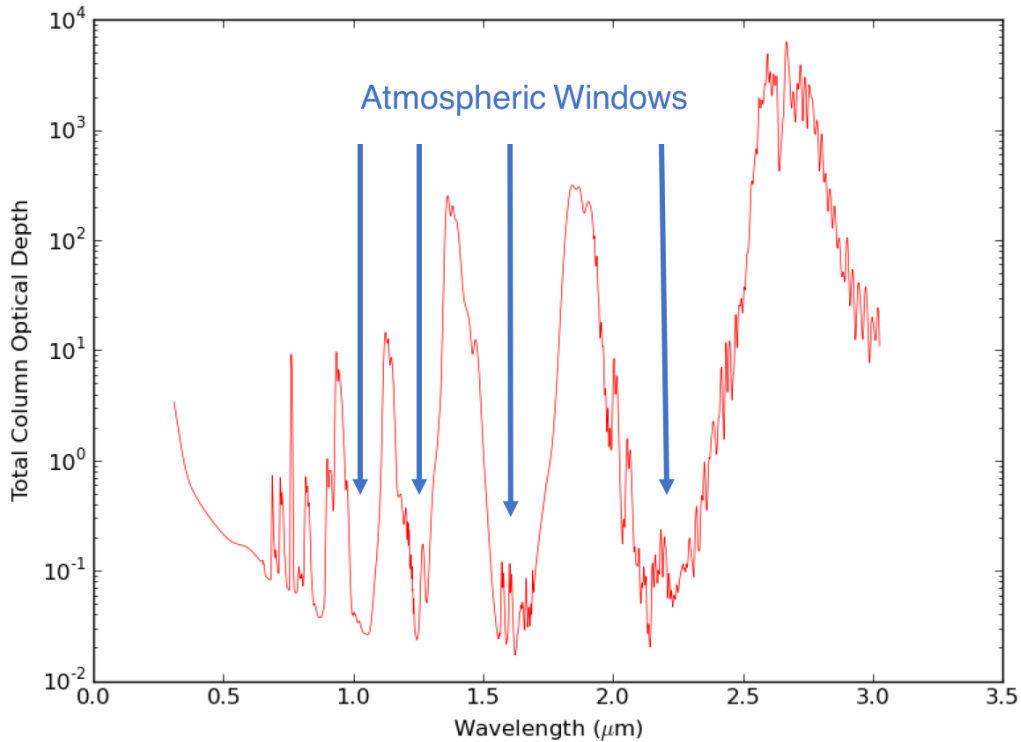


Figure 4.2: A typical total column optical depth spectrum of the Earth's atmosphere between the wavelengths 0.3 and 3 μm with Rayleigh scattering, gas and aerosol extinction but no clouds. Note that an atmosphere can be optically thin in a given wavelength range ("atmospheric window" regions) even with a large column air mass. This profile was generated by the WRF-Chem chemistry and transport model for a location over the continental US (Grell et al., 2005; Fast et al., 2006; Peckham et al., 2011)

vations will contain some amount of atmospheric absorption. In such cases, it is important to know how thick an atmosphere a planet can have before the glint signal is completely obscured. To estimate this, we consider the effects of a Rayleigh scattering atmosphere on top of a glinting ocean, with varying optical thicknesses (Fig 4.3). Both scattering and absorption contribute to the atmospheric optical depth. While atmospheric scattering can change both the degree of polarization and the phase angle of peak polarization, atmospheric absorption will mostly attenuate the overall signal. Since we are interested in glint signals from the surface, it makes sense to choose wavelengths where the atmosphere is most transparent. Other than the straightforward interpretation of optical depth being an indicator of atmospheric mass or thickness, this can also be thought of as the difference between observing at 1.5 μm and 2 μm in an Earth-like atmosphere (Fig 4.2), where the optical depth

changes by a factor of 10000. In the thin atmosphere limit, the glint signal is clearly visible at crescent phases (phase angles 0.1 and 0.9), whereas the glint signal is almost entirely absent in the thick atmospheres. The high degree of polarization in the thick atmosphere cases comes from Rayleigh scattering in the atmosphere. The thick atmosphere planets are also much brighter than those with thin atmospheres, since the atmospheres have no absorption (single scattering albedo of 0.9999) and the surface is relatively dark at angles away from the glint spot.

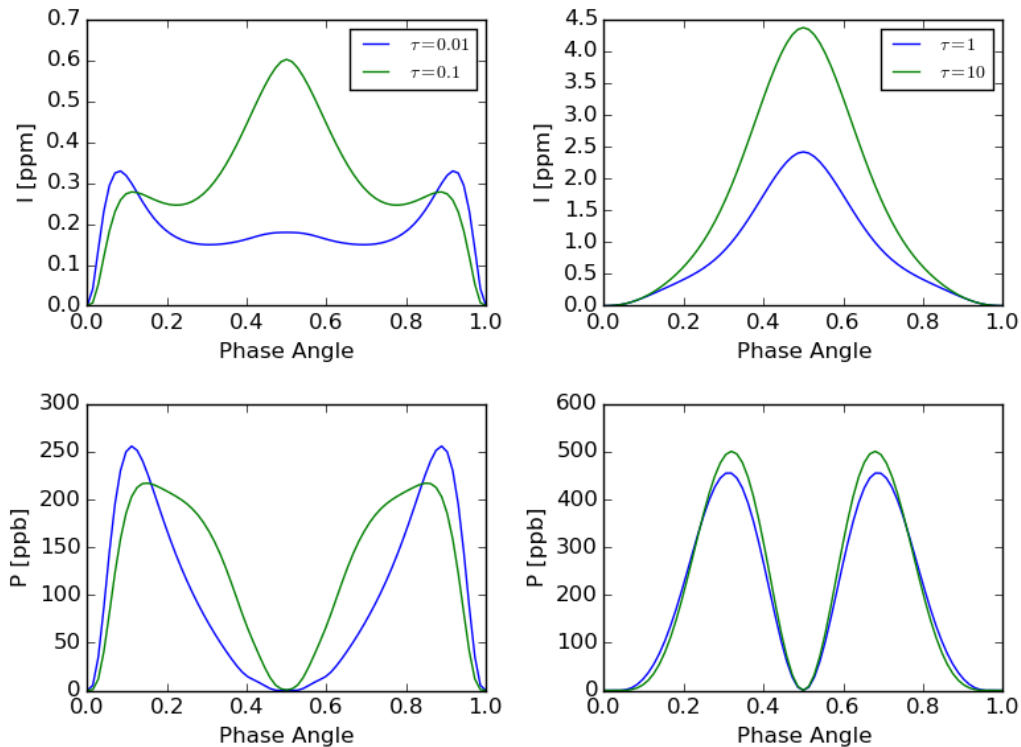


Figure 4.3: Reflected starlight intensity and degree of polarization phase curves for TRAPPIST-1e in the thin (left column) and thick atmospheric (right column) limits over an ocean like glinting surface. Legend indicates the optical depth of the atmosphere. The phase angle used here is an atypical convention chosen for consistency with exoplanetary polarization literature (for e.g., Wiktorowicz et al., 2015). Under this convention, phase angles of 0 and 1 correspond to mid-transit (only nightside is visible) and a phase of 0.5 corresponds to opposition (full dayside is visible). Intensity and polarization are expressed as fractions of direct, unscattered starlight in units of parts per million [ppm] and parts per billion [ppb].

Clouds and hazes introduce their own features into both the intensity and polarization curves. The effects of cloud particle size and global cloud fraction have been discussed in detail in other work (e.g., Zugger et al., 2010; Zugger et al., 2011;

Karalidi, Stam, and Hovenier, 2012). For our purposes, we examine one representative case of water clouds with a size of $2 \mu\text{m}$ and a size variance of $0.1 \mu\text{m}$, which are similar to cloud particle type A in Karalidi, Stam, and Hovenier (2012). Phase curves for TRAPPIST-1e with a planet wide deck of clouds of varying optical depth shown in Fig 4.4. Thick clouds increase planet brightness significantly at opposition, but generally have a lower degree of polarization.

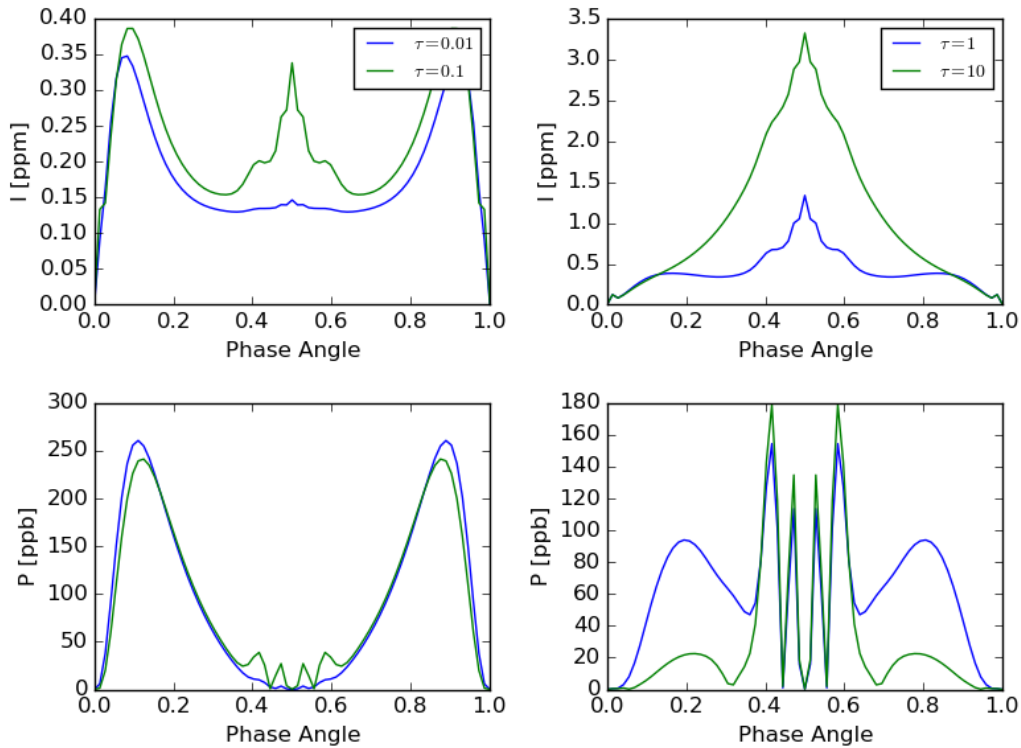


Figure 4.4: Same as Fig 4.3, but with scattering by cloud particles of size $2 \mu\text{m}$. Note the appearance of rainbows around phase 0.4 and 0.6 in the thick cloud limit.

Signatures of Different Ocean Configurations

For further modeling in this section, we will use an atmospheric optical depth of 0.1, a surface Lambertian albedo of 0.2 (for dry surfaces), a weakly absorbing Rayleigh scattering atmosphere (single scattering albedo of 0.9999) and a wind speed of 10 m/s for the Cox-Munk model. A Rayleigh scattering, Earth-like atmosphere with a pressure of 1 bar has an optical depth of 0.1 around 550 nm (Bodhaine et al., 1999) and as seen in Figs 4.3 and 4.4 in the previous section, this optical depth provides a fair mixture of features from both the atmosphere and ocean glint. The previous section only dealt with a uniform, global ocean. However, this is only one

possible configuration. If the planet is tidally locked and near the outside edge of the continuously habitable zone, we may have an open water ocean around the sub stellar point. It should be noted that factors such as the total insolation, thermal mass of the atmosphere, presence of greenhouse gases, and the orbital period can affect the ocean configuration. We model this case by setting an open ocean within 30° of the sub stellar point and dry surfaces elsewhere (eyeball ocean). With a smaller fraction of ocean surface, the difference in the intensity curves is harder to detect. Furthermore, in the case where the planet is tidally locked with a short period or not tidally locked but still quite cold, we could expect to have a planet encircling ocean around the equator. For the case of an equatorial ocean, the polarization is intermediate to the two cases discussed above. We model this case by having an ocean within 30° latitude of the equator. Models for these cases: a global ocean, a wholly dry planet, eyeball ocean and equatorial ocean are shown in Fig 4.5. Planets with oceans are in general darker than the dry planet; however, the eyeball ocean curve coincides with the dry planet curve after quadrature phases (<0.25 or >0.75) when the ocean begins to go out of view.

Phase Curves for the TRAPPIST-1 System

The TRAPPIST-1 system consists of seven planets packed into orbits closer than 0.07 AU around their star. Observations of reflected light curves will likely not be able to spatially separate light coming from different planets. So any data collected will measure the sum of the reflected light coming from all the planets. We investigate the prospects of retrieving a glint signal from such a sum. To convert the brightness and polarization phase curves from the above calculations for TRAPPIST-1e to other planets in the system, they will need to be scaled by a factor of R_p^2/a^2 , where R_p is the radius of the planet and a is the orbital distance from the star. We only model starlight scattering by the planets and do not consider star planet interactions such as transits or eclipses in these phase curves. For convenience, we provide these factors in Table 4.4.

We assume that all planets other than TRAPPIST-1e are dry, and TRAPPIST-1e is an aqua planet. Fig 4.6 shows reflected light curves for this case. The summed intensity and polarization as shown by the thick, black curve is the observable quantity. Note that the contribution of planet e to the sum total in intensity (0.2 ppm out of 15 ppm or $\sim 1\%$) is about one order of magnitude smaller than its contribution to the polarization (0.2 ppm out of 1.2 ppm or $\sim 17\%$). Therefore, observing polarization offers a far larger contrast in this case. Note also that having multiple planets around

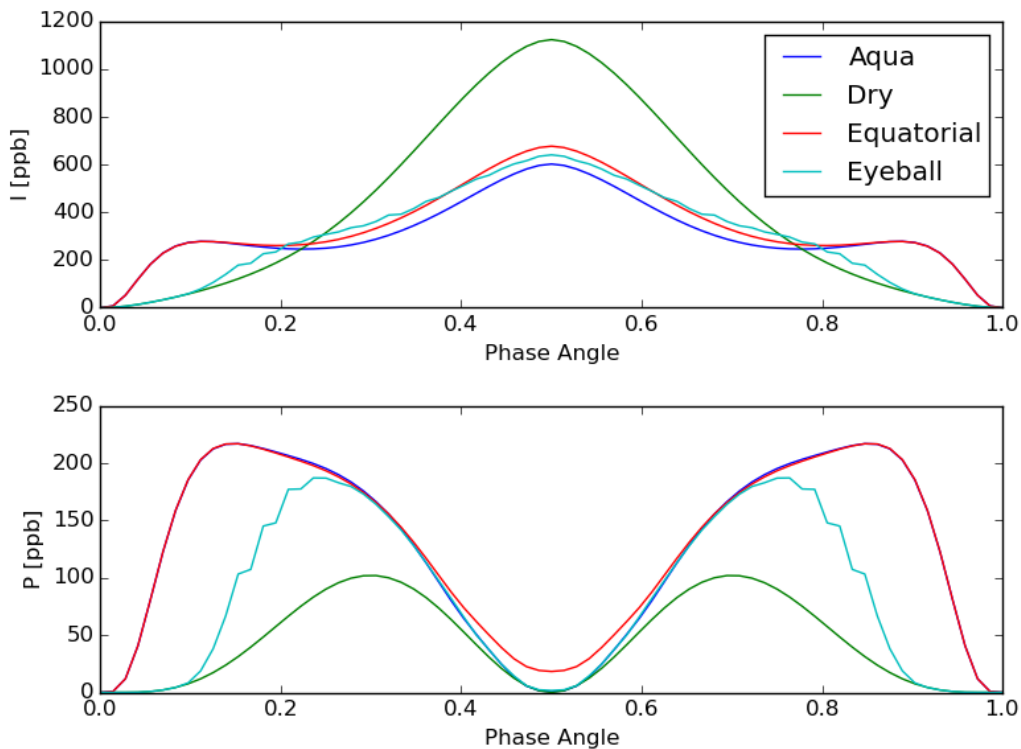


Figure 4.5: Phase curves for fully ocean covered (aqua), completely dry planet and two intermediate cases. The equatorial ocean and global ocean cases have near identical polarization curves since the glint signal comes primarily from near the equator. The intensity curves for the non-dry cases are nearly identical, and different from the dry case, since the dry surfaces are brighter than the ocean at non-glint angles and contribute significantly to disc brightness.

a star increases the degree of polarization of the star-planet system, which might be usable characteristic for surveys. Given this observable quantity, we want to answer the questions: how long an observing period is necessary to obtain a definitive signal in polarized light from this planet? How reliable is this detection under different conditions? To examine this, we consider the combined light curves of the TRAPPIST-1 planets under a few different scenarios:

Case 1: Planet e has a global ocean, other planets are totally dry. All planets have a clear atmosphere with an optical depth of 0.1 (same as Fig 4.6).

Case 2: Same as Case 1, except planet e has a clear atmosphere with optical depth of 1. Note that the polarization signal from planet e is now dominated by atmospheric Rayleigh scattering instead of ocean glint.

Case 3: All planets have a cloudy atmosphere with an optical depth of 0.1. The

Planet	Radius (R_p)	Orbit (AU)	Scaling Factor
TRAPPIST-1b	1.09	0.011	9.00
TRAPPIST-1c	1.06	0.015	4.54
TRAPPIST-1d	0.77	0.021	1.22
TRAPPIST-1e	0.92	0.028	1.0
TRAPPIST-1f	1.04	0.037	0.75
TRAPPIST-1g	1.13	0.045	0.59
TRAPPIST-1h	0.72	0.060	0.13

Table 4.1: Scaling factors for brightness to convert above curves to other planets in the system based on relative size and orbital distance. Values taken from Wang et al. (2017).

ocean on planet e is visible, but slightly obscured by cloud.

Case 4: All planets have a cloudy atmosphere with an optical depth of 1, i.e, the surface is invisible on all planets.

We compute the Fourier transform of the sum total intensity and polarization curves for different observing periods for each of these cases (Fig 4.7). Large amplitude variations of less than 1.5 days (shortest known planetary period) are smoothed to 0. For observing periods of order 200 days and above, a peak corresponding to the period of planet e is distinguishable by eye from the power spectrum.

For cases 1 and 3, where the glint signal is most unambiguous, the Fourier transform shows a clear signal for planet e that is about a factor of 10 stronger in polarization than in intensity. For case 2, where the thick atmosphere gives planet e a much higher albedo, the detection is stronger than in any other case. Conversely, if the atmosphere of planet e had absorbers that lowered its albedo, both intensity and polarization will give a much weaker signal. However, polarization and intensity signals are about the same magnitude and polarization offers no advantage for observing. In case 4, the thick cloud deck makes all the planets look uniform. The strength of the observable signal monotonically decreases with distance from the star, and polarization again offers no real advantage over intensity alone. Additionally TRAPPIST-1 is an active star (Roettenbacher and Kane, 2017) with a noisy stellar spectrum which contaminates planetary spectra (Zhang et al., 2018). Polarization offers great advantages for glint detection under certain conditions, but variability in planetary properties and stellar noise or instrumental polarization (e.g., Wiktorowicz et al., 2015) can limit how useful the technique can be.

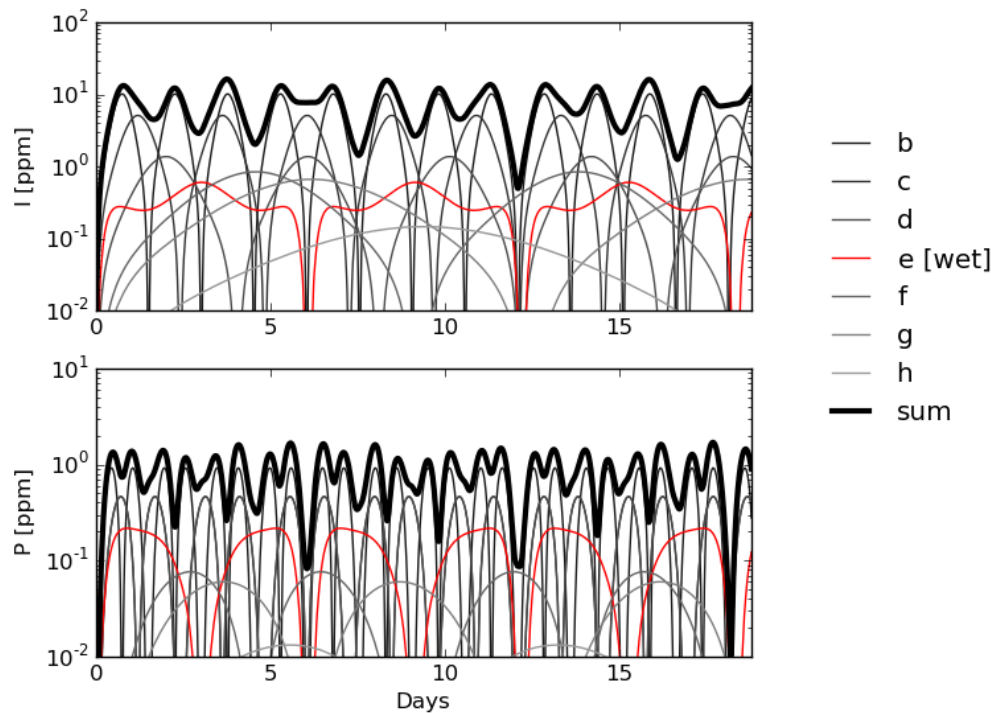


Figure 4.6: Reflected light intensity and polarization expressed as a fraction of direct starlight for the TRAPPIST-1 system for one period of the outermost planet (~ 19 days). Planet e is modeled as an aquaplanet, while the other planets are completely dry. The wet planet signal contributes a much higher fraction of the sum total in polarization ($\sim 17\%$) than in intensity ($\sim 1\%$).

Observing Possibilities

For the case of TRAPPIST-1, the dimness of the star, the small size of the planet and the presence of several other planets in the system make it extremely challenging to observe phase curves associated with surface reflectance without committing several thousand hours of observing time from the largest ground based telescopes. This is in spite of the polarized glint signal offering a 10x better contrast than a simple intensity phase curve. Present day ground and space telescopes cannot reach this high contrast at small angular separations from the star (Mawet et al., 2012; Robinson, Stapelfeldt, and Marley, 2016). For the moment, the way to indirectly infer the presence of an ocean on one of the TRAPPIST-1 planets will be the detection of water absorption in the planetary atmosphere during transit along with some measurement or estimate of surface temperature.

In the near future, there are proposals for several large space and ground based

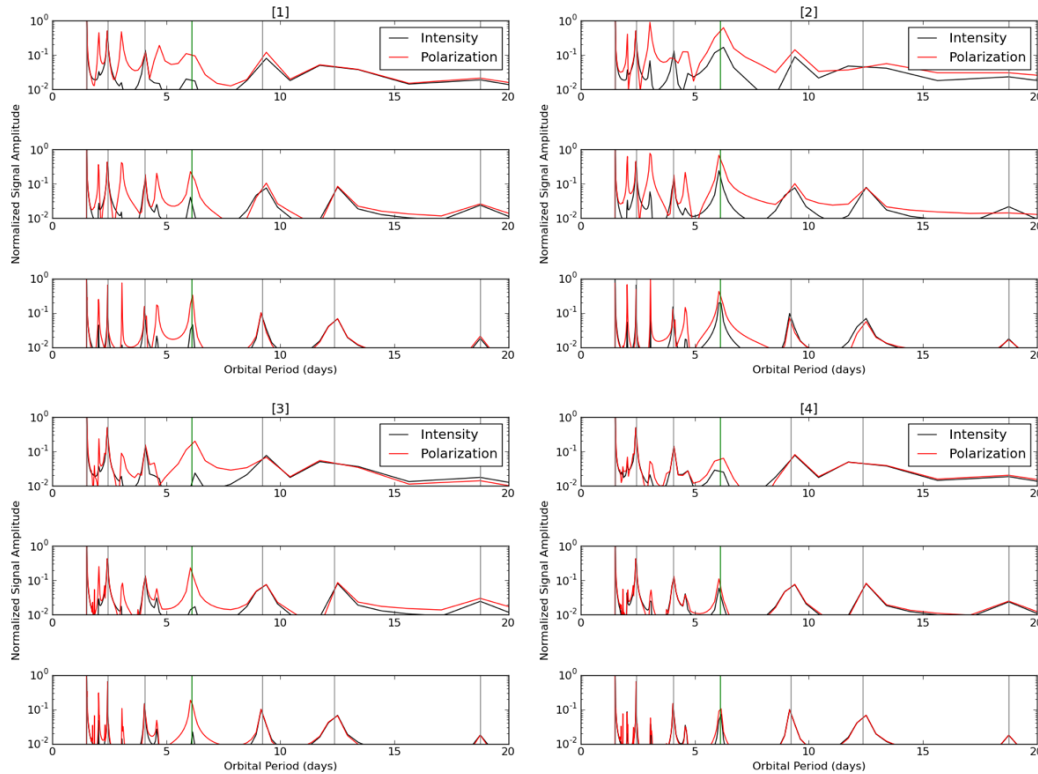


Figure 4.7: Fourier transforms of the combined phase curves (dark black line in Fig 4.6) for observing periods totaling 5, 10 and 20 periods of the outermost planet (~ 94 , 188 and 375 days) for cases 1-4 described in the text. Vertical lines indicate the periods of the known planets, TRAPPIST-1e is in green.

telescopes with coronagraphs (and polarimeters), which make them sensitive to very low planet star contrasts. Here we explore the parameter space of where ocean planets might exist and what instruments might be able to observe their glint signals (Fig 4.8). We scale our aquaplanet modeling results for TRAPPIST-1e to Earth sized planets at different orbital distances around stars of various luminosities. Since the degree of polarization is close to 100%, the glint polarization and intensity contrasts with respect to the star are the same.

WFIRST-AFTA (Spergel et al., 2015) is a 2.4 m space telescope with a coronagraph (and possibly a polarimeter) and is expected to reach sensitivities of 0.1 ppb (1/10000 ppm) in the visible/near infrared. However, the coronagraph has an inner working angle (IWA) of 100 mas (milli arc seconds), which rules out the habitable zones of cool stars, but might allow for observing glint on planets around Sun-like stars. JWST NIRCcam cannot observe such signals even though it has an IWA of ~ 10 mas for certain configurations, the detection contrasts required are in the range of

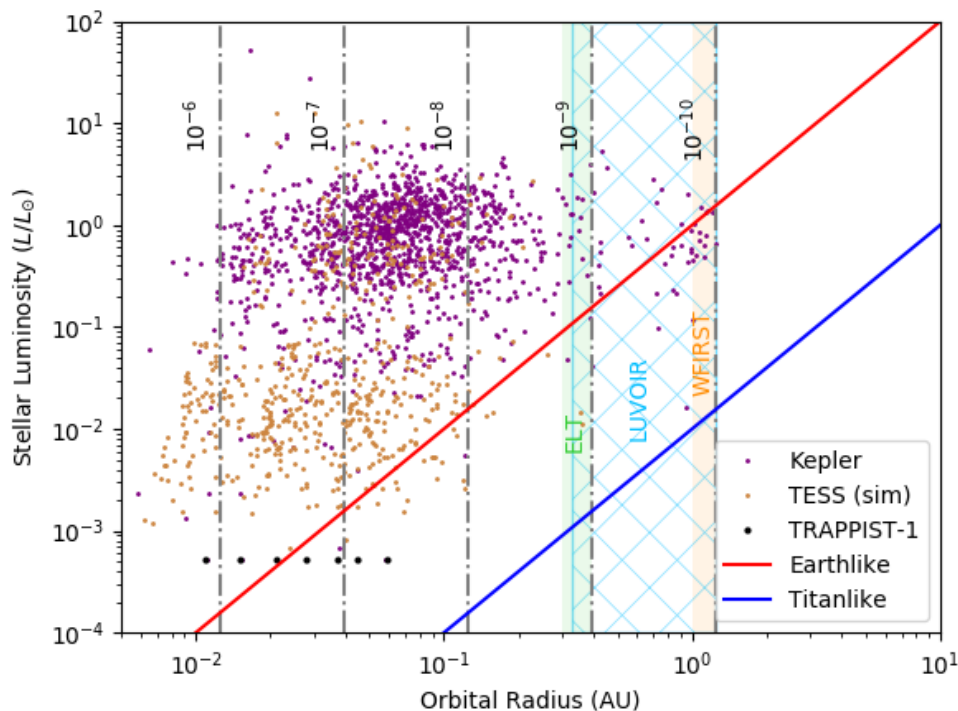


Figure 4.8: Modeled glint star-planet contrast signals (dot-dash grey lines) plotted against detection limits of various upcoming large telescopes (WFIRST, LUVOIR and ELT) for systems at a distance of 10 pc. The blue and red lines indicate the distance from the star at which a planet receives an Earthlike (surface water ocean) and Titanlike (surface hydrocarbon lakes) solar flux. Present or near future observable Earth like planets (size smaller than $2R_{Earth}$) from Kepler detections and candidate objects (downloaded from exoplanets.org (Han et al., 2014) on 6 Oct 2017) and simulated detections from TESS (Sullivan et al., 2015) are overplotted for a sense of the number of detections by surveys that may have an ocean, which can be followed up for glint studies. Planetary periods listed in the TESS simulated dataset are converted to orbital distances by converting the listed stellar radii to stellar masses using the method of Demircan and Kahraman, 1991.

10^{-4} (Krist et al., 2010; Beichman et al., 2010). The most promising space telescope concept for these observations is LUVOIR (Bolcar et al., 2015). With a proposed telescope mirror of about 18 m, this telescope is planned to be sensitive to 10^{-10} contrast at 35 mas.

Among ground based telescopes, the EPICS exoplanet imager for the 40m ELT (Kasper et al., 2010) aims to achieve a contrast of 10^{-8} at 30 mas and 10^{-9} at 100 mas in the NIR, which might allow a few detections. The LMIRCam on the Large

Binocular Telescope (Defrere et al., 2014) can also see this range, but only reaches a contrast of 10^{-5} for the region of interest.

4.5 Conclusions

We model scattering of starlight by the atmosphere and surface of TRAPPIST-1e to produce a number of polarized phase curves for different distributions of the surface ocean and atmospheric cloud opacities. We find that the existence of a sizeable liquid water surface will show a strong signal in polarized light if the atmosphere is not opaque, and this measurement might offer a definitive difference between liquid water holding and dry planets. However, for the case of TRAPPIST-1, direct observation of glint polarization is impossible with current instruments. Future missions, such as WFIRST-AFTA, LUVOIR or ELT may be capable of making such a measurement for Earth-like planets around Sun-like stars. The presence of polarimeters on such telescopes could allow for definitive detections of oceans on Earth-like exoplanets.

4.6 Acknowledgements

We thank Peter Gao for insightful comments and Sloane Wiktorowicz for giving us an observer’s perspective on the model results. This research was supported in part by an NAI Virtual Planetary Laboratory grant from the University of Washington to the Jet Propulsion Laboratory and California Institute of Technology, and in part by the Jet Propulsion Laboratory. We acknowledge use of the Exoplanet Orbit Database and the Exoplanet Data Explorer at exoplanets.org

References

- Alberti, Tommaso, Vincenzo Carbone, Fabio Lepreti, and Antonio Vecchio (2017). “Comparative Climates of the Trappist-1 Planetary System: Results from a Simple Climate-vegetation Model”. In: *The Astrophysical Journal* 844.19, 7pp.
- Bacour, Cédric and François-Marie Bréon (2005). “Variability of biome reflectance directional signatures as seen by POLDER”. In: *Remote Sensing of Environment* 98.1, pp. 80–95.
- Beichman, Charles A et al. (2010). “Imaging young giant planets from ground and space”. In: *Publications of the Astronomical Society of the Pacific* 122.888, p. 162.
- Bicheron, Patrice and Marc Leroy (2000). “Bidirectional reflectance distribution function signatures of major biomes observed from space”. In: *Journal of Geophysical Research: Atmospheres* 105.D21, pp. 26669–26681.

- Bodhaine, Barry A, Norman B Wood, Ellsworth G Dutton, and James R Slusser (1999). “On Rayleigh optical depth calculations”. In: *Journal of Atmospheric and Oceanic Technology* 16.11, pp. 1854–1861.
- Bolcar, Matthew R et al. (2015). “Technology development for the advanced technology large aperture space telescope (ATLAST) as a candidate large UV-optical-infrared (LUVOIR) surveyor”. In:
- Bourrier, V et al. (2017). “Temporal Evolution of the High-energy Irradiation and Water Content of TRAPPIST-1 Exoplanets”. In: *Astronomical Journal* 154.3, Art–No.
- Cowan, Nicolas B et al. (2009). “Alien maps of an ocean-bearing world”. In: *The Astrophysical Journal* 700.2, p. 915.
- Cowan, Nicolas B, Dorian S Abbot, and Aiko Voigt (2012). “A false positive for ocean glint on exoplanets: The latitude-albedo effect”. In: *The Astrophysical Journal Letters* 752.1, p. L3.
- Cox, Charles and Walter Munk (1954). “Measurement of the roughness of the sea surface from photographs of the sun’s glitter”. In: *JOSA* 44.11, pp. 838–850.
- Defrere, Denis et al. (2014). “L-band AGPM vector vortex coronagraph’s first light on LBTI/LMIRCam”. In: *SPIE Astronomical Telescopes+ Instrumentation*. International Society for Optics and Photonics, pp. 91483X–91483X.
- Demircan, Osman and Göksel Kahraman (1991). “Stellar mass-luminosity and mass-radius relations”. In: *Astrophysics and Space Science* 181.2, pp. 313–322.
- Dumont, Marie, Olivier Brissaud, Ghislain Picard, Bernard Schmitt, J-C Gallet, and Yves Arnaud (2010). “High-accuracy measurements of snow Bidirectional Reflectance Distribution Function at visible and NIR wavelengths—comparison with modelling results”. In: *Atmospheric Chemistry and Physics* 10.5, pp. 2507–2520.
- Fast, Jerome D, William I Gustafson, Richard C Easter, Rahul A Zaveri, James C Barnard, Elaine G Chapman, Georg A Grell, and Steven E Peckham (2006). “Evolution of ozone, particulates, and aerosol direct radiative forcing in the vicinity of Houston using a fully coupled meteorology-chemistry-aerosol model”. In: *Journal of Geophysical Research: Atmospheres* 111.D21.
- Gillon, Michaël et al. (2017). “Seven temperate terrestrial planets around the nearby ultracool dwarf star TRAPPIST-1”. In: *Nature* 542.7642, pp. 456–460.
- Grell, Georg A, Steven E Peckham, Rainer Schmitz, Stuart A McKeen, Gregory Frost, William C Skamarock, and Brian Eder (2005). “Fully coupled “on-line” chemistry within the WRF model”. In: *Atmospheric Environment* 39.37, pp. 6957–6975.

- Han, Eunkyu, Sharon X Wang, Jason T Wright, Y Katherina Feng, Ming Zhao, Onsi Fakhouri, Jacob I Brown, and Colin Hancock (2014). “Exoplanet orbit database. II. Updates to exoplanets. org”. In: *Publications of the Astronomical Society of the Pacific* 126.943, p. 827.
- Horak, Henry G (1950). “Diffuse Reflection by Planetary Atmospheres.” In: *The Astrophysical Journal* 112, p. 445.
- Karalidi, T, DM Stam, and JW Hovenier (2012). “Looking for the rainbow on exoplanets covered by liquid and icy water clouds”. In: *Astronomy & Astrophysics* 548, A90.
- Kasper, Markus et al. (2010). “EPICS: direct imaging of exoplanets with the E-ELT”. In: *Ground-based and Airborne Instrumentation for Astronomy III*. Vol. 7735. International Society for Optics and Photonics, 77352E.
- Kopparla, Pushkar, Vijay Natraj, Xi Zhang, Mark R Swain, Sloane J Wiktorowicz, and Yuk L Yung (2016). “A Multiple Scattering Polarized Radiative Transfer Model: Application to HD 189733b”. In: *The Astrophysical Journal* 817.1, p. 32.
- Krist, John E et al. (2010). “The JWST/NIRCam coronagraph flight occulter”. In: Lingam, Manasvi and Abraham Loeb (2017). “Enhanced interplanetary panspermia in the TRAPPIST-1 system”. In: *Proceedings of the National Academy of Sciences*, p. 201703517.
- Luger, Rodrigo et al. (2017). “A seven-planet resonant chain in TRAPPIST-1”. In: *Nature Astronomy* 1.
- Mawet, Dimitri et al. (2012). “Review of small-angle coronagraphic techniques in the wake of ground-based second-generation adaptive optics systems”. In: *SPIE Astronomical Telescopes+ Instrumentation*. International Society for Optics and Photonics, pp. 844204–844204.
- Meadows, Victoria S et al. (2017). “Exoplanet Biosignatures: Understanding Oxygen as a Biosignature in the Context of Its Environment”. In: *arXiv preprint arXiv:1705.07560*.
- O’Malley-James, Jack T and L Kaltenegger (2017). “UV surface habitability of the TRAPPIST-1 system”. In: *Monthly Notices of the Royal Astronomical Society: Letters* 469.1, pp. L26–L30.
- Peckham, SE et al. (2011). *WRF/Chem Version 3.3 User’s Guide*, 94 p.
- Robinson, Tyler D, Victoria S Meadows, and David Crisp (2010). “Detecting oceans on extrasolar planets using the glint effect”. In: *The Astrophysical Journal Letters* 721.1, p. L67.
- Robinson, Tyler D, Karl R Stapelfeldt, and Mark S Marley (2016). “Characterizing rocky and gaseous exoplanets with 2 m class space-based coronagraphs”. In: *Publications of the Astronomical Society of the Pacific* 128.960, p. 025003.

- Roettenbacher, Rachael M and Stephen R Kane (2017). “The Stellar Activity of TRAPPIST-1 and Consequences for the Planetary Atmospheres”. In: *The Astrophysical Journal* 851.2, p. 77.
- Spergel, D et al. (2015). “Wide-Field Infrared survey telescope-astrophysics focused telescope assets WFIRST-AFTA 2015 report”. In: *arXiv preprint arXiv:1503.03757*.
- Spurr, Robert JD (2006). “VLIDORT: A linearized pseudo-spherical vector discrete ordinate radiative transfer code for forward model and retrieval studies in multilayer multiple scattering media”. In: *Journal of Quantitative Spectroscopy and Radiative Transfer* 102.2, pp. 316–342.
- Stam, DM (2008). “Spectropolarimetric signatures of Earth-like extrasolar planets”. In: *Astronomy & Astrophysics* 482.3, pp. 989–1007.
- Sullivan, Peter W et al. (2015). “The Transiting Exoplanet Survey Satellite: Simulations of planet detections and astrophysical false positives”. In: *The Astrophysical Journal* 809.1, p. 77.
- Wang, Songhu, Dong-Hong Wu, Thomas Barclay, and Gregory P Laughlin (2017). “Updated Masses for the TRAPPIST-1 Planets”. In: *arXiv preprint arXiv:1704.04290*.
- Wang, Yujie, Alexei I Lyapustin, Jeffrey L Privette, Robert B Cook, Suresh K SanthanaVannan, Eric F Vermote, and Crystal L Schaaf (2010). “Assessment of biases in MODIS surface reflectance due to Lambertian approximation”. In: *Remote Sensing of Environment* 114.11, pp. 2791–2801.
- Wiktorowicz, Sloane J, Larissa A Nofi, Daniel Jontof-Hutter, Pushkar Kopparla, Gregory P Laughlin, Ninos Hermis, Yuk L Yung, and Mark R Swain (2015). “A ground-based Albedo Upper Limit for HD 189733b from Polarimetry”. In: *The Astrophysical Journal* 813.1, p. 48.
- Wolf, Eric T (2017). “Assessing the Habitability of the TRAPPIST-1 System Using a 3D Climate Model”. In: *The Astrophysical Journal Letters* 839.1, p. L1.
- Zhang, Zhanbo, Yifan Zhou, Ben Rackham, and Daniel Apai (2018). “The Near-Infrared Transmission Spectra of TRAPPIST-1 Planets b, c, d, e, f, and g and Stellar Contamination in Multi-Epoch Transit Spectra”. In: *arXiv preprint arXiv:1802.02086*.
- Zugger, ME, JF Kasting, DM Williams, TJ Kane, and CR Philbrick (2011). “Searching for water Earths in the near-infrared”. In: *The Astrophysical Journal* 739.1, p. 12.
- Zugger, Michael E, James F Kasting, Darren M Williams, Timothy J Kane, and C Russell Philbrick (2010). “Light scattering from exoplanet oceans and atmospheres”. In: *The Astrophysical Journal* 723.2, p. 1168.

*Chapter 5***A FAST AND ACCURATE PCA BASED RADIATIVE TRANSFER MODEL: EXTENSION TO THE BROADBAND SHORTWAVE REGION AND IMPROVEMENTS TO AEROSOL SCHEME, VERTICAL LAYERING AND SPECTRAL BINNING**

This chapter is adapted from work previously published as

Kopparla, Pushkar, Vijay Natraj, Drew Limpasuvan, Robert Spurr, David Crisp, Run-Lie Shia, Peter Somkuti, and Yuk L Yung (2017). “PCA-based radiative transfer: Improvements to aerosol scheme, vertical layering and spectral binning”. In: *Journal of Quantitative Spectroscopy and Radiative Transfer* 198, pp. 104–111.

Kopparla, Pushkar, Vijay Natraj, Robert Spurr, Run-Lie Shia, David Crisp, and Yuk L Yung (2016). “A fast and accurate PCA based radiative transfer model: Extension to the broadband shortwave region”. In: *Journal of Quantitative Spectroscopy and Radiative Transfer* 173, pp. 65–71.

5.1 Abstract

Accurate radiative transfer (RT) calculations are necessary for many earth-atmosphere applications, from remote sensing retrieval to climate modeling. A Principal Component Analysis (PCA)-based spectral binning method has been shown to provide an order of magnitude increase in computational speed while maintaining an overall accuracy of 0.01% (compared to line-by-line calculations) over narrow spectral bands. In this paper, we have extended the PCA method for RT calculations over the entire shortwave region of the spectrum from 0.3 to 3 microns. The region is divided into 33 spectral fields covering all major gas absorption regimes. We find that the RT performance runtimes are shorter by factors between 10-100 as compared to a standard line by line RT model. We describe several improvements made to the method and provide a discussion of the method’s performance over a diverse set of atmospheric profiles and land surface types. The method is now capable of providing atmospheric spectra with residuals under 0.1%, calculated with respect to the continuum, throughout the shortwave region between 0.3 – 3 μm at high resolution, which is substantial improvement over errors reported in earlier work. Future directions for applications and further optimization are examined.

5.2 Introduction

There have been many approaches to enhance the performance of radiative transfer (RT) computations at infrared wavelengths, where vibration-rotation bands of gases introduce rapid variations in the gas absorption cross sections, the most widely used being the correlated-k model (Goody et al., 1989; Lacis and Oinas, 1991; Fu and Liou, 1992). Other approaches include spectral mapping (Crisp, 1997; Moncet et al., 2008), low-stream interpolations (Duan, Min, and Li, 2005; O'Dell, 2010) and low orders of scattering approximations (Natraj and Spurr, 2007).

The Principal Component Analysis (PCA) technique for RT speed enhancement was first proposed by Natraj et al. (Natraj et al., 2005) (and later independently by Liu et al. (Liu et al., 2006)), who reproduced the TOA reflectance spectrum over a small spectral region centered on the O_2 A band at $0.75\mu m$ to accuracies of 0.3% compared to a line-by-line RT model, while achieving a 10-fold increase in speed. Further development of the PCA model, its expansion to broader spectral regions and the derivation of analytic Jacobians can be found in a series of papers (Natraj, Shia, and Yung, 2010; Spurr et al., 2013).

The PCA-based RT technique takes advantage of redundancy in the optical property information (gas absorption, Rayleigh scattering and aerosol scattering profiles) to reduce computational time without significant decrease in accuracy. The basic principle here is that fast two-stream calculations, when compared against more exact, multi-stream calculations, have errors that are non-random and strongly correlated with the optical properties of the atmosphere. The method therefore uses principal components (PCs) derived from the optical properties to generate correction factors which greatly reduce the magnitude of errors from the two-stream model. However, the effectiveness of the correction factors is sensitive to a variety of parameters: the binning scheme used to group monochromatic grid points together for the PCA, the number of principal components used to calculate the correction factors, the vertical grid on which calculations are carried out and so on. The purpose of this paper is to explore these dependencies and optimize strategies for choosing model parameters with the goal of achieving the required accuracy with the shortest possible model runtime.

This chapter is organized as follows. In Section 2 we recapitulate the PCA-RT method and describe new developments, including a better aerosol scheme, vertical grid structures and binning considerations. In Section 3, we present runtime and error statistics for top-of-the-atmosphere (TOA) radiance calculations, and discuss

implications.

5.3 The PCA RT Technique

RT Models

The PCA RT technique is based on two contrasting RT models. First, for accurate MS calculations we use the LIDORT discrete ordinate RT model (Spurr, 2008) – which includes the treatment of solar-beam incoming attenuation in a spherically curved atmosphere (the pseudo-spherical approximation), and the use of the delta-M scaling approximation for aerosol scattering with sharply peaked forward scattering. We run LIDORT in MS mode with 32 streams (computational quadrature angles; 16 each for upwelling and downwelling polar directions); the single scatter (SS) contribution is not included in the calculations. A full set of LIDORT MS calculations at every wavelength point is computationally expensive; the key to the PCA RT approach is to drastically limit the number of such full-MS calculations to a reduced set of PCA-determined optical profiles that capture the vast majority of optical information for a given wavelength range.

Secondly, fast RT computations are done using a numerically efficient two-stream-exact single scattering (2S-ESS) RT model (Spurr and Natraj, 2011), which comprises two parts. The 2S part is a fast MS calculation based on a single discrete ordinate in each of the up-welling and down-welling directions; the RT calculation is done analytically except for the multi-layer boundary-value problem (which is also solved using a simple and fast pentadiagonal solver rather than typical matrix inversion techniques). The 2S calculation also uses the pseudo-spherical approximation. The ESS part is an accurate spherical-geometry calculation of the singly scattered radiation computed with the complete scattering phase function (not a truncated form based on a limited number of Legendre polynomial expansion coefficients). The 2S-ESS combination is the “fast” RT calculation; in this, the use of the ESS calculation mitigates bias due to the severe phase function truncation inherent in the 2S approximation to MS. The LIDORT-ESS combination provides the most accurate computation of the complete (SS+MS) radiation field; in the following, we will refer to this benchmark computation as the "Exact RT" calculation, against which the accuracy of the PCA RT model is to be compared. A more detailed summary of these models can be found in Spurr et al. (2017) (Spurr et al., 2017).

PCA RT Formalism

We refer the reader to earlier publications (Natraj et al., 2005; Natraj, Shia, and Yung, 2010; Spurr et al., 2013; Kopparla et al., 2016; Spurr et al., 2017) for details about the PCA RT technique. Here, we report on recent developments and modifications. The first step is to derive the atmospheric optical properties on a quasi-monochromatic spectral grid, that fully resolves variations in the spectral structure of the gas absorption and aerosol extinction. The next step is to partition the given spectral range into a number of appropriately chosen bins, each bin containing spectral points for which the optical properties are broadly "similar". column-integrated gas absorption optical depth; we discuss the criteria in subsection 2.3. Each bin, which contains a subset of the monochromatic grid points within the spectral range, is then subjected to an independent PCA procedure as described below.

Consider a bin with N monochromatic grid points in an atmosphere stratified into M optically homogeneous layers. Let $\tau_{i,j}$ be the total gas absorption optical depth in layer i at monochromatic grid point j and $\omega_{i,j}$ be the Rayleigh scattering optical depth. We then take the logarithm of the optical properties on this grid and subtract the mean value and then create a covariance matrix. Let us denote this set of log optical properties by $F_{k,j}$, where $F_{[1,M],j}$ are the gas absorption optical depths and $F_{[M+1,2M],j}$ are the Rayleigh scattering optical depths. The mean-removed covariance matrix C over all layers has elements given by (k and l are layer indices)

$$C_{k,l} = \overline{(F_{k,j} - \bar{F}_k) (F_{l,j} - \bar{F}_l)} \quad (5.1)$$

where the overbar denotes a mean-value over all grid points in the bin. The index l also goes from 1 to $2M$. If necessary, surface albedo and aerosol properties (described in Section 2.4) can also be added into this grid. These are particularly important for calculations over broad spectral regions, where these properties can vary significantly from one end of the spectral region to the other. For example, if 3 more optical properties corresponding to the surface albedo and aerosols were included, the size of the covariance matrix goes from $[2M, N]$ to $[2M + 3, N]$. The rest of the procedure is identical. The eigenvectors of the covariance matrix are the empirical orthogonal functions (EOFs). The PCs are calculated by projecting the optical properties on to the EOFs. Each EOF has $2M$ components; they are scaled by the square root of the variance to make them dimensionally consistent with the corresponding optical properties. Thus, we can express all the original information in our new coordinate system as

$$\ln \tau_{k,j} = \ln \bar{\tau}_k + \sum_{i=1}^M P_{i,j} \epsilon_{i,k} \quad (5.2)$$

$$\ln \omega_{k,j} = \ln \bar{\omega}_k + \sum_{i=M+1}^{2M} P_{i,j} \epsilon_{i,k} \quad (5.3)$$

where the overbar indicates a mean value over all grid points in the bin, k is the layer index and j is an index that shows the position of the grid point within the bin. $P_{i,j}$ and $\epsilon_{i,k}$ are the i^{th} PC and EOF respectively. Spectral information is stored in the PCs, while the vertical profile information is stored in the EOFs. In essence, by choosing monochromatic grid points with closely related optical properties such as column-integrated optical depths, it is possible to capture most of the relevant variation in optical properties with a small number of EOFs, usually four or less. Thus, starting with a dataset of dimension $2M \times N$, we have reduced it to a total of $4 \times N$ (PCs) and $4 \times T \times 2M$ (for 4 EOFs and T bins across the spectral region). In effect, the variation in the two-stream model errors trace the variation in the optical properties. With PCA combining most of the variation in the optical properties into a small number of EOFs, we can calculate the error (defined as the difference between the 2S and "exact" model radiance or flux) at any one monochromatic grid point, and use the PCs to estimate the errors at all other grid points in that bin.

First, we calculate the MS radiances for the mean (over all monochromatic grid points) optical property profiles with a multi-stream LIDORT calculation followed by the two-stream calculation. Let us define a quantity I_d

$$I_d = \ln(I_{MS}/I_{2S}) \quad (5.4)$$

The mean optical properties are then perturbed by the magnitude of one scaled EOF in both the positive and negative directions away from the mean for every EOF being used. For instance in layer k , a perturbation corresponding to the i th EOF has the optical depths

$$\ln \tau_k^+ = \ln \bar{\tau}_k + \epsilon_{i,k} \quad (5.5)$$

$$\ln \tau_k^- = \ln \bar{\tau}_k - \epsilon_{i,k} \quad (5.6)$$

The two MS RT models are run again with these perturbed profiles. Let the new logarithmic ratios be I_d^+ and I_d^- . With respect to this EOF, the first and second order differences are calculated as

$$\delta I_k = \frac{I_d^+ - I_d^-}{2} \quad (5.7)$$

$$\delta^2 I_k = I_d^+ + I_d^- - 2I_d \quad (5.8)$$

The corrected 2S radiance is thus calculated as

$$I_l = I_l^{2S} \exp \left[I_d + \sum_{k=1}^4 \delta I_k P_{k,l} + \frac{1}{2} \sum_{k=1}^4 \delta^2 I_k P_{k,l}^2 \right] \quad (5.9)$$

where l is the monochromatic grid point index.

Model Setup and Preliminary Binning Considerations

Wavenumbers in each bin must be chosen such that the optical properties are strongly correlated. This is necessary to reduce the number of EOFs required to attain a given accuracy. If the wavenumbers have optical properties that are very different from each other, we can still capture the variability with a larger number of EOFs, but this has a higher computational cost and defeats the purpose of using PCA.

The entire shortwave region from $0.29 - 3\mu m$ is first divided into 33 spectral "fields" depending on dominant gas absorptions within the field (Table 5.1). Over each field, wavenumbers are grouped into four bins, based on the total column optical depth. We started with the following four bins: $(0 - 0.01)$, $(0.01 - 0.1)$, $(0.1 - 1.0)$ and $(1.0 - \infty)$. Each of these bins is further bisected by dividing wavenumbers along the median single scattering albedo. Finally, the result is a set of eight wavenumber bins which have the same absorbers, and somewhat similar total optical depths. The PCA RT model, as described in the Sections 2.1 and 2.2, is applied to each spectral field with these initial bins, and the residuals are computed with respect to "Exact Model" using 32-stream LIDORT. Next, bins with large residuals are again bisected with respect to total column optical depth; for instance, the second bin would be split into $(0.01 - 0.05)$ and $(0.05 - 0.1)$. This process is repeated until the root mean square residuals are below 0.01% for every spectral field after degrading to typical instrument resolutions (more discussion on this in the results section). We find that, following this procedure, a total of eleven bins provide satisfactory residuals. The upper limits of these bins are $(0.01, 0.025, 0.05, 0.1, 0.25, 0.5, 0.625, 0.75, 1.0, 5.0, \infty)$. The runtime of the code scales linearly with the number of bins. Note from Table 5.1 that the number of wavelengths and the spectral resolution vary according to spectral field — finer absorption features require higher resolution. This was further tested for a wide range

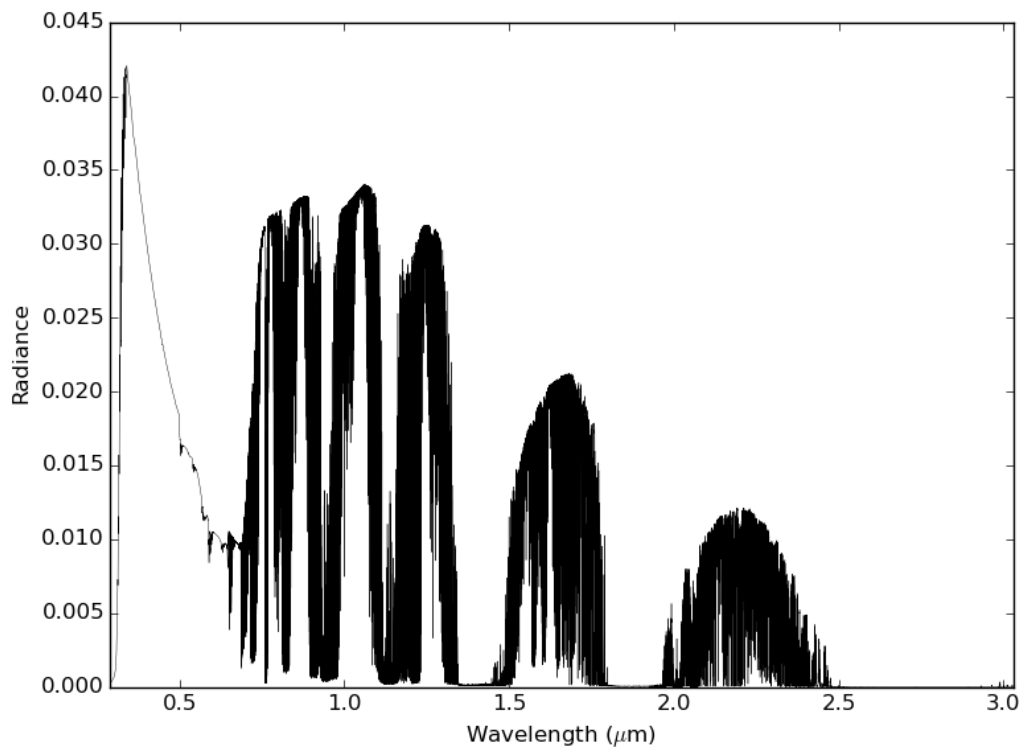


Figure 5.1: Top of the Atmosphere (TOA) reflectances from Exact-RT LIDORT for a single profile showing major absorptions. There are 33 spectral fields in all, with 8 in the ultraviolet/visible and the rest in the shortwave infrared (Table 5.1).

of atmospheric profiles taken from GEOS-CHEM, global 3-D chemical transport model (Bey et al., 2001). We used profiles representing locations in North America chosen over a wide range of latitudes and longitudes. The patterns in error residuals were found to be similar for these profile data sets. We also find that some degree of iteration was necessary in order to determine an acceptable binning scheme for a given spectral range. Although the binning selection is done manually at present, it will be advantageous to automate this procedure. This will allow for customizing and minimizing the number of bins over different spectral ranges for better efficiency.

5.4 Preliminary Results

We compare radiances and performance run-times for the fast-PCA and exact-LIDORT models across all shortwave spectral fields. The 11-bin scheme with four EOFs is used. Figure 5.1 shows the top of the atmosphere radiances calculated using the Exact Model for a single atmospheric profile from the North America GEOS-CHEM profile set. Figures 5.2 and 5.3 show the residuals and radiances

comparing the "Exact" and "fast-PCA" models, and 2-stream and PCA models respectively. In addition, we also compare residuals and timing for the full LIDORT calculations in which the number of streams is reduced from 32 down to as low as 4. The original resolution of the RT calculations is of the order 0.05cm^{-1} ; we use a Gaussian smoothing procedure to reduce the spectral resolution to 0.2cm^{-1} , which is a reasonable value for modern instruments such as OCO-2. As expected, increasing the number of streams improves agreement with the Exact Model. Note particularly that the run-time of the Exact-RT LIDORT model scales as the cube of the number of computational streams, increasing about two orders of magnitude when moving from 4 to 32 streams. However, the PCA model shows only about a 20% increase in run-time over the same range of streams. Thus, when we have scattering aerosols and/or clouds with strongly forward-peaked phase functions that require many streams in the RT, the PCA technique offers a cost-effective way to obtain acceptably accurate results in a reasonable amount of time.

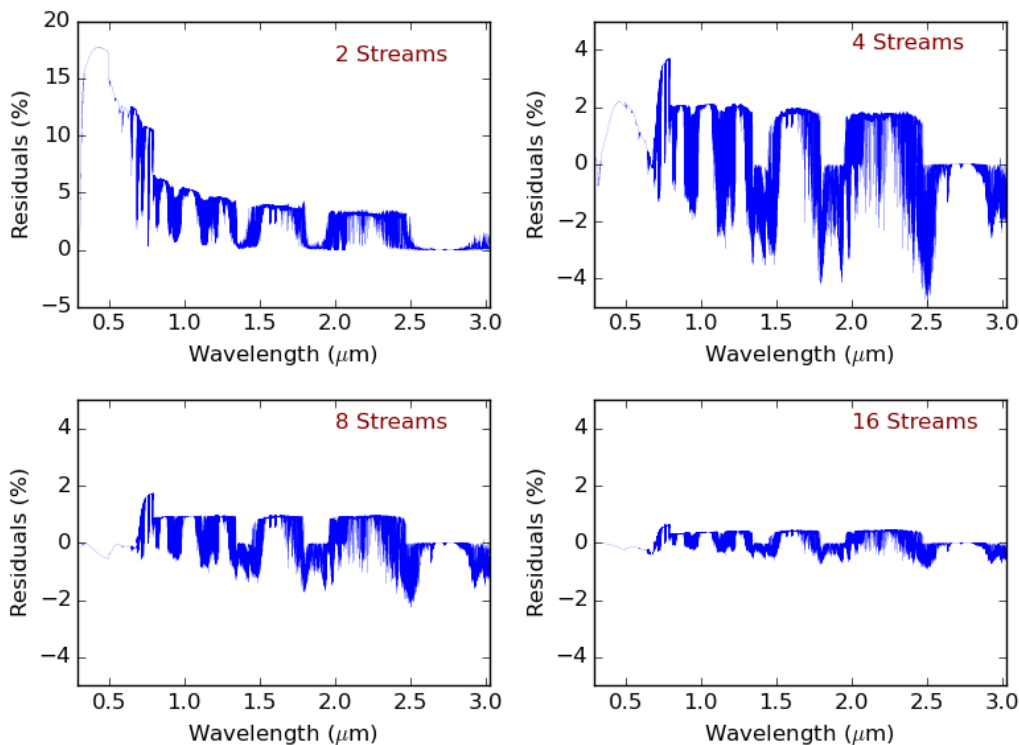


Figure 5.2: Residuals (%) of the Exact-RT LIDORT radiances for 2, 4, 8, and 16 streams compared with the 32-streams LIDORT calculations. Optical properties as for Figure 5.1

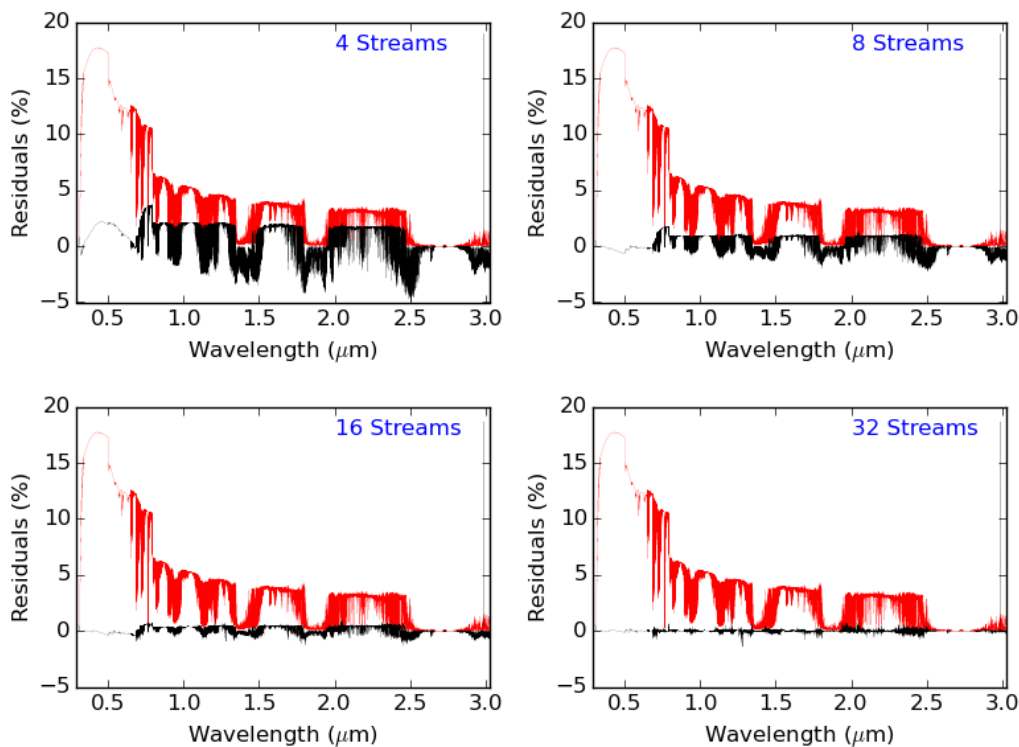


Figure 5.3: Residuals (%) for the PCA (black) and 2S (red) models as compared to 32 stream LIDORT over the entire shortwave range. The residuals have been Gaussian smoothed to 0.2 cm^{-1} .

That said, the PCA model residuals still have scope for improvement. Figure 5.4 shows PCA residuals with and without Gaussian smoothing over a small spectral field using 32 stream LIDORT. While residuals are of order 0.1% over most wavenumbers, there are a small number of wavenumbers with errors around 1% . We find that these wavenumbers are located either at the cores of weak absorptions or in the wings of strong absorptions, typically with total column optical depths between $0.1 - 10$. Figure 5.5 shows the improvements in runtime of the PCA model versus the Exact Model. We find that run-time is reduced by a factor of 10-100 for different spectral fields. The speed of the PCA model is currently limited by the rate at which optical properties are generated *ab initio* from databases, thereby resulting in somewhat arbitrary runtime improvements which are unrelated to the actual RT calculation. Runtime can be further optimized by using tabulated optical property inputs, for instance. We are able to show that the PCA RT technique is capable of producing accuracy comparable to 32 stream, full LIDORT RT calculations with run-times comparable to those from a 2S model. While the PCA routine works extremely well

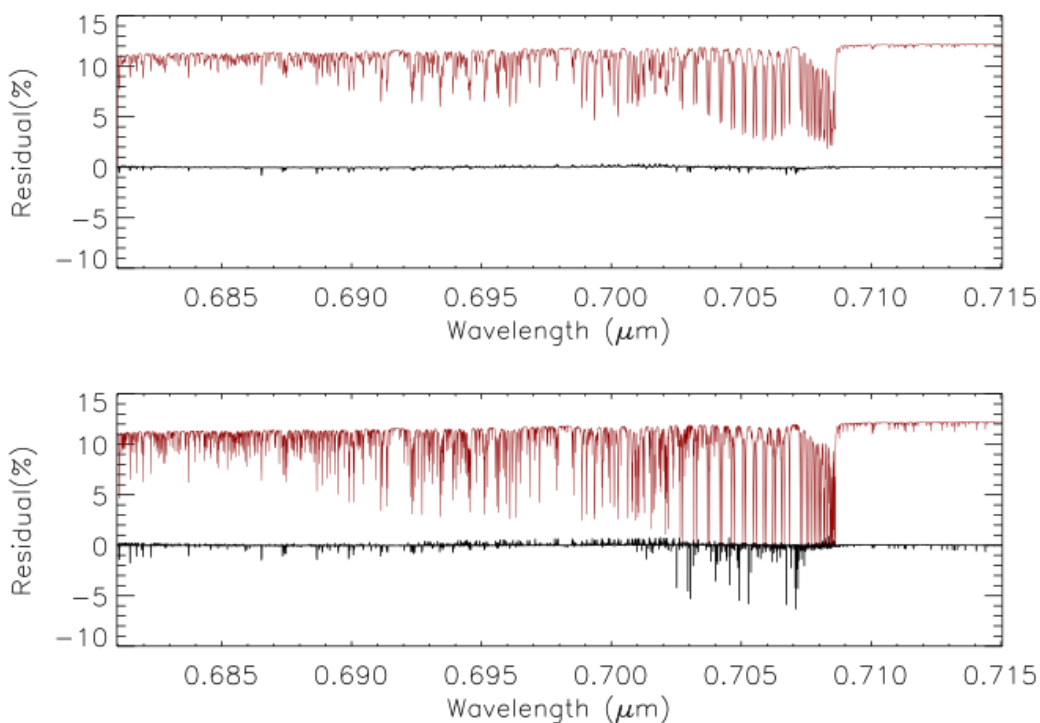


Figure 5.4: Residuals of the PCA (black) and 2 Stream (red) models as compared to 32 stream LIDORT with (top) and without (bottom) smoothing for spectral field 9, where the dominant gas absorbers are oxygen and water.

for $> 99.9\%$ of all points on the shortwave spectrum as defined here, a few points continue to show sizeable irreducible errors. Within the paradigm of choosing binning schemes for each spectral field, no further improvements could be made. We were stuck at this point for a long time, and we had to attack the problem from a different direction to make progress again.

5.5 PCA Efficiencies

Much of the material in this and the following subsections is from Kopparla et al., 2017. To get the smallest errors possible when reconstructing the optical properties with a given number of EOFs, we tested a few different transformations on the optical properties. Particularly interesting are the cases where the optical properties are re-gridded onto a grid with uniform pressure thickness layers, and when the PCA is performed on the optical properties themselves (hereafter referred to as "linear PCA"), rather than their logarithms that were used in previous work (hereafter referred to as "log PCA"). For testing, we chose optical depth profiles from bin 9 (binning is discussed in detail in the Section 2.5) of spectral range 11 (refer

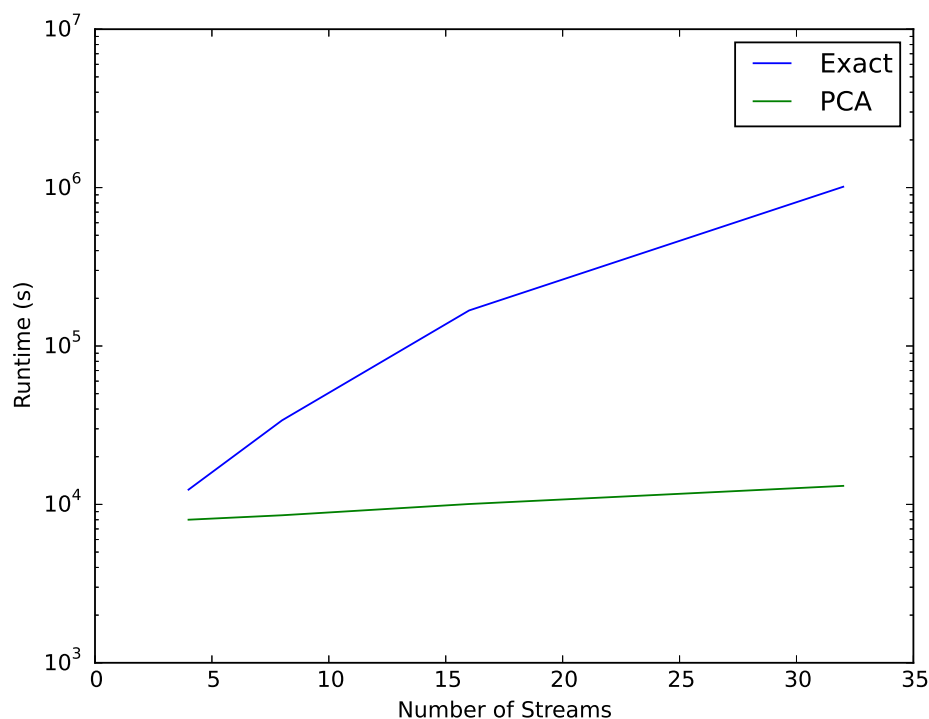


Figure 5.5: The sum total of the runtime of LIDORT and PCA model over all spectral fields for one profile with changing number of computational streams. Note from Figure 3 that increasing the number of streams improves the PCA RT accuracy, with very little time penalty as shown in this figure. Refer to text for further discussion.

Table 5.1) which contains monochromatic grid points with column optical depths between 1 and 5. The profiles are taken from the GEOS-CHEM model (Bey et al., 2001) and represent atmospheric conditions over diverse locations in North America and contain both aerosols and absorbing gases but no clouds. The behavior found here is fairly general, and reproducible in other regions and bins. The results are shown in Fig. 1. Using equal pressure thickness layers provides an order of magnitude improvement in spectral residuals compared to the standard model (arbitrary pressure grid and log PCA), while linear PCA provides two orders of magnitude improvement. When both equal pressure thickness layers and linear PCA are used together, we obtain three orders of magnitude improvement. Note, however, that we are only reconstructing optical properties here; translating these improvements into the correction factors for the RT model introduces additional difficulties. Using linear, rather than logarithmic optical depths sometimes introduces negative values when optical properties are perturbed (Eqns. 4 & 5) and the resulting spectra are

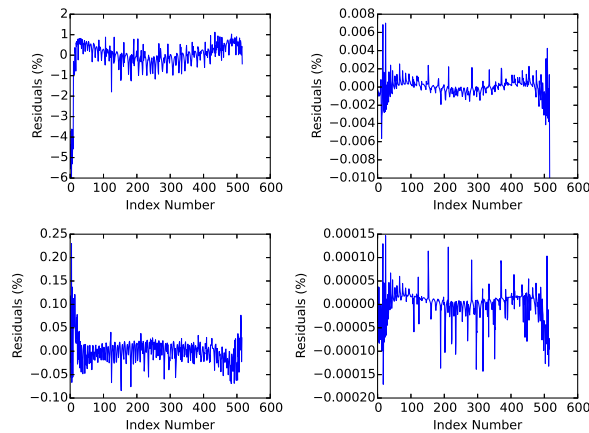


Figure 5.6: Total column optical depth reconstruction accuracy using 5 EOFs for various settings: (upper left) "standard" PCA on log optical properties on an arbitrarily spaced vertical grid, (upper right) same as standard PCA but with linear optical properties, (lower left) PCA on log optical properties on an equal pressure thickness grid, (lower right) PCA on linear optical properties on an equal pressure thickness grid. Optical depths are reconstructed layer by layer and then summed, and compared to the total column optical depth in the original data set.

not always better than those with the log optical properties. Incorporating linear PCA correctly into the RT model requires more work, and is a possible direction for future attempts. Using equal pressure thickness layers, on the other hand, does not pose any such issues. Even though the root mean square error remains about the same, the largest errors are significantly reduced (Fig. 2). Therefore, we perform all calculations on equal pressure thickness grids. The percentage residuals in all figures are calculated as:

$$\Delta I = \frac{(I_{PCA} - I_{Exact}) * 100}{I_{Exact}^{continuum}} \quad (5.10)$$

We calculate residuals with respect to the continuum radiance (maximum radiance in the spectral region) to avoid artificial amplification of errors in regions with very strong gas absorption (due to division by small numbers). Using the continuum radiance in the denominator shifts sensitivity of the error metric away from the darkest points.

5.6 Aerosol Scheme

Previous versions of the PCA-based RT model employed bin averages for aerosol properties. With such treatment of aerosols, residual patterns invariably display

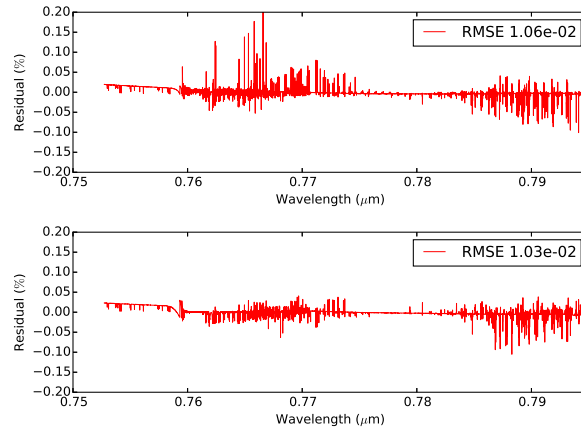


Figure 5.7: Comparison of PCA RT performance: (top) arbitrarily spaced vertical grid, (bottom) equal pressure thickness grid. Both grids have 114 layers. RMSE denotes the root mean square error.

gradient (slope) biases (see for example, Figure 3, bottom panel), which are present due to the lack of representation of slowly changing aerosol properties in the PCA mean-perturbation process. On the other hand, adding full vertical profiles for several aerosol types to the optical properties matrix adds an unnecessary computational burden. However, we make the (reasonable) approximation that, unlike Rayleigh scattering and gas absorption, for each aerosol type, the properties are wavelength, but not altitude, dependent. This results in just one additional number (per aerosol type; essentially the total column extinction optical depth of that type) to the optical properties matrix. For further accuracy, we could also add the total column scattering optical depth of each aerosol type to the matrix. This is in a way similar to the way we handle surface albedo changes. As a result of this inclusion, the slope in the residuals is greatly diminished (Fig. 3). Aerosol total column optical depth is of order 10^{-3} in the profiles we use.

5.7 Further Modifications to Binning Schemes

Monochromatic spectral grid points in each bin must be chosen such that the optical properties are strongly correlated. We find that there is no one generic binning scheme that is appropriate for all spectral regions; rather, the choice of binning scheme and the number of bins used are sensitive to the complexity of spectral absorption in the region. In the following, we discuss different approaches necessary to achieve $< 0.1\%$ residuals at every single monochromatic grid point over a given spectral region.

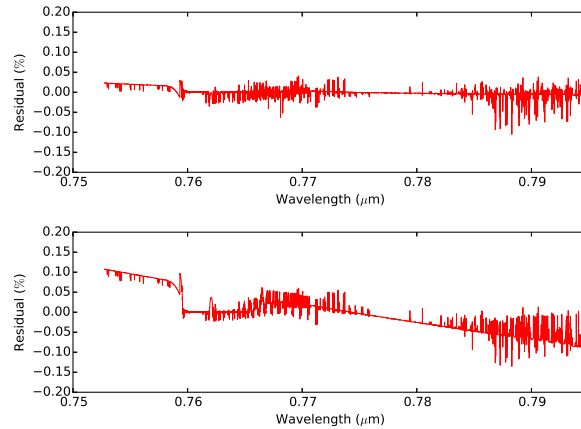


Figure 5.8: Differences in PCA RT residuals (bottom) using bin averaging for aerosol optical properties, and (top) with explicit inclusion of aerosols in the PCA process. Note the almost complete elimination of the slope in the latter scenario.

The entire shortwave region from $0.3 - 3\mu\text{m}$ is first divided into 34 spectral windows depending on dominant gas absorption within the window (Table 5.1).

Scheme 1

The most straightforward cases include a spectrally-uniform continuum absorption with little gas absorption fine structure. In such cases, monochromatic grid points are grouped into bins which are equally spaced in the logarithm of total column gas absorption optical depth. For example, in a window where the total column gas absorption optical depths lie between 0.01 and 10, a four-bin scheme would have these bin ranges: $(0 - 0.01)$, $(0.01 - 0.1)$, $(0.1 - 1.0)$ and $(1.0 - 10)$. Scattering is included in the process through the use of Rayleigh scattering optical depth and aerosol optical depths in the calculation of the optical property EOFs. Depending on the complexity of the absorption band, more or fewer bins maybe required to reach the specified precision. A slowly-varying continuum range can be simulated with as few as one bin, but the residuals will have a clear parabolic structure, with negative residuals at either end of the field and positive ones at the center. This structure is likely due to the quadratic nature of the error correction applied (Eqn. 8). Total column gas absorption optical depths below 0.01 can be grouped together in most cases without much loss of accuracy since this is close to continuum scattering, and the vertical profile of gas absorption is irrelevant. Similarly, for total column gas absorption optical depths above 10, the extinction is strong enough that radiances are very small. This is a situation dominated by single scattering above the absorption

layer, and PCA corrections are irrelevant.

Scheme 2

In spectral windows where a significant fraction of spectral points fall within rapidly varying absorption bands due to one or multiple absorbers, the simple scheme above fails to yield residuals under 0.2% in most cases. It is possible to reduce residuals by using a large number of bins (~ 100), but that approach significantly slows down the calculation. We use a more empirical scheme for these regions. We start with the following four bins in total column absorption optical depth: (0 – 0.01), (0.01 – 0.1), (0.1 – 1.0) and (1.0 – ∞). The PCA RT model, as described in the Sections 2.1 and 2.2, is applied to each spectral range with these initial bins, and the residuals are computed with respect to "Exact Model" using 8-stream LIDORT (We have tested binning by using upto 32 streams, in general, binning schemes affect errors at 32-streams in much the same way as they do at 8). Next, bins with large residuals are again bisected with respect to total column optical depth; for instance, the second bin would be split into (0.01 – 0.05) and (0.05 – 0.1). This process is repeated until the residuals are below 0.01% for every spectral point. We find that, following this procedure, a total of eleven bins provide satisfactory residuals. The upper limits of gas absorption optical depth for these bins are (0.01, 0.025, 0.05, 0.1, 0.25, 0.5, 0.625, 0.75, 1.0, 5.0, ∞). Most of our testing was centered on the spectral window 11 (Table 5.1) around $0.76\mu\text{m}$ which contains the oxygen A-band. We find that this binning scheme, and in particular the bins derived from the $0.76\mu\text{m}$ range, are well suited to direct application in similar windows across the $0.3 - 3\mu\text{m}$ shortwave region.

Other Issues

However, spectral range 4 (Table 5.1) remains difficult to simulate. This range has four absorbing gases (O_3 , H_2O , NO_2 , O_4) and three, well separated absorption bands, of which the first is particularly ill-behaved (Fig. 5). Several binning schemes were attempted, including using separate bins for absorptions by different gases, but these did not yield significant improvements. Another scheme used the separation of monochromatic grid points into bins based on the shape of the vertical gas absorption profile rather than the total column gas absorption, inspired by the method used for spectral mapping in the SMART RT model (Crisp, 1997). If the optical depth of a monochromatic grid point was similar to other monochromatic grid points in a bin within 10% at every single vertical level, these monochromatic grid points

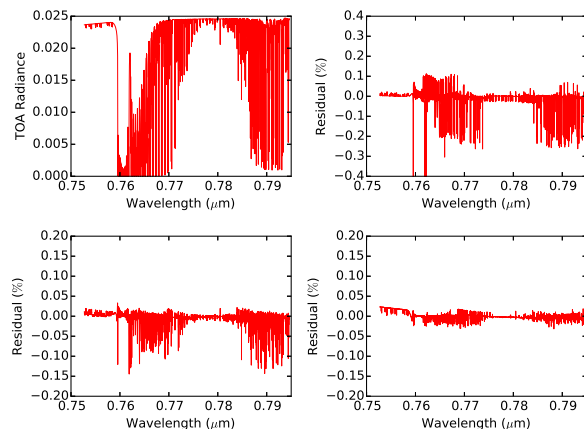


Figure 5.9: (upper left) TOA radiances, (upper right) residuals using Scheme 1 with 11 bins, (lower left) residuals using Scheme 1 with 21 bins, and (lower right) Scheme 2 with 11 bins, for spectral window 11. The band of absorption lines centered at $0.76\mu\text{m}$ is the O₂ A-band, and that around $0.79\mu\text{m}$ is due to water vapor absorption.

were grouped together. Otherwise a new bin was created for this monochromatic grid point. While residuals were generally acceptable with this binning scheme, it frequently created several hundred bins due to the diversity of vertical profiles, was thus rejected for reasons of speed. In the end, spectral region 4 was split into two regions around $0.53\mu\text{m}$ and the calculations were done separately for each region.

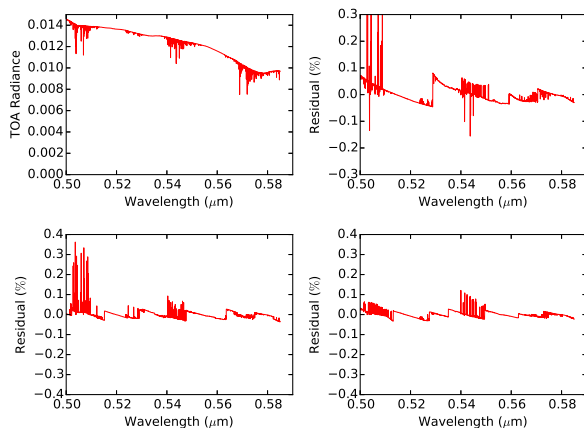


Figure 5.10: Top of the atmosphere radiances (top left) and residuals using Scheme 2 with 5 bins (top right), 21 bins (bot left) for spectral range 4. Since adding more bins was found to be ineffective with both Schemes 1 (not shown here) and 2, the spectral range was split into two around $0.535\mu\text{m}$. Each piece was then treated as a separate spectral range and solved using Scheme 1 binning with 5 bins (bot right).

Over each range, monochromatic grid points are grouped into four bins, based on

the total column optical depth. The runtime of the code scales linearly with the number of bins. Note from Table 5.1 that the number of wavelengths and the spectral resolution vary according to spectral range — finer absorption features require higher resolution.

We also found that some degree of iteration was necessary in order to determine an acceptable binning scheme for a given spectral range. However, we find that the general magnitude and spectral distribution of errors is stable with respect to viewing geometry, changes in aerosol distribution and surface albedo (Fig. 6). In other words, given a spectral region with a known number of gas absorbers, a binning scheme only needs to be devised once and can be reused for any number of diverse scenarios.

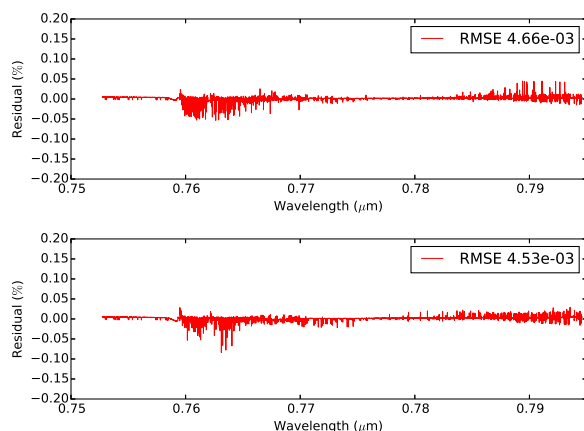


Figure 5.11: Residuals in spectral window 11 for two different profiles, with different viewing geometries, aerosol densities and surface types, using Scheme 2 with 11 bins. For a given binning scheme, errors remain fairly constant for different atmospheric profiles taken from the GEOS-CHEM model (Bey et al., 2001).

5.8 Final Results and Discussion

The dependence of model performance and run time on number of EOFs, number of streams used in the "exact" model and number of bins used have been discussed earlier (Kopparla et al., 2016). Unless otherwise stated, all results shown here use 4 EOFs, and the exact model uses 8 streams (whole space, 4 streams in half space) for the RT calculation. Better accuracies can be achieved by the use of higher number of streams, at the cost of runtime. Smoothing to typical instrument resolutions will again reduce outliers and improve RMS errors. TOA radiances for a representative atmospheric profile are shown in Fig. 7, with and without aerosols.

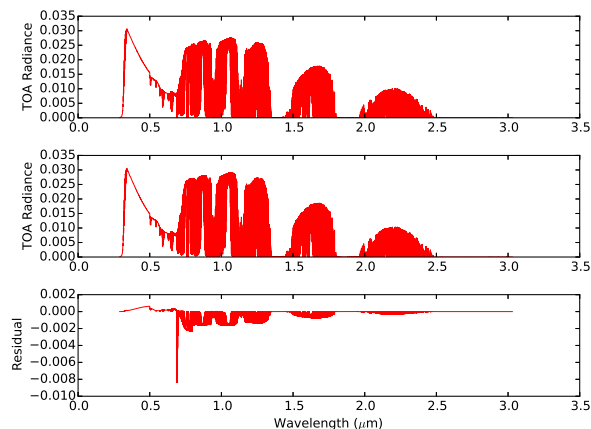


Figure 5.12: TOA radiances over the entire shortwave range of interest, (top) with and (middle) without aerosols, and the difference between the aerosol and no aerosol cases (bottom) for a representative atmospheric profile.

Residuals for the same profile, with aerosols, are shown in Fig. 8. We find that the binning scheme derived from spectral range 11 (Scheme 2) works reasonably well as a one-size-fits-all solution. However, a few unacceptably large residuals remain. Spectral windows 2 and 3 show large, parabolic shaped residuals. These two ranges have no strong gas absorptions, and therefore all points fall into the lowest total optical depth bin in Scheme 2 and all other bins are empty. As discussed in the binning section, this leads to parabolic residuals. Therefore, we use Scheme 1 here. Scheme 1 works admirably for range 16, which had a large spike in residual. As discussed before, spectral range 4 needed to be split in two, and each piece independently solved using Scheme 1. With these settings, we are able to achieve better than 0.01% residuals at every single one of 457701 points across the broadband region.

In order to better understand the variation of errors with location, viewing geometry and so forth, Scheme 2 binning was tested over the entire 0.3 – 3 μ m range for 70 profiles taken from the GEOS-CHEM global 3-D chemical transport model (Bey et al., 2001). Profiles representing locations in North America were chosen over a wide range of latitudes and longitudes, each one with different viewing geometries and aerosol concentrations. The error statistics are shown in Fig. 6. The histogram shows the mean distribution of errors over all profiles, and the blue error bars show one standard deviation.

In summary, we have shown that the PCA RT technique can produce broadband

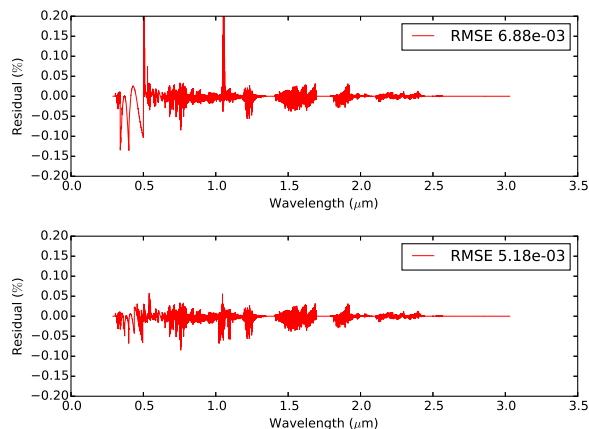


Figure 5.13: Residuals over the entire shortwave range of interest using (top) purely Scheme 2 and (bottom) a combination of Schemes 1 and 2, for a representative atmospheric profile.

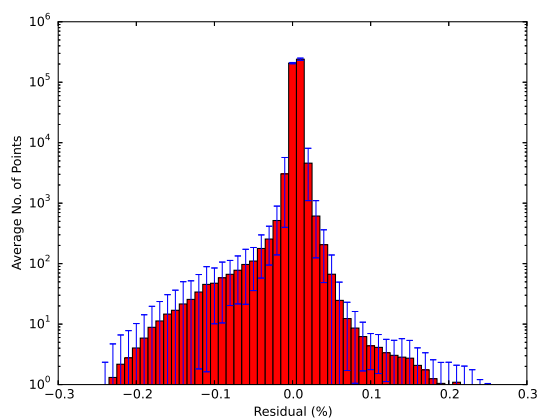


Figure 5.14: Mean distribution of residuals over 70 diverse atmospheric profiles using binning Scheme 2.

spectral radiances at 0.1% maximum residual and 0.005% RMS error. The inclusion of aerosol properties in the PCA procedure, as well as the use of an equal pressure thickness grid contributed significantly to reduce errors. The issue of using linear instead of logarithmic optical properties shows promise to improve the model further, and will be investigated in the future. The PCA RT technique should also be compared rigorously to existing fast RT models to better assess its strengths.

Acknowledgements

We thank members of Prof. Yung's group for useful comments. We also thank the anonymous referee for insightful suggestions that helped improve the manuscript. This research was supported in part by NASA NNX13AK34G grant to the California Institute of Technology and the Orbiting Carbon Observatory (OCO-2) Project at JPL. We thank members of Yung's group for useful comments. This research was supported in part by an NAI Virtual Planetary Laboratory grant from the University of Washington to the Jet Propulsion Laboratory and California Institute of Technology, and part of the research described here was carried out at the Jet Propulsion Laboratory, California Institute of Technology, under a contract with the National Aeronautics and Space Administration. YLY was supported in part by NASA NNX09AB72G grant to the California Institute of Technology. PS is funded by the ESA Greenhouse Gas Climate Change Initiative (GHG-CCI) as part of a PhD studentship.

5.9 Acknowledgements

We thank members of Prof. Yung's group for useful comments. We also thank the reviewers for several insights that improved the paper. This research was supported in part by an NAI Virtual Planetary Laboratory grant from the University of Washington to the Jet Propulsion Laboratory and California Institute of Technology, and part of the research described here was carried out at the Jet Propulsion Laboratory, California Institute of Technology, under a contract with the National Aeronautics and Space Administration. YLY was supported in part by NASA NNX09AB72G grant to the California Institute of Technology. PS is funded by the ESA Greenhouse Gas Climate Change Initiative (GHG-CCI) as part of a PhD studentship.

Table 5.1: Spectral Fields as Defined by Major Gas Absorptions.

Spectral Field	Wavelength Range (μm)	No. of Spectral Points	Gas Absorbers
1	0.290-0.340	1001	<i>O₃, NO₂, SO₂, HCHO, BrO</i>
2	0.340-0.400	1200	<i>O₄, NO₂, HCHO, BrO</i>
3	0.400-0.500	2000	<i>NO₂, CHOCHO</i>
4	0.500-0.585	1700	<i>O₃, H₂O, NO₂, O₄</i>
5	0.585-0.605	400	<i>O₃, H₂O, NO₂, O₄</i>
6	0.605-0.630	500	<i>O₃, H₂O, NO₂, O₄</i>
7	0.630-0.650	398	<i>O₃, H₂O, NO₂, O₄</i>
8	0.650-0.681	14001	<i>H₂O</i>
9	0.681-0.715	14000	<i>H₂O, O₂</i>
10	0.715-0.752	14000	<i>H₂O, O₂</i>
11	0.752-0.794	14000	<i>H₂O, O₂</i>
12	0.794-0.841	14000	<i>H₂O, O₂</i>
13	0.841-0.894	14000	<i>H₂O, O₂</i>
14	0.894-0.954	14000	<i>H₂O, O₂</i>
15	0.954-1.022	14000	<i>H₂O, O₂</i>
16	1.022-1.101	14000	<i>H₂O, O₂</i>
17	1.101-1.205	15701	<i>H₂O, O₂</i>
18	1.205-1.234	20000	<i>H₂O, O₂</i>
19	1.234-1.560	33800	<i>H₂O, O₂, CO₂</i>
20	1.560-1.626	26000	<i>H₂O, O₂, CO₂</i>
21	1.626-1.695	25000	<i>H₂O, O₂, CO₂, CH₄</i>
22	1.695-1.923	14000	<i>H₂O, CO₂, CH₄</i>
23	1.924-2.105	45000	<i>H₂O, O₂, CO₂</i>
24	2.105-2.128	5000	<i>H₂O, O₂, CO₂, N₂O</i>
25	2.128-2.222	20000	<i>H₂O, CO₂, CH₄, N₂O</i>
26	2.222-2.247	5000	<i>H₂O, O₂, CH₄</i>
27	2.247-2.299	10000	<i>H₂O, O₂, CH₄, N₂O</i>
28	2.299-2.410	20000	<i>H₂O, O₂, CH₄, CO</i>
29	2.410-2.439	5000	<i>H₂O, O₂, CO</i>
30	2.439-2.564	20000	<i>H₂O, N₂O, CO₂, CH₄</i>
31	2.564-2.632	10000	<i>H₂O, N₂O, CO₂</i>
32	2.632-2.857	30000	<i>H₂O, O₂, CO₂</i>
33	2.857-3.030	20000	<i>H₂O, N₂O, CO₂</i>